The Pennsylvania State University
The Graduate School

STUDIES OF MATRIX ELEMENTS OF OBSERVABLES IN QUANTUM MANY-BODY SYSTEMS

A Dissertation in
Physics
by
Tyler LeBlond

© 2021 Tyler LeBlond

Submitted in Partial Fulfillment
of the Requirements
for the Degree of

Doctor of Philosophy

May 2021

The dissertation of Tyler LeBlond was reviewed and approved by the following:

Marcos Rigol
Professor of Physics
Dissertation Advisor
Chair of Committee

Eugenio Bianchi
Assistant Professor of Physics

Mikael Rechtsman
Downsbrough Early Career Development Professor of Physics

Luen-Chau Li
Professor of Mathematics

Nitin Samarth
Professor of Physics
George A. and Margaret M. Downsbrough Department Head

Abstract

In this thesis, we use numerical exact diagonalization to contrast an interacting integrable Hamiltonian (the paradigmatic spin-1/2 XXZ chain) with related quantum chaotic models. In systems with translational symmetry, we first demonstrate that the bipartite von Neumann entanglement entropy can powerfully distinguish the two classes of systems. Then, the majority of the thesis is spent studying the matrix elements of local operators in Hamiltonian eigenstates at the center of the spectrum. The most novel results are in interacting integrable models: for diagonal matrix elements, we show evidence that the support does not vanish with increasing system size, while the average eigenstate-to-eigenstate fluctuations vanish in a power-law fashion. For the off-diagonal matrix elements, we show that they follow a distribution that is close to (but not quite) log-normal, and that their variance is a well-defined function of $\omega = E_\alpha - E_\beta$ ($\{E_\alpha\}$ are the eigenenergies) proportional to $1/D$, where D is the Hilbert space dimension. Establishing this for translationally symmetric operators, we continue on to study the off-diagonal matrix elements of observables that break the translational symmetry of the Hamiltonian, and as such connect energy eigenstates from different total quasimomentum sectors. In quantum-chaotic models, we find that there is eigenstate thermalization, and in interacting integrable models, we find the same behavior noted above. We deepen our study of off-diagonal matrix elements in both classes of systems by investigating the low-frequency behavior of their variances and unveiling the regimes in which it exhibits diffusive vs ballistic scaling. We show that in quantum-chaotic models the behavior of the variance is qualitatively similar for matrix elements that connect eigenstates from the same vs different quasimomentum sectors. We also show that this is not the case in the interacting integrable model for observables whose translationally invariant analogue does not break integrability if added as a perturbation to the Hamiltonian. Additionally, we demonstrate that a single magnetic defect embedded in the XXZ chain with open boundary conditions gives rise to eigenstate thermalization while retaining the microcanonical predictions of local observables and the ballistic character of spin transport from the integrable model. Lastly, we show that the onset of quantum chaos in the perturbed XXZ chain and perturbed Anderson models is marked by universal behavior including a peak in the fidelity susceptibility that scales with the square of the inverse level spacing. This peak is located at decreasing perturbation strengths, suggesting that neither model is stable to perturbations in the the thermodynamic limit.

Table of Contents

List of Figures

Acknowledgments

I have been privileged in many ways to be able to devote the last several years to the completion of the work contained in this thesis and to have a good and supportive environment in which to thrive during the process.

I thank my advisor, Marcos Rigol, who patiently mentored me and trained me to not only perform state of the art calculations, but to carefully analyze data to discover meaningful and novel results and to strive for absolute correctness while never cutting corners. I thank him for always seeking to involve me in cutting edge projects and pushing me hard while also being sensitive to my needs as a person and willing to coordinate with me and my personal goals.

I thank my committee members Mikael Rechtsman, Eugenio Bianchi, and Luen-Chau Li for their willingness to learn about my research, ask interesting questions, and make valuable comments along the way. I thank my collaborators Lev Vidmar, Krishnanand Mallayya, Marlon Brenes, John Goold, Dries Sels, and Anatoli Polkovnikov for making studying physics exciting and dynamic.

I thank my family for supporting and loving me throughout my entire life. I also would not have been able to complete this journey without support from mentors and friends within the Christian community in State College. It is through the church during these years that I found some of the deepest relationships I have ever had. I thank Lam Tran above all for discovering Christ with me. I thank Adam Kling, SJ Roh, and Alex Zubler for being my closest brothers in the faith. I thank Dan Min and Bryan Schlake for mentoring me. I give the final and most resounding thanks to the Lord, who grew and sustained me during this season of life.

I acknowledge funding support through the National Science Foundation Grant No. PHY-1707482 and PHY-2012145. The conclusions and findings found within this thesis do not necessarily reflect the views of the National Science Foundation.

Chapter 1 Introduction

In this chapter, I provide an overview of some recent advances in quantum many-body physics, with a particular emphasis on the relaxation dynamics of observables in chaotic and integrable quantum systems and its relationship with matrix elements. I borrow heavily from a review article which has been written by our research group (Ref. [2]) while adding further depth in some areas. I also include details of advances in the field which were published more recently, and which directly connect with the story told in the later chapters of this thesis. Lastly, I provide some details about our numerical methods, which are usually not discussed in the literature.

1.1 Relaxation Dynamics in Isolated Quantum systems

1.1.1 Classical Chaos and Integrability

In classical mechanics, chaos is understood to be the underlying mechanism for thermalization. Non-linearity in the underlying equations of motion of classically chaotic systems allows them to unpredictably sample their phase spaces[1]. The rigorous connection between chaos and thermalization in classical systems is beyond the scope of this thesis, and is perhaps still a subject of academic debate. Here, I qualitatively describe a couple of connections between chaos and thermalization which lend themselves to our later discussion of quantum thermalization. Interestingly, quantum thermalization is better understood from microscopic dynamics than classical thermalization is, as will be made

[1]Non-linearity is a necessary but not sufficient condition for chaos: general linear differential equations are always reducible into systems of first order linear ones, which can be readily solved and are not chaotic. It is much harder to find analytic solutions to nonlinear differential equations. This is not diagnostic of chaos, however, and the accepted way to characterize chaos in classical systems is through the Lyapunov exponent which will be described later.

clear in Section 1.3.

A major defining feature of classically chaotic systems is that their phase space trajectories are exponentially sensitive to their initial conditions. The motion of such a system in its accessible phase space is unconstrained and it uniformly covers its phase space in infinite time. This notion is called ergodicity, wherein one can state that long time averages of physical quantities are equivalent to unbiased (microcanonical) averages of the physical quantity over the accessible phase space of the system. In isolated systems, one generally identifies convergence to this microcanonical average as thermalization (for large systems, it is equivalent to the canonical average of systems in contact with a thermal bath). Thus, ergodicity implies thermalization of the long-time average of physical quantities.[2]

Ergodicity explains thermalization of the long-time average of a physical quantity, but does not guarantee thermalization at instantaneous points of time. For this, one must invoke typicality, which is the notion that the vast majority of points in phase space have similar physical properties. Then, the microcanonical average of a physical quantity will be equal to the value of that quantity at a typical point in the phase space. A system evolving under chaotic dynamics would then tend from its atypical initial configuration into typical phase space points and yield measurements consistent with the microcanonical ensemble. This explanation of thermalization presumes that all accessible points in phase space are equally probable (ergodicity), or at least that atypical configurations are not much more likely to be sampled than typical ones under dynamical evolution.[3]

The relaxation process described above is impossible if the system cannot freely explore its phase space. Systems that have conserved quantities have constrained trajectories in phase space. For these systems, the microcanonical average of a physical quantity includes regions of phase space that are inaccessible to the system and will therefore be inaccurate. One can still obtain an accurate phase space average for which the argument of typicality applies within the subdomain of phase space for which the system is chaotic. In the limit where a system has as many conserved quantities as it has degrees of freedom, its motion is fully constrained. Such a system is said to be integrable, and the statistical

[2]While the above definition of ergodicity does not apply in quantum systems, where there is no well-defined phase space, quantum ergodicity is related to delocalization of the Hamiltonian eigenvectors.

[3]In quantum systems, it will be shown that the vast majority of eigenstates have thermal expectation values for few-body observables in both chaotic and integrable systems, so in that sense the eigenstates of both classes of systems are 'typical'; however, the latter class of systems does not thermalize. The reason for this will be discussed later.

arguments made above no longer apply[4]. We next delve into relaxation dynamics in quantum mechanical systems and its connection with matrix elements, which is the main subject of this thesis.

1.1.2 Ultracold Atom Experiments

Within the last twenty years, questions of relaxation dynamics in isolated quantum systems have been opened by modern advances in the control and isolation of ultracold atoms. These advances have enabled physicists to probe relaxation phenomena in quantum many-body systems over large time scales in what is known as quantum simulation [3–5]. Certain landmark experiments confirmed that there is a lack of thermalization in some setups [6–9] while there is thermalization in others [9–12]. For example, in Ref. [6], a so-called quantum Newton's cradle was created in which one-dimensional Bose gases with point-like interactions did not thermalize over the time-scale of the experiment. This is rationalized by the near-integrability of the setup. Recently, Ref. [9] took this a step further using a quantum Newton's cradle with tunable integrability-breaking magnetic dipole interactions to show a separation of relaxation timescales between a pre-thermal one at short times (which was captured by Ref. [6], and can be described by the generalized Gibbs ensemble (GGE), to be discussed later) and the thermal one which occurs at long times. From a theoretical standpoint, it is interesting to wonder how a pure quantum state which depends on exponentially many parameters (the expansion coefficients of the initial state in the eigenbasis of the Hamiltonian governing the quantum dynamics) can relax to the predictions of a statistical ensemble which depends on a much smaller set of parameters (a set which is O(1) in nonintegrable systems but O(L) in integrable systems). Additionally, how can pure quantum states yield the same measurements at long times as statistical ensembles, which are mixed states? We discuss next how the unitary dynamics of pure states in quantum systems plays out at the level of observable matrix elements, the behavior of which is the main subject of this thesis. We will also later see a connection between thermalization and entanglement entropy.

1.1.3 Unitary Dynamics of a Pure State

Suppose we have a quantum system prepared in an eigenstate of Hamiltonian $\hat{H}_0$ and evolving under a new Hamiltonian $\hat{H}$. In the basis of $\hat{H}$, the initial state $|\psi(0)\rangle =$

[4]Conversely, as we will describe later, quantum integrable systems can still be described by a fully constrained ensemble known as the generalized Gibbs ensemble (GGE).

$\sum_\alpha C_\alpha|\Psi_\alpha\rangle$ evolves under $\hat{H}$ as $|\psi(t)\rangle = \sum_\alpha C_\alpha e^{-iE_\alpha t}|\Psi_\alpha\rangle$. The expectation value of an observable $\hat{O}$ in this time-evolved state is

$$\langle\hat{O}(t)\rangle = \langle\psi(t)|\hat{O}|\psi(t)\rangle = \sum_{\alpha\beta} C_\alpha^* C_\beta e^{i(E_\alpha - E_\beta)t} O_{\alpha\beta}, \tag{1.1}$$

where $O_{\alpha\beta} = \langle\Psi_\alpha|\hat{O}|\Psi_\beta\rangle$. This sum can be broken up into diagonal and non-diagonal sums as follows:

$$\langle\hat{O}(t)\rangle = \sum_\alpha |C_\alpha|^2 O_{\alpha\alpha} + \sum_{\alpha\neq\beta} C_\alpha^* C_\beta e^{i(E_\alpha - E_\beta)t} O_{\alpha\beta}. \tag{1.2}$$

Clearly, the diagonal sum is constant in time but the terms in the non-diagonal sum are oscillating with frequencies given by the eigenenergies of $\hat{H}$. In order to see what the equilibrium value of this quantity would be (if it equilibrates at all), one can take the time average of $\langle\hat{O}(t)\rangle$ over the domain $[0,\infty)$. Each term in the second sum yields an integral

$$\lim_{T\to\infty}\frac{1}{T}\int_0^T e^{i(E_\alpha - E_\beta)t} = \lim_{T\to\infty}\frac{1}{T}\frac{e^{i(E_\alpha - E_\beta)t}}{i(E_\alpha - E_\beta)} = 0. \tag{1.3}$$

Importantly, we have assumed that the spectrum is non-degenerate[5]. Thus, because all of the contributions to the second sum vanish over the infinite time average, the long time average of observable $\hat{O}$ is

$$\overline{\langle\hat{O}(t)\rangle} = \sum_\alpha |C_\alpha|^2 O_{\alpha\alpha}. \tag{1.4}$$

We note that this result is equivalent to the prediction of a so-called 'diagonal ensemble' with density matrix $(\rho_{DE})_{\alpha\beta} = |C_\alpha|^2\delta_{\alpha\beta}$. To summarize what we have shown so far, decoherence of the initial state yields an expected equilibrium value that is the same as that of mixed state with exponentially many parameters. This equilibrium value depends on diagonal matrix elements of the observable in question, while all of the time-dependent behavior (including the approach to equilibrium and fluctuations about equilibrium) are controlled by the off-diagonal elements. In what follows, we seek to understand how $\overline{\langle\hat{O}(t)\rangle}$ can be equivalent to the equilibrium value of observables obtained from various statistical ensembles, and additionally how we can expect relaxation to occur over

[5]In the systems studied throughout this thesis, both integrable and nonintegrable, it is generally the case that the spectrum is nondegenerate once one has accounted for all symmetries. Even if there are O(1) degeneracies, they will only negligibly effect the time-independent outcome of this analysis since the number of terms in the first sum is exponentially large.

reasonable timescales given that the longest physical timescale, the so-called Heisenberg time $t_H \sim 1/\omega_H$, is expected to diverge exponentially in system size due to energy levels being exponentially close. We first explore quantum chaos and thermalization in non-integrable quantum systems, which is understood on the mathematical basis of random matrix theory (RMT) and its generalization to physical systems in the eigenstate thermalization hypothesis (ETH). Then, we explore how Eq. (1.4) is equivalent to the GGE in quantum integrable systems through generalized eigenstate thermalization.

1.2 Quantum Chaos

One of the defining questions of quantum thermalization is how Eq. (1.4) can be equivalent to the microcanonical ensemble which only depends on one parameter: the energy density of the initial state. In order for $\langle \hat{O}(t) \rangle$ to reach thermal equilibrium, Eq. (1.4) must be equal to

$$\sum_{\alpha} |C_\alpha|^2 O_{\alpha\alpha} = O_{ME}(\langle E \rangle) = \frac{1}{N} \sum_{|E_\alpha - E_0| < \Delta E} O_{\alpha\alpha}, \tag{1.5}$$

where $O_{ME}(\langle E \rangle)$ is the microcanonical average of $\hat{O}$ at $\langle E \rangle = \langle \psi(0)|\hat{H}|\psi(0)\rangle$, ΔE defines a small window of energy eigenvalues, and N is the normalization constant. In a landmark paper, Rigol *et al.* demonstrated relaxation of a nonintegrable quantum many-body system to the microcanonical result after a quantum quench [13]. After demonstrating that this relaxation occurs within a reasonable timescale (and later positing that this is possible due to smallness of off-diagonal matrix elements), the article convincingly showed that smoothness of the diagonal matrix elements as a function of energy density is the explanation for the equality in Eq. (1.5). Ref. [13] was the first step in numerically confirming the ETH, which is based on the theory of quantum chaos and RMT. Because the ETH is now well-tested numerically and well-founded mathematically in RMT (though not analytically proved), and especially since there is no equivalent foundation for what is now known about matrix elements in integrable systems (a major thrust of this thesis), it is worth briefly reviewing quantum chaos and RMT.

1.2.1 History

Classical notions of chaos do not easily apply to quantum mechanics. Exponential sensitivity to initial conditions of trajectories in phase space, the defining feature of

classically chaotic systems, is expressed using the Lyapunov exponent λ [14]:

$$\delta\mathbf{Z}(t) \approx e^{\lambda t}|\delta\mathbf{Z}(0)|. \tag{1.6}$$

If $\lambda > 0$, the system is chaotic. This definition of chaos cannot be readily used in quantum mechanical systems because they have no well-defined phase space (and therefore no phase space trajectories) due to the Heisenberg uncertainty principle. Additionally, the natural quantum analogue to a classical phase space trajectory is a wavefunction under dynamical evolution, but the overlap between two wavefunctions is always constant in time and therefore cannot exponentially diverge. There have been many attempts to reconcile the two pictures, including attempting to quantize classical chaotic trajectories (which are not closed in phase space) using the WKB quantization method [2]; we will not dwell on that here. Recently, it has become popular to use the exponential growth of out-of-time order correlators (OTOC) to define quantum chaos in a way which is reminiscent of Eq. (1.6) [15]. The OTOC is beyond the scope of this thesis, and the notion of quantum chaos presented here is based entirely on random matrix theory (RMT) and its direct implications for quantum thermalization. That said, contact has been made in the literature between the picture of quantum chaos based on OTOC and the picture based on RMT [16].

The connection between chaos and RMT was introduced by physicists who wanted to understand the spectra of complex nuclei. The initial idea, conceived by Wigner, was that the Hamiltonian of a quantum chaotic system (when represented in a generic basis) should be essentially random within a small energy window where the density of states is approximately constant [2]. Using this assumption, it was confirmed that the level spacings of complex nuclei are well-described by the Wigner-Dyson distribution, which is a key result from RMT, and it was discovered later that the level statistics of quantum systems which have a chaotic classical counterpart also follow RMT (with some exceptions) [2]. This has led to features of RMT becoming defining features of quantum chaos, even for systems which do not have any classical counterpart.

1.2.2 Gaussian Orthogonal Ensemble

The random matrix ensemble that we will focus on is the Gaussian orthogonal ensemble (GOE), because it is the one which is relevant for systems which obey time-reversal

symmetry. The probability distribution underlying the GOE is as follows:

$$P(\hat{H}) \propto \exp\left[-\frac{1}{a^2}\mathrm{Tr}\hat{H}^2\right]. \tag{1.7}$$

In (1.7), a sets an overall energy scale, and $\hat{H}$ are Hermitian matrices. It is called Gaussian because it is depends on the sum of many independent random variables, and orthogonal because $\mathrm{Tr}\hat{H}^2$ is invariant under orthogonal transformations. While when studying quantum mechanical models we do not actually have an ensemble of random matrices, or any randomness at all in the matrix elements, the quantum many-body systems we typically study have a sufficiently high dimensionality that it becomes sensible to think of their eigenvalues and eigenvectors in statistical terms. Below I state a few significant results from the GOE.

1.2.2.1 Level Spacing Statistics

The distribution which underlies the eigenvalue spacings in the GOE is called the Wigner-Dyson distribution. For a 2×2 matrix, the (normalized) distribution can be written as

$$P(\omega) = \frac{\pi}{2}\omega \exp\left[-\frac{\pi}{4}\omega^2\right], \tag{1.8}$$

where ω is the difference between the eigenvalues. The above expression assumes a mean level spacing equal to one. From this example, one can see two defining features of the Wigner-Dyson distribution: level repulsion ($P(0) = 0$) and a Gaussian tail. For general $n \times n$ matrices, Eq. (1.8) is called the Wigner surmise. In contrast to Eq. (1.8), the level spacings of quantum integrable systems obey an exponential distribution because the energy levels are uncorrelated random numbers and thus obey Poisson statistics.

1.2.2.2 Level Spacings in 1D Lattice Models

Let us show that the distributions of the level spacings of the quantum chaotic and integrable models studied later in this thesis comply with the previous theoretical predictions. We calculate the eigenvalue spectrum of a spin-chain Hamiltonian for which the $\lambda = 0$ point is the XXZ model (Δ is the anisotropy) and λ modulates next-nearest neighbor interactions and spin flipping. The Hamiltonian, with L sites and periodic boundary conditions, is

$$\hat{H} \;=\; \sum_{i=1}^{L}\left[\frac{1}{2}\left(\hat{S}_i^+\hat{S}_{i+1}^- + \mathrm{H.c.}\right) + \Delta\hat{S}_i^z\hat{S}_{i+1}^z\right]$$

$$+\lambda \sum_{i=1}^{L} \left[\frac{1}{2} \left(\hat{S}_i^+ \hat{S}_{i+2}^- + \text{H.c.} \right) + \frac{1}{2} \hat{S}_i^z \hat{S}_{i+2}^z \right], \tag{1.9}$$

where $\hat{S}_i^\nu$ are spin-1/2 operators in the $\nu \in \{x, y, z\}$ directions on site i, and $\hat{S}_i^\pm = \hat{S}_i^x \pm i\hat{S}_i^y$ are the corresponding ladder operators. As mentioned, the level spacings of a non-integrable quantum system are typically characterized by a Wigner-Dyson distribution [17], while those of an integrable one are characterized by a Poisson distribution [18]. Instead of directly using the level spacings (which requires a procedure known as "unfolding" to properly account for changes in the local density of states), we use the ratio of consecutive levels $r_n = \min(\delta_n, \delta_{n+1}) / \max(\delta_n, \delta_{n+1})$, first introduced in Ref. [19], where $\delta_n = E_{n+1} - E_n$ and the eigenenergies $\{E_n\}$ of the relevant symmetry sector form an ordered list. The probability distribution for r when $\{E_n\}$ are from the GOE is [20]:

$$P_{GOE}(r) = \frac{27}{4} \frac{r + r^2}{(1 + r + r^2)^{\frac{5}{2}}} \Theta(1 - r), \tag{1.10}$$

where $\Theta(x)$ is the Heaviside step function. On the other hand, when eigenvalues can be treated as uncorrelated random numbers as in Poisson processes, as is expected in integrable systems, the probability distribution for r is:

$$\frac{2}{(1 + r)^2} \Theta(1 - r). \tag{1.11}$$

Figure 1.1 compares the ratio of consecutive levels distributions for an integrable point ($\lambda = 0$) and a quantum chaotic one ($\lambda = 1$), both at $\Delta = 0.55$. It can be seen that the distribution in the system with $\lambda = 0$ follows the Poisson distribution, while the one with $\lambda = 1$ follows the Wigner-Dyson distribution.

1.2.2.3 Eigenvector Statistics and Entanglement Entropy

The individual coefficients of normalized eigenvectors in the GOE are Gaussian distributed in the thermodynamic limit, with a variance of $1/D$ [21]. The joint probability distribution of these coefficients is

$$P(\psi_1, \psi_2, ..., \psi_N) \propto \delta(\sum_j \psi_j^2 - 1), \tag{1.12}$$

where $\delta(x)$ is the Dirac delta function. Eq. (1.12) is justified based on the normalization requirement of eigenvectors and the invariance of the GOE under orthogonal transformations. Therefore, eigenvectors in the GOE can be said to be "essentially" random vectors

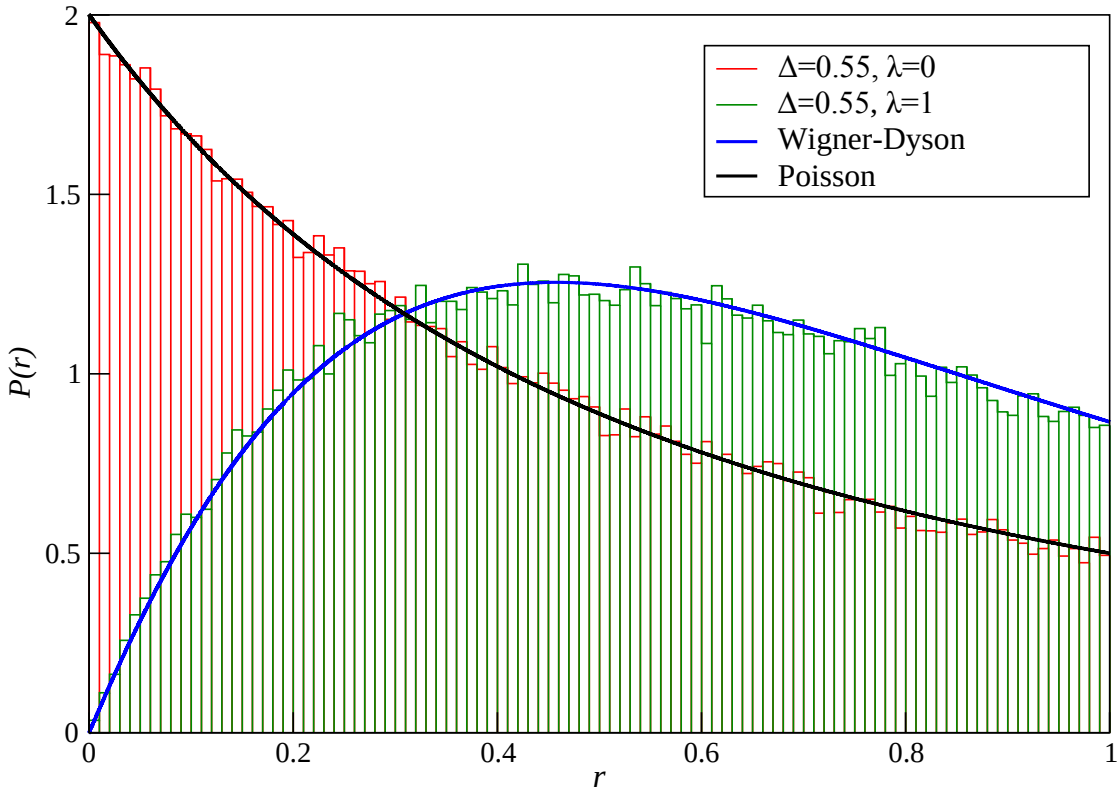

Figure 1.1 | **The distribution of the ratio of consecutive energy levels,** which is Poissonian for the Hamiltonian with $\lambda = 0$ and Wigner-Dyson for Hamiltonian with $\lambda = 1$. $\Delta = 0.55$ is used in both cases. We consider a fully resolved symmetry sector in $L = 26$ chains (see Chapter 2 for the exact specification).

in the Hilbert space.

The entanglement properties of eigenvectors in the GOE are of interest because they point to the thermal properties of these states without the need to reference observable matrix elements. In Ref. [22], the entanglement entropy of so-called random canonical states, which are states with fixed particle number[6] and Gaussian distributed coefficients (i.e. like the ones from the GOE), was studied. It was analytically and numerically demonstrated that, at half filling and for a bipartition of the system between two equal halves, they exhibit nearly maximal entanglement (with an O(1) deviation that was predicted for random pure states in Ref. [23]), and away from half filling there is a $\sqrt{L}$ deviation from maximal entanglement[7]. Thus, to leading order, the entanglement entropy

[6]They consider states on a lattice with L sites and two states per site (which correspond with the 'occupied' or 'unoccupied' designations).

[7]Maximal entanglement is the von Neumann entropy of a completely random ensemble with $\rho_{\alpha\beta} = (1/D)\delta_{\alpha\beta}$, which is also known as the infinite temperature ensemble.

of GOE eigenstates (in a physically relevant fixed particle number basis) is the same as the entropy of an infinite temperature ensemble. In the same article, these results were numerically confirmed to hold for eigenstates around the center of the spectrum of a nonintegrable quantum Hamiltonian. In Chapter 2, we extend the discussion of the entanglement entropy of eigenstates to interacting integrable systems, which will be seen to have a sub-maximal leading order term suggestive of a different universality class for the average entanglement entropy of these classes of Hamiltonians.

1.2.2.4 Operators in the Random Eigenbasis

Using a Gaussian distribution for the eigenvector coefficients, one can derive the following expression for the matrix elements of Hermitian operators in the GOE eigenbasis:

$$O_{mn} \approx \overline{O}\delta_{mn} + \sqrt{\frac{\overline{O^2}}{D}} R_{mn}, \tag{1.13}$$

where $\overline{O} = \frac{1}{D}\sum_i O_i$, $\overline{O^2} = \frac{1}{D}\sum_i O_i^2$, R_{mn} is a Gaussian-distributed random number with a variance of 2 for $m = n$ and a variance of 1 for $m \neq n$, and D is the dimension of the Hilbert space. One can see that the variance of both diagonal and off-diagonal element distributions goes to zero in the limit $D \to \infty$. Clearly, Eq. (1.5) is satisfied if one uses the above ansatz for matrix elements of observables in the GOE; one obtains $\sum_\alpha |C_\alpha|^2 O_{\alpha\alpha} \approx \overline{O}\sum_\alpha |C_\alpha|^2 = \overline{O}$. It is also important to note that, because off-diagonal elements are exponentially small compared to diagonal elements, one also expects temporal fluctuations in Eq. (1.2) to be very small. Therefore, if there is any energy scale at which a quantum mechanical system can be considered as a random matrix, an initial state which samples states from that window will thermalize in reasonable times to the predictions of the microcanonical ensemble.

1.3 Eigenstate Thermalization Hypothesis

The generalization of random matrix theory to physical systems which have structure in energy is called the eigenstate thermalization hypothesis (ETH). It manifests as a matrix element ansatz for observables and was proposed by Mark Srednicki [24], and is written as

$$O_{\alpha\beta} = O(\bar{E})\delta_{\alpha\beta} + e^{-S(\bar{E})/2} f_O(\bar{E}, \omega) R_{\alpha\beta}, \tag{1.14}$$

where $\bar{E} \equiv (E_\alpha + E_\beta)/2$, $\omega = E_\alpha - E_\beta$, and $S(\bar{E})$ is the thermodynamic entropy at energy $\bar{E}$. The functions $O(\bar{E})$ and $f_O(\bar{E}, \omega)$ are smooth, and $R_{\alpha\beta}$ is a random variable with zero mean and unit variance (variance 2) for $\alpha \neq \beta$ ($\alpha = \beta$) in Hamiltonians that exhibit time-reversal symmetry. Importantly, $O(E)$ is identical to the microcanonical prediction at energy E. It is easy to see that within small energy windows where $O(\bar{E})$ and $f_O(\bar{E}, \omega)$ are approximately constant, and at the center of the spectrum where $e^{-S(\bar{E})/2} = 1/\sqrt{D}$, Eq. (1.14) reduces to Eq. (1.13). Recently, some progress has been made in finding the regime where matrix elements become uncorrelated and true RMT behavior emerges in nonintegrable quantum spin chains [25].

Important features of Eq. (1.14) are as follows. The smoothness of the diagonal matrix elements allows observables described by Eq. (1.14) to thermalize (i.e., to be described by traditional ensembles of statistical mechanics) for experimentally relevant initial conditions. The ETH also states that the off-diagonal matrix elements are exponentially small, and this ensures equilibration (the time fluctuations of observables about the time average are small) at long times [2]. Physically, the smooth function $|f_O(\bar{E}, \omega)|^2$ is central to fluctuation-dissipation relations [2], and can be probed experimentally by measuring heating rates in periodically driven systems [1]. The ETH ansatz (1.14) has been extensively tested in exact diagonalization studies of nonintegrable Hamiltonians [2, 13, 26–41]. Further support of this ansatz will be given throughout this thesis, and Chapter 4 will explore its extension to symmetry-breaking observables. The ways in which this ansatz is broken in interacting integrable models will be explored primarily in Chapter 2 but also to some extent in later chapters.

Consider the implications of Eq. (1.14). Suppose that $O_{\alpha\alpha} = O(E_\alpha)$, i.e. that observable eigenstate expectation values (EEV) are a smooth function of the energy eigenvalues. Suppose also that C_α are narrowly distributed such that the left-hand side of (1.5) will only have contributions from α for which $E_\alpha \approx \langle E \rangle$, where $\langle E \rangle$ is the energy of an initial state. Then, Taylor expanding $O_{\alpha\alpha}$ about $\langle E \rangle$, we obtain

$$O_{\alpha\alpha} \approx O(\langle E \rangle) + \frac{dO}{d\langle E \rangle}(E_\alpha - \langle E \rangle) + \frac{1}{2}\frac{d^2O}{d\langle E \rangle^2}(E_\alpha - \langle E \rangle)^2. \tag{1.15}$$

From here, inserting into the left-hand side of (1.5), we obtain

$$\sum_\alpha |C_\alpha|^2 O_{\alpha\alpha} = O(\langle E \rangle) + \frac{1}{2}\frac{d^2O}{d\langle E \rangle^2}\langle \Delta E^2 \rangle. \tag{1.16}$$

Thus, given that $\langle \Delta E^2 \rangle$ is subextensive, the second term is negligible in the thermody-

namic limit, and we obtain

$$\sum_{\alpha} |C_\alpha|^2 O_{\alpha\alpha} \sim O(\langle E \rangle). \tag{1.17}$$

Therefore, subextensive fluctuations in energy give us (1.5).

Importantly, one can use Eq. (1.14) to show exponentially decaying time fluctuations of $O(t)$ in system size, which implies that thermalization does occur in the strong sense, although there is still the open question of how long exactly it takes for nonintegrable systems to thermalize. This is expected to be observable dependent, but not exponentially slow (in L) unless one is very close to an integrable point [42]. Thus, thermalization in quantum chaotic systems is well understood through the ETH ansatz, and has RMT as a mathematical underpinning. We next turn to integrable systems, which relax to a different ensemble (the GGE) by the mechanism of generalized eigenstate thermalization.

1.4 Generalized Gibbs Ensemble

As mentioned, integrable quantum systems do not thermalize because they have an extensive number of local conserved quantities which obstruct thermalization. The ensemble that they relax to instead is known as the generalized Gibbs ensemble (GGE), and is designed to account for the full set of conserved quantities. The form for the GGE can be found as follows:

$$\hat{\rho}_{\mathrm{GGE}} = \frac{\exp\left(-\sum_k \lambda_k \hat{I}_k\right)}{\mathrm{Tr}\left[\exp\left(-\sum_k \lambda_k \hat{I}_k\right)\right]}, \tag{1.18}$$

where $\{\hat{I}_k\}$ are the set of conserved quantities and λ_k are found by setting $\langle \hat{I}_k \rangle = \mathrm{Tr}(\hat{\rho}_{\mathrm{GGE}} \hat{I}_k) = \mathrm{Tr}(\hat{\rho}_I \hat{I}_k)$, where $\hat{\rho}_I$ is the density matrix of the initial state. The GGE was first postulated and demonstrated to be accurate for an integrable quantum system in Ref. [43].

The question is: how can we understand Eq. (1.4), which is still valid for integrable systems, in the context of the GGE? In this case, the number of parameters needed to describe the equilibrium state is only $O(L)$ when an exponentially large set (the $|C_\alpha|^2$) are expected from the diagonal ensemble. Further, as it will be demonstrated in Chapter 2, the vast majority of diagonal matrix elements of local observables are thermal in these systems. Thus, we wonder why the arguments for ETH do not cause Eq. (1.4) to be equivalent to the microcanonical ensemble. The resolution lies in the fact that the initial state samples eigenstates from a subextensive shell in all of the conserved quantities, not only the energy as in nonintegrable systems. It has been

demonstrated that if one carefully constructs a generalized microcanonical ensemble which accounts for all of the conserved quantities of an integrable Hamiltonian, one finds that its predictions are equivalent to those of the diagonal ensemble [44]. Generalized eigenstate thermalization states that the diagonal matrix elements of observables would be approximately constant within the generalized microcanonical shell, and equilibration to the generalized microcanonical ensemble follows from arguments along the lines of those in Section 1.3.

Just as in nonintegrable systems, the diagonal matrix elements of observables dictate equilibrium properties and off-diagonal matrix elements of observables dictate out-of-equilibrium properties in integrable systems. One of the biggest contributions of the work reported in this thesis to the literature is that it has deepened the understanding of matrix elements in integrable systems. See the introductions of the remaining chapters of this thesis for discussions of pre-existing work on matrix elements in integrable systems. What remains is to resolve the mathematical foundations of the behavior of matrix elements in integrable systems which, in contrast to nonintegrable ones, have no random matrix structure. We next turn to an example of the physical implications of off-diagonal matrix elements which is relevant to both nonintegrable and integrable quantum systems.

1.5 Heating Rates

One notable application of the off-diagonal matrix elements of operators in both nonintegrable and integrable quantum many-body systems is in the calculation of heating rates. Reference [1] discovered that heating rates in these systems are in excellent agreement with Fermi's golden rule which, as demonstrated in the article, is related to the spectral function $|f(\bar{E},\omega)|^2$ through the ETH ansatz (1.14). Reference [1], which goes on to show that heating rates can be used to probe the behavior of $|f(\bar{E},\omega)|^2$ in both nonintegrable and integrable systems, was an important motivation for us to carry out the detailed study of $|f(\bar{E},\omega)|^2$ in interacting integrable systems that is presented in Chapter 2. Before Refs. [1] and [45], it had been thought that the spectral function is not well-defined in integrable systems (this is still thought to be the case in noninteracting ones [29]).

In Ref. [1], the numerical linked cluster expansion (NLCE) technique was used in a periodically driven system of hard-core bosons to calculate energy as a function of driving time in the thermodynamic limit. The 1D Hamiltonian that was considered is

$\hat{H}(\tau) = \hat{H}_0 + g(\tau)\hat{K}$, with $\hat{H}_0$ and $\hat{K}$ as follows:

$$\begin{aligned}\hat{H}_0 &= \sum_i \Big[\Big(-t\,\hat{b}_i^\dagger \hat{b}_{i+1} - t'\,\hat{b}_i^\dagger \hat{b}_{i+2} + h\,\hat{b}_i^\dagger\Big) + \text{H.c.} \\ &\quad + V\left(\hat{n}_i - \frac{1}{2}\right)\left(\hat{n}_{i+1} - \frac{1}{2}\right) + V'\left(\hat{n}_i - \frac{1}{2}\right)\left(\hat{n}_{i+2} - \frac{1}{2}\right)\Big], \qquad (1.19)\\ \hat{K} &= -\sum_i \Big(\hat{b}_i^\dagger \hat{b}_{i+1} + \text{H.c.}\Big). \qquad (1.20)\end{aligned}$$

We note that $\hat{H}_0$ is integrable (and mappable onto the XXZ model) for $t' = V' = h = 0$, and nonintegrable otherwise. The function $g(\tau)$ was chosen to be a square wave $g(\tau) = g\,\mathrm{sgn}[\sin(\Omega\tau)] = \sum_{m>0} 2g_m \sin(m\Omega\tau)$, where g_m are the strengths of the individual Fourier modes. The energy as a function of driving time is defined with respect to the static Hamiltonian as in $E(\tau) = \mathrm{Tr}\left[\hat{H}_0\hat{\rho}(\tau)\right]$, where $\hat{\rho}(\tau)$ is the density matrix of a state (initially taken to be a thermal state at finite temperature) that has been evolved to stroboscopic times $\tau = nT = 2n\pi/\Omega$ ($n = 0, 1, 2, ...$). Figure 1.2, reproduced from Ref. [1], shows that $e(\tau) = E(\tau)/L$ decays exponentially toward the infinite temperature result ($E_\infty/L = 0$) for (a) nonintegrable and (b) integrable Hamiltonians at three different strengths (g) of the time-dependent perturbation $g(\tau)\hat{K}$.

More importantly for us, the insets of Fig. 1.2 show that the heating rates are quadratic in the driving parameter g and in good agreement with Fermi's golden rule, which is given by

$$\dot{E}_m(\tau) = 2\pi g_m^2 \sum_{i,f} |\,\langle E_f^0|\,\hat{K}\,|E_i^0\rangle\,|^2 (E_f^0 - E_i^0) P_i^0(\tau)\,\delta(E_f^0 - E_i^0 \pm m\Omega), \qquad (1.21)$$

where $\dot{E}_m(\tau)$ is the heating rate of Fourier mode m of the perturbation (strength g_m), $|E_i^0\rangle$ ($|E_f^0\rangle$) are the eigenstates of $\hat{H}_0$ with energies E_i^0 (E_f^0), and $P_i^0(\tau) = \langle E_i^0|\,\hat{\rho}(\tau)\,|E_i^0\rangle$ are the diagonal matrix elements of $\hat{\rho}(\tau)$ in the eigenbasis of $\hat{H}_0$. From here, the heating rate is defined as $\Gamma(\tau) = \sum_{m>0}\Gamma_m(\tau)$, where $\Gamma_m(\tau) = \dot{E}_m(\tau)/[E_\infty - E(\tau)]$ is the rate for mode m and E_∞ is the energy at infinite temperature. One can see from Eq. (1.21) that the heating rates are an important physical application of the off-diagonal matrix elements of operators.

1.6 Exact Diagonalization Studies

Here, I discuss some details of the exact diagonalization calculations reported in this thesis. The Hamiltonian of a quantum many-body system with Hilbert space dimension

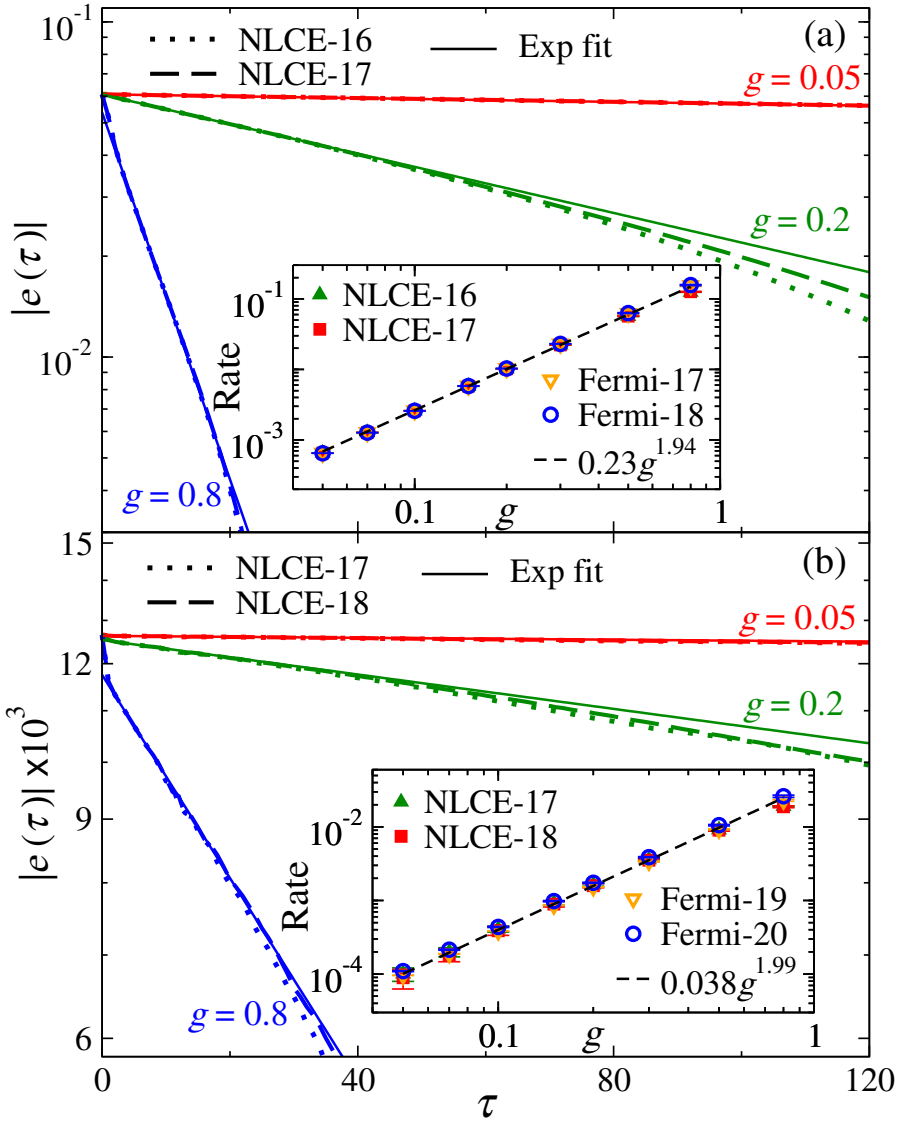

Figure 1.2 | **Heating rates, reproduced from Ref. [1].** Energy per site $|e(\tau)|$ vs τ for nonintegrable (a) and integrable (b) Hamiltonians at three different perturbation strengths $g = \{0.05, 0.2, 0.8\}$ with period $T = 1.0$ and inverse temperature of the initial state $\beta_I = (30)^{-1}$. In (a), the NLCE is computed up to order 16 (NCLE-16) and 17 (NCLE-17), while in (b) it is computed up to order 17 (NLCE-17) and 18 (NLCE-18). Exponential fits to the highest NCLE order are shown in both panels as solid lines. Insets: heating rates as a function of g. NLCE results (filled symbols) are obtained from the exponential fits to $|e(\tau)|$ vs τ. Fermi's golden rule results (open symbols) were calculated using Eq. (1.21) with results from exact diagonalization in periodic chains of length (a) 17 (Fermi-17) and 18 (Fermi-18) and (b) 19 (Fermi-19) and 20 (Fermi-20). Dashed lines are power law fits to the highest order of NLCE for $0.05 \leq g \leq 0.3$.

D is represented as a $D \times D$ matrix on the computer. In order to do this, one chooses a convenient basis of states to represent the system and perform calculations.

Most basically, we use the Fock basis $|s\rangle = |n_1, n_2, ..., n_L\rangle$, where $\{n_i\}$ are the occupation numbers of the ith site in a one-dimensional chain. We always work with spinless fermions or hard-core bosons, where only a single particle can occupy any given lattice site. Thus our states are represented as binary numbers and labeled by the corresponding base-10 integer. This basis is useful if the system has no underlying symmetries that one can take advantage of.

A brute force diagonalization of the Hamiltonian (necessary if one wants to study the bulk properties of eigenvalues and eigenvectors) scales with time $t \sim D^3$. Therefore, in most cases, we choose a computational basis which shares the symmetries of the Hamiltonian. For translationally invariant systems, which are my focus in this thesis, we use the total quasimomentum eigenstates $|k, a\rangle = \frac{1}{\sqrt{D_a}} \sum_{n=1}^{D_a} e^{-ikn} \hat{T}^n |a\rangle$, where k are quasimomenta, $\hat{T}$ is the translation operator, $|a\rangle$ is a representative Fock state (usually taken to be the state with the lowest state integer in its translation cycle), and D_a is the dimensionality of the translation cycle of $|a\rangle$. Things become more interesting (and more complicated) when one involves additional symmetries such as parity and particle-hole symmetry.

1.7 Thesis Outline

This thesis presents research that largely builds on the body of work described above that deals with the properties of matrix elements in quantum many-body systems. Our first publication (Ref. [45]) contributed significantly to the understanding of matrix elements in interacting integrable quantum systems, and will be presented in Chapter 2. This publication also served to confirm and solidify expected behaviors in quantum chaotic systems, expressed through the ETH ansatz (1.14). Additionally, this work introduced the idea that the average entanglement entropy over eigenstates can be used to differentiate between quantum chaotic and quantum integrable many-body systems.

After the publication of Ref. [45], there was a surge of interest in the low-ω properties of the spectral function $|f(\bar{E}, \omega)|^2$. This subject, while not explored in Ref. [45], needed to be thoroughly addressed. Additionally, questions started to emerge about the properties of matrix elements of observables that break translational symmetry in a translationally invariant Hamiltonian. Thus, in Ref. [46], we sought to address those gaps in our knowledge. In that paper, we discovered that symmetry-breaking operators obey the

ETH ansatz in quantum chaotic systems. Additionally, we found that they exhibit some of the behaviors found in Ref. [45] for translationally invariant operators in integrable systems. A low ω analysis of off-diagonal elements revealed differences between observables which break integrability and those which do not. The findings of Ref. [46] will be the subject of Chapter 4.

In between Refs. [45] and [46], and motivated by Ref. [47], we became interested in the emergence of eigenstate thermalization in a spin chain with a single-site defect. In Chapter 3, we demonstrate that a local impurity indeed results in eigenstate thermalization, but that the thermodynamic and transport properties remain the same as those of the unperturbed system. Lastly, in Chapter 5, which focuses on Ref. [48], we seek to address universal behavior in the onset of quantum chaos by studying the behavior of two different models, the perturbed XXZ model and the perturbed Anderson insulator.

This thesis closely follows the publications noted above, with modifications introduced to avoid redundancy.

Chapter 2
Entanglement and Matrix Elements of Observables in Interacting Integrable Systems

2.1 Introduction

Much work has been done in the last decade to understand the far-from-equilibrium dynamics and description after equilibration of isolated nonintegrable (generic) and integrable quantum many-body systems [2, 49, 50]. Despite tremendous progress in recent years [51–60], the microscopics of interacting integrable systems are those which remain less understood. On the one hand, interactions are present in those systems as in nonintegrable ones (making their study challenging), and on the other hand, they exhibit extensive numbers of local conserved quantities as noninteracting systems do. The presence of such quantities precludes thermalization in integrable (noninteracting and interacting) quantum systems [6, 43, 61–63].

Thermalization does occur in generic isolated quantum systems, and is understood to be a consequence of quantum chaos and eigenstate thermalization [2, 13, 64, 65]. Essentially, the matrix elements of observables (few-body operators) $\hat{O}$ in eigenstates of generic quantum Hamiltonians are described by the eigenstate thermalization hypothesis (ETH) ansatz (1.14). The ETH ansatz (1.14) has been extensively tested in exact diagonalization studies of nonintegrable Hamiltonians [2, 13, 26–41]. While the diagonal matrix elements display a shrinking support and an exponentially decaying variance with increasing system size in nonintegrable systems, confirming that the diagonal ETH is valid for them, the same is not true in integrable systems [26–28, 31, 41, 44, 56]. In

integrable systems, the support of the diagonal matrix elements need not shrink, and their variance is expected to decay as a power law in system size [66–68]. The latter is consistent with the fact that the variance of the diagonal matrix elements of intensive translational invariant observables must vanish at least as a power law in system size because it is bounded from above by the Hilbert-Schmidt norm (which vanishes as a power law in system size) [41].

The off-diagonal matrix elements of observables in the eigenstates of interacting integrable quantum many-body systems have received little attention. While some results have been reported for specific models and system sizes alongside those of quantum chaotic systems [27, 28, 35], there has been no systematic study of their properties. For noninteracting models (or models mappable to them), the existence of an increasingly large (with increasing system size) fraction of vanishing off-diagonal matrix elements precludes the definition of a meaningful function $f_O(\bar{E}, \omega)$, in contrast to quantum chaotic models [29]. On the other hand, recent results in the context of periodically driven systems provided strong evidence that one can define (and experimentally measure) a function $|f_O(\bar{E}, \omega)|^2 = e^{S(\bar{E})}\overline{|O_{\alpha\beta}|^2}$ for interacting integrable models [1]. Exploring this, along with other properties of the off-diagonal (and diagonal) matrix elements in the spin-1/2 XXZ chain, is one of the two central goals of this chapter.

The other central goal of this chapter is to study the structure of highly-excited energy eigenstates by means of their bipartite entanglement. Recently, much work has been devoted to understanding entanglement properties of highly-excited eigenstates of many-body Hamiltonians [22, 69–103]. Here we study the average entanglement entropy over all eigenstates of the spin-1/2 XXZ Hamiltonian in the zero-magnetization sector. We argue that this average universally reveals the fundamentally different natures of interacting integrable and quantum chaotic models. While in both nonintegrable and interacting integrable systems the leading term of the average entanglement entropy exhibits a volume-law scaling, we show that the corresponding volume-law coefficient is markedly different between the two. In quantum chaotic systems [22] it matches the prediction by Page [23] for random pure states in the Hilbert space, while it is smaller for interacting integrable systems. Remarkably, our results for interacting spin-1/2 integrable systems are consistent with this coefficient being very close to, or the same as, the one for translationally invariant free [80] and (more generally) quadratic [87, 89] fermionic Hamiltonians. This suggests that, entanglement-wise, the overwhelming majority of the eigenstates are very similar between interacting spin-1/2 integrable Hamiltonians and noninteracting fermionic Hamiltonians.

The presentation is organized as follows: In Sec. 2.2, we discuss the specific integrable and nonintegrable models and observables considered, as well as details about the numerical calculations carried out. In Sec. 2.3, we compare the average entanglement entropy of eigenstates of the spin-1/2 XXZ chain with that of eigenstates of noninteracting and nonintegrable models. In Sec. 2.4, we discuss the distributions and scaling properties of the diagonal matrix elements of two local observables at the center of the spectrum. In Sec. 2.5, we discuss the off-diagonal matrix elements of the same observables: their distributions, scaling properties, and functional dependence of $|f_O(\bar{E},\omega)|^2$ on ω, for $\bar{E}$ at the center of the spectrum. Lastly, in Sec. 2.6, we summarize our results.

2.2 Model and Observables

We study the spin-1/2 XXZ chain with the addition of next-nearest neighbor interactions, with L sites and periodic boundary conditions. The Hamiltonian is

$$\begin{aligned}\hat{H} &= \sum_{i=1}^{L}\left[\frac{1}{2}\left(\hat{S}_i^+\hat{S}_{i+1}^- + \text{H.c.}\right) + \Delta\hat{S}_i^z\hat{S}_{i+1}^z\right] \\ &\quad +\lambda\sum_{i=1}^{L}\left[\frac{1}{2}\left(\hat{S}_i^+\hat{S}_{i+2}^- + \text{H.c.}\right) + \frac{1}{2}\hat{S}_i^z\hat{S}_{i+2}^z\right], \end{aligned} \tag{2.1}$$

where $\hat{S}_i^\nu$ are spin-1/2 operators in the $\nu \in \{x, y, z\}$ directions on site i, and $\hat{S}_i^\pm = \hat{S}_i^x \pm i\hat{S}_i^y$ are the corresponding ladder operators. When $\lambda = 0$, Hamiltonian (2.1) is integrable and can be solved exactly using Bethe ansatz [104]. When $\lambda \neq 0$, Hamiltonian (2.1) is quantum chaotic [105]. We set $\lambda = 0$ and 1 to compare the integrable and nonintegrable regimes, respectively. Unless otherwise specified, we show results for $\Delta = 0.55$ and $\Delta = 1.1$ to illustrate that they are qualitatively similar in the (nearest-neighbor) easy-plane ($\Delta < 1$) and easy-axis ($\Delta > 1$) regimes.

We study the matrix elements of two local operators: The nearest neighbor z-interaction

$$\hat{A} = \frac{1}{L}\sum_{i=1}^{L}\hat{S}_i^z\hat{S}_{i+1}^z, \tag{2.2}$$

and the next-nearest neighbor flip-flop operator

$$\hat{B} = \frac{1}{L}\sum_{i=1}^{L}\left(\hat{S}_j^+\hat{S}_{j+2}^- + \text{H.c.}\right). \tag{2.3}$$

To study the entanglement entropy of energy eigenstates, as well as the matrix

elements of $\hat{A}$ and $\hat{B}$ in those eigenstates, it is important to resolve all the symmetries of the Hamiltonian [2, 28]. First, we note that Hamiltonian (2.1) conserves the total magnetization in the z-direction, $M^z = \sum_i \hat{S}_i^z$. In this chapter we focus on the zero magnetization sector in chains with even numbers of lattice sites. The next important symmetry is translation, which allows one to block diagonalize the Hamiltonian in different total quasimomentum k sectors. All quasimomentum sectors are used in the average entanglement entropy calculations reported in Sec. 2.3. Within the $M^z = 0$ and $k = 0$ sector, there are two further symmetries, namely, spin inversion (Z_2) and space reflection (P). In our studies of matrix elements we focus on the even-Z_2 even-P sector within the $M^z = 0$ and $k = 0$ sector. We use full exact diagonalization of periodic chains with up to $L = 26$ sites. The even-Z_2 even-P sector within the $M^z = 0$ and $k = 0$ sector of the chain with $L = 26$, the largest considered, has $101,340$ states.

2.3 Entanglement Entropy

In this section, we study the entanglement properties of eigenstates $\{|\alpha\rangle\}$ of Hamiltonian (2.1) in the zero magnetization sector. We consider a bipartition into a subsystem A and its complement $\bar{A}$ that consist of L_A and $L - L_\mathrm{A}$ consecutive lattice sites, respectively. We calculate the bipartite entanglement entropy of an eigenstate $|\alpha\rangle$ as

$$S_\alpha = -\mathrm{Tr}\{\hat{\rho}_A \ln(\hat{\rho}_A)\}\,, \tag{2.4}$$

where $\hat{\rho}_A = \mathrm{Tr}_{\bar{A}}\{|\alpha\rangle\langle\alpha|\}$ is the reduced density matrix of the subsystem A. We average S_α over all Hamiltonian eigenstates in the zero magnetization sector to obtain the average entanglement entropy $\bar{S} = \mathcal{D}^{-1}\sum_\alpha S_\alpha$, where $\mathcal{D} = \binom{L}{L/2}$. The upper bound for the entanglement entropy of pure states in a given magnetization sector (or, equivalently, in a given particle-number sector when mapping spin-1/2 systems onto hard-core bosons or spinless fermions), for a given L_A/L, depends both on the magnetization and on L_A/L. The leading term, which scales with the volume, depends on the magnetization [22, 85]. There is also a subleading, $O(1)$, term that depends on L_A/L [22].

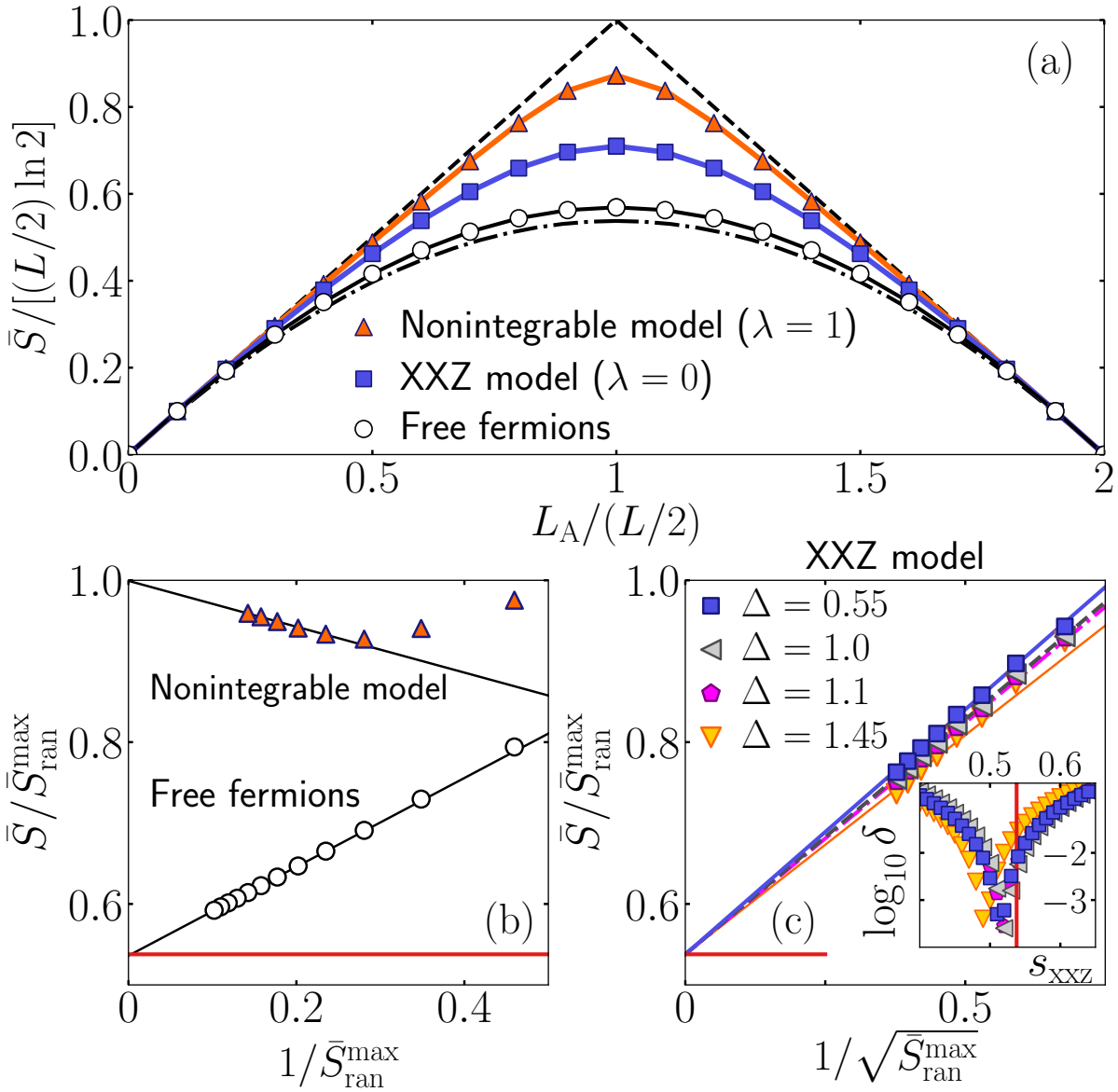

Figure 2.1 | **Average entanglement entropy** $\bar{S}$**,** in the zero-magnetization sector (half filling for free fermions), for three paradigms of many-body quantum systems: the spin-1/2 XXZ model [$\lambda = 0$ in Eq. (2.1), an interacting integrable model], a nonintegrable model [$\lambda = 1$ in Eq. (2.1)], and free fermions [which are mappable to the spin-1/2 XX spin chain, Eq. (2.1) with $\Delta = \lambda = 0$]. (a) $\bar{S}$ vs L_A for $L = 20$ ($\Delta = 0.55$ in the interacting models). The dashed line shows the results for random pure states from Eq. (2.5) in the thermodynamic limit. The dashed-dotted line is the average for free fermions in all particle sectors at $L = 36$ (the same results reported in Fig. 1 in Ref. [80]). Panels (b) and (c) show finite-size scaling analyses at $L_A/L = 1/2$. We normalize $\bar{S}$ by $\bar{S}^{max}_{ran} \equiv \bar{S}_{ran}\left(\frac{L}{2}, \frac{1}{2}\right)$, see Eq. (2.5), and plot the results vs $\bar{S}^{max}_{ran}$ to show that $\bar{S} = \bar{S}^{max}_{ran}$ for the nonintegrable model in the thermodynamic limit and to improve the scaling analyses in our small systems. (b) Normalized averages as functions of $1/\bar{S}^{max}_{ran}$ at the nonintegrable point and for free fermions. Lines are two-parameter fits to $c_0 + c_1/\bar{S}^{max}_{ran}$

with $c_0 = 0.999$ (with 1 minus the coefficient of determination, $1 - R^2 = 4.3 \times 10^{-3}$) and $c_0 + c_1/\bar{S}_{\rm ran}^{\rm max}$ with $c_0 = 0.536$ (with $1 - R^2 = 2.5 \times 10^{-5}$), respectively, for $L \geq 14$. (c) Normalized averages at $\Delta = 0.55$, 1.0, 1.1, and 1.45 in the spin-1/2 XXZ model as functions of $1/\sqrt{\bar{S}_{\rm ran}^{\rm max}}$. Lines are single-parameter fits to the function $s_{\rm free}\left(\frac{1}{2}\right) + d_1/\sqrt{\bar{S}_{\rm ran}^{\rm max}}$ for systems with $L \geq 14$. Inset in (c), $\delta = 1 - R^2$ of the fits to $s_{\rm xxz} + d_1/\sqrt{\bar{S}_{\rm ran}^{\rm max}}$ as a function of the volume-law coefficient $s_{\rm xxz}$ chosen. Note that the minima are very close to $s_{\rm free}\left(\frac{1}{2}\right)$ for $\Delta \simeq 1$, and depart from that value as the quality of the fit worsens when departing from $\Delta = 1$ (presumably because of stronger finite-size effects).

In the zero magnetization sector, for $L_A \leq L/2$, the leading and first subleading terms in the average entanglement entropy of random pure states with normally distributed real coefficients are [22]

$$\begin{aligned} \bar{S}_{\rm ran}\left(L_{\rm A}, \frac{L_{\rm A}}{L}\right) &= L_{\rm A}\ln(2) + \frac{\frac{L_{\rm A}}{L} + \ln(1-\frac{L_{\rm A}}{L})}{2} - \frac{1}{2}\frac{\sum_{n_{\rm A}=0}^{L_{\rm A}}\binom{L_{\rm A}}{n_{\rm A}}^2}{\binom{L}{L/2}} \\ &= L_{\rm A}\ln(2) + \frac{\frac{L_{\rm A}}{L} + \ln(1-\frac{L_{\rm A}}{L})}{2} - \frac{1}{2}\frac{\binom{2L_{\rm A}}{L_{\rm A}}}{\binom{L}{L/2}}\,. \end{aligned} \tag{2.5}$$

On the r.h.s. of Eq. (2.5), the first two terms are the upper bound for the entanglement entropy of pure states in the $M^z = 0$ sector [22], while the third term is the generalization of the correction derived by Page [23] for the $M^z = 0$ sector of a system with conserved M^z. Motivated by the numerical results in Ref. [22], we think of $\bar{S}_{\rm ran}\left(L_{\rm A}, \frac{L_{\rm A}}{L}\right)$ as an upper bound for the average entanglement entropy over all eigenstates of any given physical Hamiltonian, with $\bar{S}_{\rm ran}^{\rm max} \equiv \bar{S}_{\rm ran}\left(\frac{L}{2}, \frac{1}{2}\right)$ as the maximum. The dashed line in Fig. 2.1(a) shows $\bar{S}_{\rm ran}\left(L_{\rm A}, \frac{L_{\rm A}}{L}\right)$ in the thermodynamic limit.

On the opposite (low-entropy) side of physical Hamiltonians one has noninteracting (free) fermions. Translationally invariant free fermionic Hamiltonians exhibit the same leading term of the average entanglement entropy as the XX model, Eq. (2.1) with $\Delta = \lambda = 0$ [89]. It was proved in Ref. [80] that the leading (volume) term of the average entanglement entropy over all (i.e., including all particle-number sectors) eigenstates in those models is

$$\bar{S}_{\rm free}\left(L_{\rm A}, \frac{L_{\rm A}}{L}\right) = s_{\rm free}\left(\frac{L_{\rm A}}{L}\right) L_{\rm A}\ln 2, \tag{2.6}$$

with $s_{\rm free}(0) = 1$, and $0 < s_{\rm free}\left(\frac{L_{\rm A}}{L}\right) < 1$ for $L_{\rm A}/L > 0$. In Ref. [80], $s_{\rm free}\left(\frac{L_{\rm A}}{L}\right)$ was

computed numerically [dashed-dotted line in Fig. 2.1(a)] and, for $L_{\rm A} = L/2$, it was found that $s_{\rm free}\left(\frac{1}{2}\right) = 0.5378(1)$. Subsequently, it was conjectured that $s_{\rm free}\left(\frac{L_{\rm A}}{L}\right)$ is universal for all translationally invariant quadratic fermionic models [87, 89]. The horizontal lines in Figs. 2.1(b) and 2.1(c) show $s_{\rm free}\left(\frac{1}{2}\right)/\bar{S}^{\rm max}_{\rm ran}$.

In Fig. 2.1(a), we show the average entanglement entropy over all eigenstates within the half-filled sector of noninteracting fermions, as well as within the zero-magnetization sector of integrable ($\Delta = 0.55$ and $\lambda = 0$) and nonintegrable ($\Delta = 0.55$ and $\lambda = 1$) points of Eq. (2.1), for chains with $L = 20$. The results at the nonintegrable point are closest to the thermodynamic limit ones for random pure states. Figure 2.1(b), for $L_{\rm A}/L = 1/2$, shows that the small differences seen in Fig. 2.1(a) appear to vanish in the thermodynamic limit, in agreement with complementary results reported in Ref. [22]. For free fermions, on the other hand, the results in Fig. 2.1(a) are closest to the thermodynamic limit ones obtained in Ref. [80] by averaging over all fillings. Figure 2.1(b), for $L_{\rm A}/L = 1/2$, shows that the differences seen in Fig. 2.1(a) appear to vanish in the thermodynamic limit as expected (the zero magnetization sector is the one dominant in the thermodynamic limit when averaging over all fillings).

The numerical results at the interacting integrable point ($\Delta = 0.55$) in Fig. 2.1(a) are in between the ones for random pure states and the noninteracting ones. However, the finite-size scaling analysis reported in Fig. 2.1(c) for $L_{\rm A}/L = 1/2$ suggests that the leading term of the average entanglement entropy at $\Delta = 0.55$ (easy-plane regime) is very close to, or the same as, the one for noninteracting fermions. As a matter of fact, finite-size scaling analyses in Fig. 2.1(c) for $\Delta = 1.1$, 1.45 (easy-axis regime) and $\Delta = 1.0$ (Heisenberg point, the most symmetric point in the spin-1/2 XXZ model) suggest that this is true independently of the value of Δ.

The finite-size scaling analyses in Figs. 2.1(b) and 2.1(c) suggest that the qualitatively new effect of interactions in integrable systems is subleading, as they change the first subleading term from $O(1)$ in noninteracting models [the leading correction to $\bar{S}/\bar{S}^{\rm max}_{\rm ran}$ in Fig. 2.1(b) is $\propto 1/L_{\rm A}$] to $O(\sqrt{L_{\rm A}})$ in interacting integrable models [the leading correction to $\bar{S}/\bar{S}^{\rm max}_{\rm ran}$ in Fig. 2.1(c) is $\propto 1/\sqrt{L_{\rm A}}$].

2.4 Diagonal Matrix Elements

In this section, we study expectation values of observables in eigenstates of interacting integrable and nonintegrable Hamiltonians, referred to in what follows as the eigenstate expectation values of the observables, in the even-Z_2 even-P sector within the $M^z = 0$

and $k = 0$ sector (see Sec. 2.2).

In Fig. 2.2, we show the eigenstate expectation values of observables $\hat{A}$ and $\hat{B}$ as functions of the eigenenergies per site (E_α/L) for different chain sizes at integrable [Figs. 2.2(a) and 2.2(c)] and nonintegrable [Figs. 2.2(b) and 2.2(d)] points of Hamiltonian (2.1). At the nonintegrable point, for both observables, one can see in the plots that the support (maximum spread) of the eigenstate expectation values around each E_α/L (away from the edges of the spectrum) shrinks upon increasing the chain size L. The scaling of a quantifier of the support, see the insets in Figs. 2.2(b) and 2.2(d), indicates that the support vanishes exponentially fast with increasing L. This suggests that, in the thermodynamic limit, the eigenstate expectation values are described by the smooth function $O(E)$, which, in turn, is the thermal expectation value of observable $\hat{O}$ at energy E [2]. Hence, one expects all eigenstate expectation values at the nonintegrable point away from the edges of the spectrum to be thermal in the thermodynamic limit. On

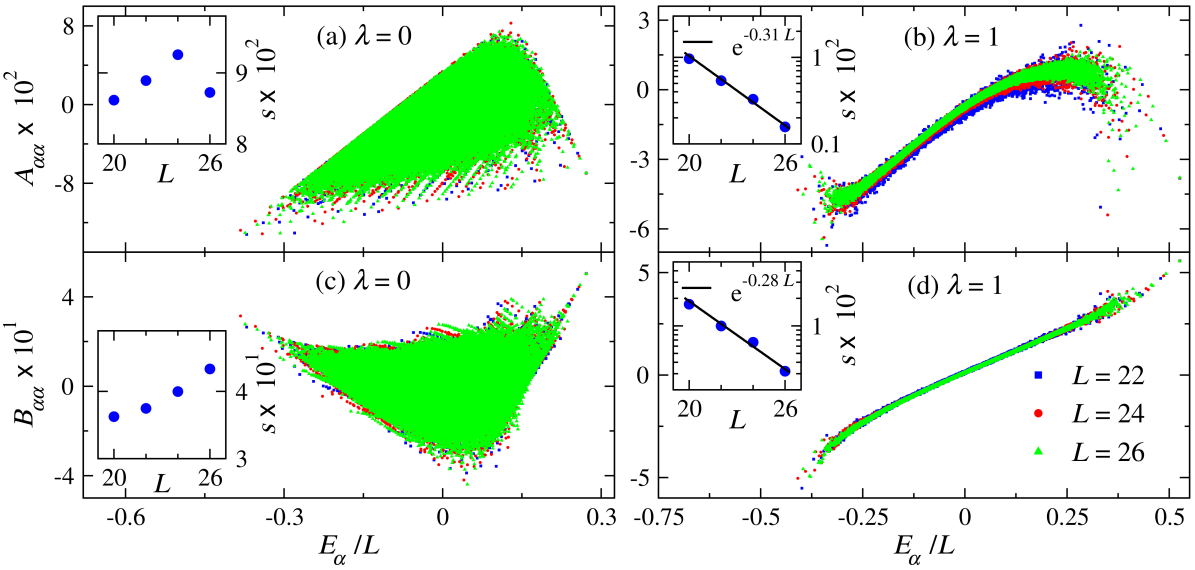

Figure 2.2 | **Eigenstate expectation values ($O_{\alpha\alpha}$) vs the eigenstate energies per site E_α/L for each eigenstate $|\alpha\rangle$.** We consider local observables $\hat{A}$ [(a) and (b), see Eq. (2.2)] and $\hat{B}$ [(c) and (d), see Eq. (2.3)] at integrable [(a) and (c), $\lambda = 0$] and nonintegrable [(b) and (d), $\lambda = 1$] points of Hamiltonian (2.1). Results are shown for chains with $L = 22$, 24, and 26 sites, and are superposed to demonstrate non-shrinking (shrinking) support in the integrable (nonintegrable) case. $\Delta = 0.55$ in all plots (qualitatively similar results were obtained, not shown, for other values of Δ). (Insets) A quantifier for the support of the eigenstate expectation values, $s = \max(\left|O_{\alpha\alpha} - \overline{O_{\alpha\alpha}}\right|)$, where $\overline{O_{\alpha\alpha}}$ is the running average over 201 eigenstate expectation values centered at $O_{\alpha\alpha}$ and $\max(\cdot)$ is taken over the central 50% of the spectrum, plotted as a function of L.

the other hand, at integrability, Figs. 2.2(a) and 2.2(c) show that the support of the eigenstate expectation values is wide and does not shrink with increasing system size [see the insets in Figs. 2.2(a) and 2.2(c)]. The wide nonshrinking support indicates that at the integrable point ETH is not satisfied, as nonthermal states persist in the thermodynamic limit. The next question to address at the integrable point is how those

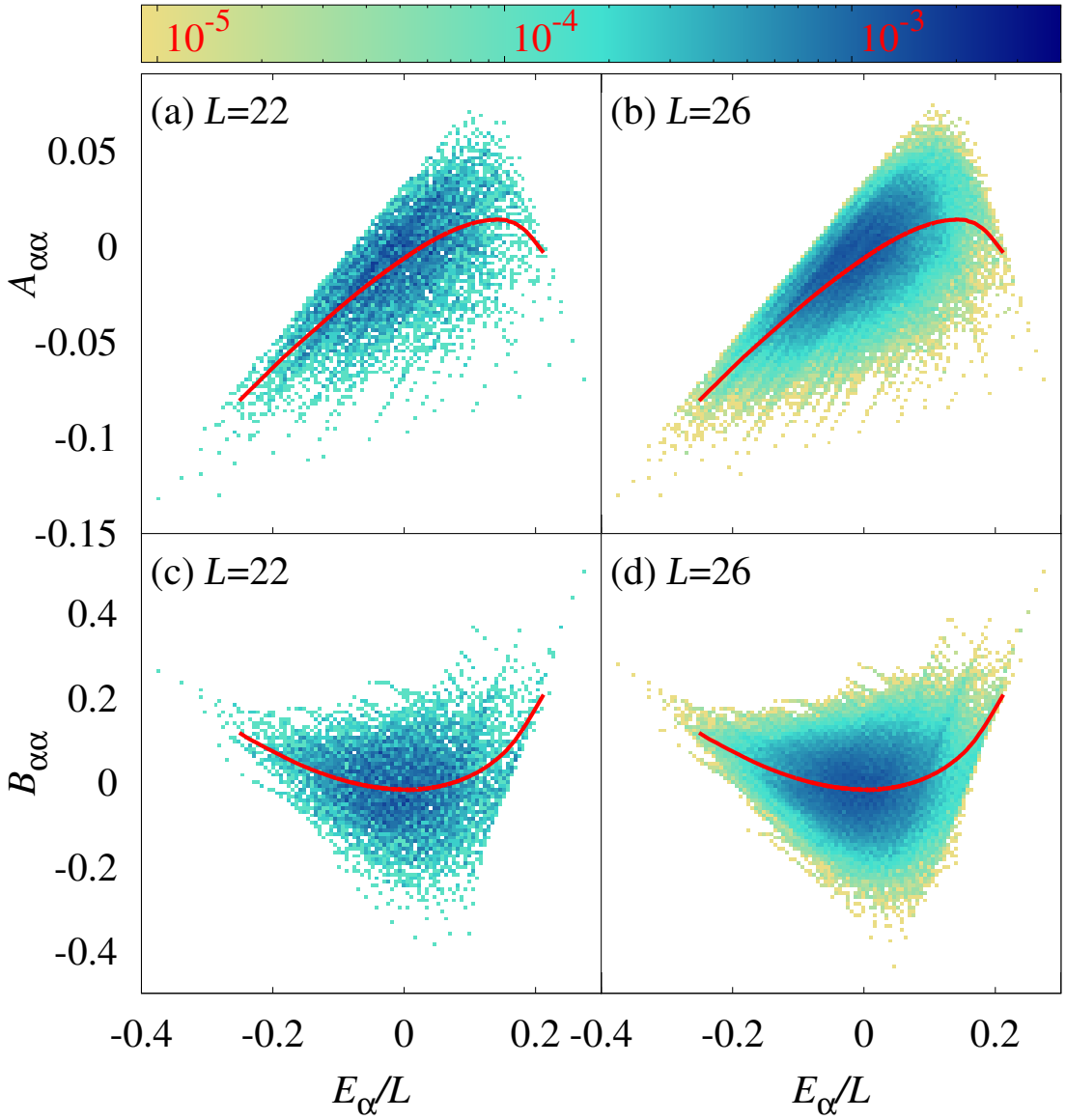

Figure 2.3 | **Normalized 2D histograms of the eigenstate expectation values as functions of E_α/L.** We consider local observables $\hat{A}$ [(a) and (b)] and $\hat{B}$ [(c) and (d)] at the integrable point ($\Delta = 0.55$ and $\lambda = 0$) of Hamiltonian (2.1). We show the microcanonical average (calculated for $L = 26$ using $\delta E/L = 0.05$) as a solid (red) line. Results are reported for $L = 22$ [(a) and (c)] and $L = 26$ [(b) and (d)].

eigenstate expectation values are distributed.

In Fig. 2.3, we show the normalized distribution (color coded) of the eigenstate expectation values for observables $\hat{A}$ and $\hat{B}$ for two different system sizes ($L = 22$ and 26) at the integrable point in Fig. 2.2, along with the microcanonical averages (solid lines) for the respective observables. The microcanonical averages are calculated using the results from $L = 26$ in an energy window δE that is small enough to yield a smooth curve independent of δE. By comparing the results for $L = 22$ and $L = 26$ for each observable, one can see that, despite the large non-vanishing support, the distribution of eigenstate expectation values (on the y-axis) becomes increasingly peaked (with increasing system size) about the microcanonical average (further evidence for this is reported in Fig. 2.5). Similarly, on the x-axis, the distribution becomes increasingly peaked about the center of the spectrum ($E_\alpha/L = 0$). The latter occurs because of the known Gaussian behavior of the density of states in local Hamiltonians [2, 106, 107].

In Fig. 2.4, we plot the many-body density of states DOS(E_α) as a function of the energy per site E_α/L at integrable and nonintegrable points along with Gaussian functions that have the same mean and variance as the data. The Gaussian functions agree well with the numerical results. This makes it apparent that, even for the small chains that one can solve using full exact diagonalization, the density of states is very close to a Gaussian function (away from the edges of the spectrum). This is true regardless of whether the Hamiltonian is integrable or not. The insets show that the variances in our calculations decay as a power law in L, with a power that is close to the expected L^{-1} behavior. This shows that, with increasing system size, the overwhelming majority of eigenstates of local Hamiltonians are at the center of the spectrum (with a vanishing energy per site in our case). In what follows, we focus our scaling analyses on that region of the spectrum ($E_\alpha/L \simeq 0$).

To quantify the differences seen in Fig. 2.2 between the eigenstate expectation values of observables in integrable and nonintegrable systems, we study the average of the absolute value of the eigenstate-to-eigenstate fluctuations [34, 36, 40]

$$\overline{|\delta O_{\alpha\alpha}|} = \overline{|O_{\alpha\alpha} - O_{\alpha+1\alpha+1}|}\,, \tag{2.7}$$

where the index α labels the eigenenergies E_α (sorted in increasing order), and $\overline{|\ldots|}$ denotes an average over the central 20% of eigenstates. To carry out an accurate comparison between our results for $\overline{|\delta O_{\alpha\alpha}|}$ and the ETH ansatz for quantum chaotic systems, a modification needs to be introduced to the ansatz in order to tailor it to

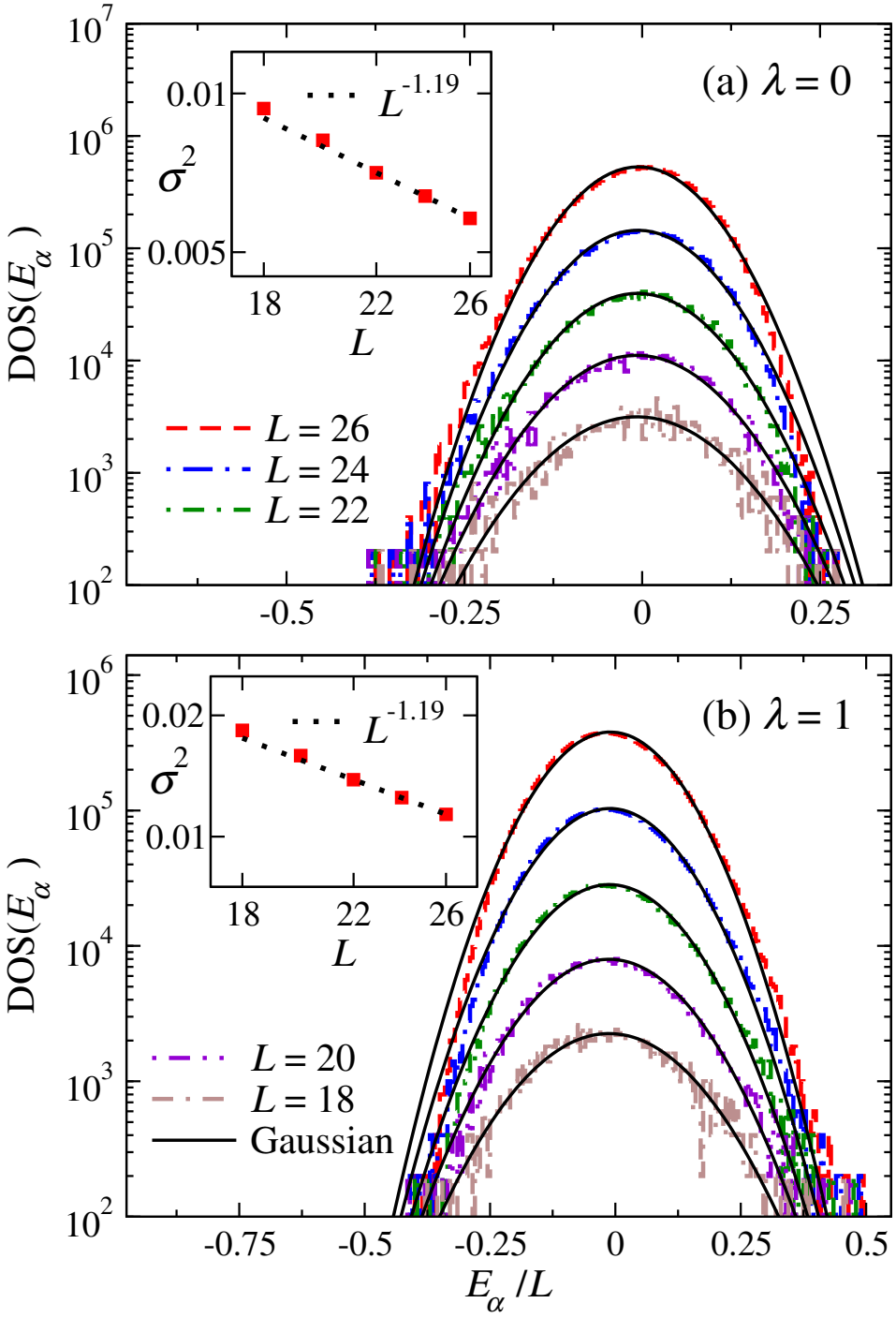

Figure 2.4 | **Densities of states (DOS) as functions of E_α/L.** We consider chain lengths $L = 18$ through $L = 26$ at integrable [(a), $\lambda = 0$] and nonintegrable [(b), $\lambda = 1$] points ($\Delta = 0.55$). The black lines are Gaussian functions with the same mean and variance as the data. (Insets) Variances of the data vs L, along with power law fits of the variances to $c_1 L^{-c_2}$.

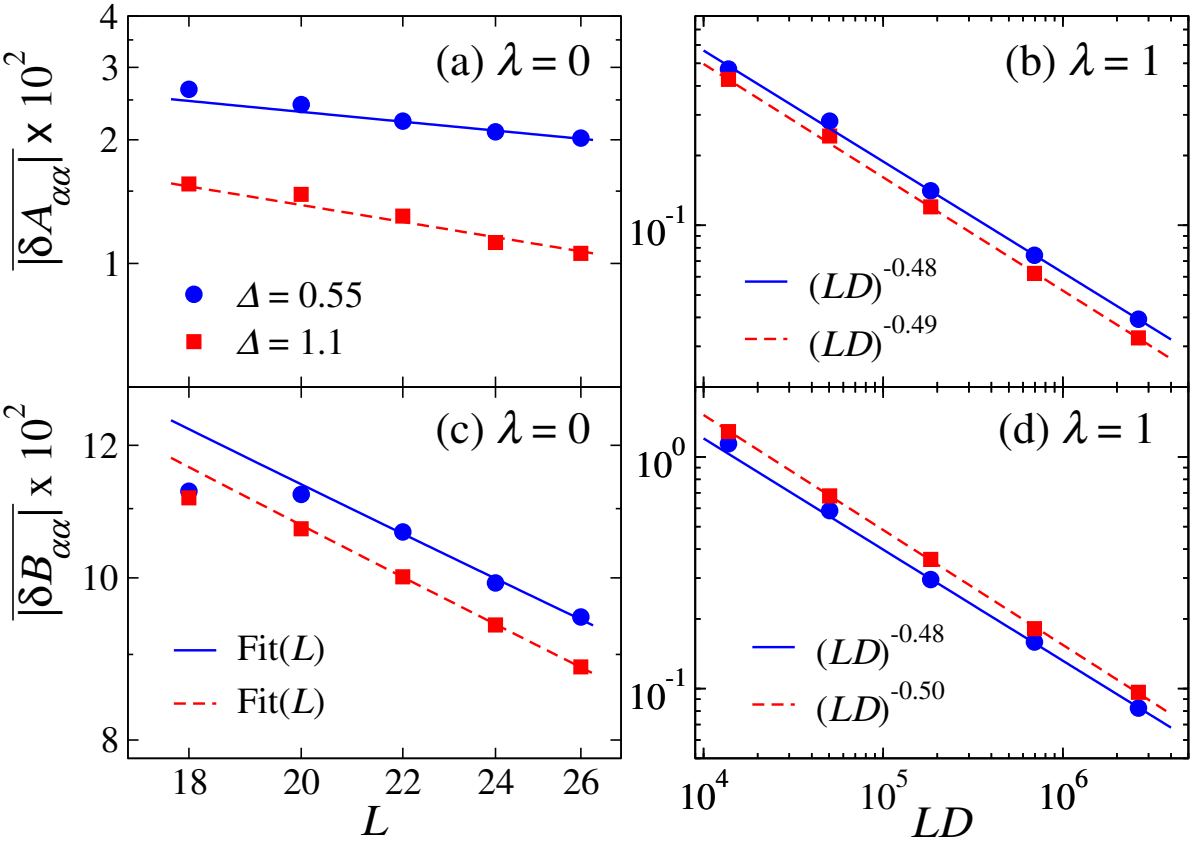

Figure 2.5 | **Scaling of the average eigenstate-to-eigenstate fluctuations of diagonal matrix elements,** $\overline{|\delta O_{\alpha\alpha}|}$ [see Eq. (2.7)], for $\hat{A}$ [(a) and (b)] and $\hat{B}$ [(c) and (d)] at two integrable [(a) and (c), $\lambda = 0$] and two nonintegrable [(b) and (d), $\lambda = 1$] points of Hamiltonian (2.1). We report results for $\Delta = 0.55$ and $\Delta = 1.1$. The symbols show the numerical results, while the lines depict fits to the functions fit$(L) = c_1/\sqrt{L} + c_2/L$ [(a) and (c)] and $c_1(LD)^{-c_2}$ [(b) and (d)] for $L = 22$ through $L = 26$.

our observables of interest. This modification is related to the fact that we focus on intensive operators that are defined via extensive sums, as seen in Eqs. (2.2) and (2.3), in the presence of translational invariance. The Hilbert-Schmidt norm of those operators scales as $1/\sqrt{L}$ [41], as opposed to the $O(1)$ Hilbert-Schmidt norm one has in mind when writing Eq. (1.14). As a result, for the diagonal part of our operators $\hat{A}$ and $\hat{B}$, Eq. (1.14) needs to be rewritten as:

$$O_{\alpha\alpha} = O(E_\alpha) + \frac{e^{-S(E_\alpha)/2}}{\sqrt{L}} f_O(E_\alpha, 0) R_{\alpha\alpha} \,. \tag{2.8}$$

Since we are focusing on the regime $E_\alpha/L \simeq 0$, in which $S(E_\alpha) \simeq \ln(D)$ (D is the dimension of the Hilbert space of the symmetry sector studied), we expect the average

eigenstate to eigenstate fluctuations of $\hat{O}$ to be $\propto (LD)^{-1/2}$. For integrable systems, on the other hand, the average eigenstate-to-eigenstate fluctuations are expected to be proportional to $1/\sqrt{L}$ [68].

In Fig. 2.5, we show the finite size scaling of $\overline{|\delta A_{\alpha\alpha}|}$ [Figs. 2.5(a) and 2.5(b)] and $\overline{|\delta B_{\alpha\alpha}|}$ [Figs. 2.5(c) and 2.5(d)] at two integrable [Figs. 2.5(a) and 2.5(c), $\lambda = 0$] and two nonintegrable [Figs. 2.5(b) and 2.5(d), $\lambda = 1$] points. For the nonintegrable points, we observe a near perfect scaling $\propto 1/\sqrt{LD}$ for both observables. This is in agreement with the ETH ansatz and indicates that the scaling is robust against the parameters of the model and the choice of observables. On the other hand, at integrability, $\overline{|\delta A_{\alpha\alpha}|}$ and $\overline{|\delta B_{\alpha\alpha}|}$ exhibit a much slower decay with increasing system size, and also exhibit very strong finite-size effects. While we expect the decay to be $\propto 1/\sqrt{L}$ [68], this is not the exponent of the power law we find if we fit the data to $c_1 L^{-c_2}$. Instead, we have fitted the data to the function $\text{fit}(L) = c_1/\sqrt{L} + c_2/L$ and find a reasonably good agreement. This suggests that higher powers of $1/\sqrt{L}$ still play an important role in the system sizes accessible to us through full exact diagonalization.

2.5 Off-Diagonal Matrix Elements

In this section, we study the off-diagonal matrix elements of observables in the eigenstates of Hamiltonian (2.1). We focus on their distributions, scaling properties, and functional dependence of $|f_O(\bar{E} \simeq 0, \omega)|^2$ on ω, for eigenstates that are in the even-Z_2 even-P sector within the $M^z = 0$ and $k = 0$ sector (see Sec. 2.2).

2.5.1 Distribution

We first study the distribution of off-diagonal matrix elements of observables $\hat{A}$ and $\hat{B}$ within 200 energy eigenstates at the center of the spectrum of a chain with $L = 26$ sites. In this eigenstate window, $\bar{E} = (E_\alpha + E_\beta)/2 \simeq 0$ and $\omega = |E_\alpha - E_\beta| \simeq 0$. For nonintegrable systems, this window is small enough to have $f_O(\bar{E}, \omega)$ approximately constant, so that the probability distribution of $O_{\alpha,\beta}$ is determined by $R_{\alpha,\beta}$.

In Fig. 2.6 we show the probability distributions of $A_{\alpha\beta}$ and $B_{\alpha\beta}$ at integrable and nonintegrable points of Hamiltonian (2.1), with $\Delta = 0.55$. At the nonintegrable point, Figs. 2.6(b) and 2.6(d) clearly show that the numerical results are well described by Gaussian distributions, as expected. At the integrable point, on the other hand, the distributions are fundamentally different [Figs. 2.6(a) and 2.6(c)]. While they also

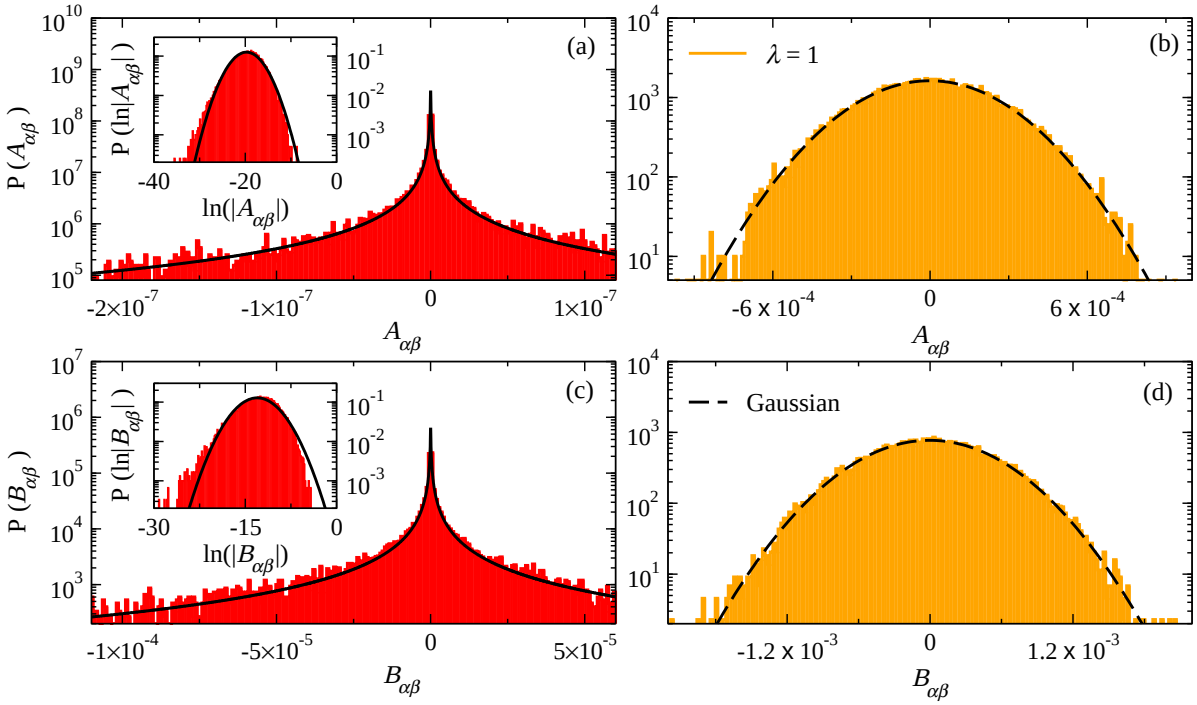

Figure 2.6 | **Probability distributions $P(O_{\alpha\beta})$ for off-diagonal matrix elements.** We consider observables $\hat{A}$ [(a) and (b)] and $\hat{B}$ [(c) and (d)] at integrable [(a) and (c), $\lambda = 0$] and nonintegrable [(b) and (d), $\lambda = 1$] points of Hamiltonian (2.1) with $\Delta = 0.55$. We consider 200 energy eigenstates at the center of the spectrum. The insets in (a) and (c) show the probability distributions $P(\ln|O_{\alpha\beta}|)$, along with Gaussian distributions (continuous lines) with the same mean and variance. The continuous lines in the main panels in (a) and (c) are the corresponding log-normal distributions. The continuous lines in panels (b) and (d) are Gaussian distributions with the same mean and variance as the distributions $P(O_{\alpha\beta})$.

have approximately zero mean, they exhibit sharp peaks at the origin. Analyses of the distributions of $\ln|O_{\alpha\beta}|$ (shown in the insets) provide a better insight on the distributions of $O_{\alpha\beta}$. We find that, for our observables, the $\ln|O_{\alpha\beta}|$ distributions have skewed normal-like shapes [insets in Figs. 2.6(a) and 2.6(c)]. Gaussian distributions with the same mean and variance as our numerical results for $\ln|O_{\alpha\beta}|$, shown as continuous lines in the insets, illustrate the Gaussianity and skewness of the $\ln|O_{\alpha\beta}|$ distributions. The corresponding log-normal distributions, shown as continuous lines in the main panels, capture some of the features observed in the distributions of $O_{\alpha\beta}$ but fail to describe them quantitatively. Which distribution fully characterizes our results for $O_{\alpha\beta}$ at integrability remains a question for future studies.

We have also studied the distributions of $A_{\alpha\beta}$ and $B_{\alpha\beta}$ for $E = (E_\alpha + E_\beta)/2 \simeq 0$ and $\omega > 0$,

obtaining qualitatively similar results as those shown in Fig. 2.6 for $E = (E_\alpha + E_\beta)/2 \simeq 0$ and $\omega \simeq 0$. Next, instead of reporting those distributions for $\omega > 0$, we study the ratio

$$\Gamma_O(\omega) = \overline{|O_{\alpha\beta}|^2} / \overline{|O_{\alpha\beta}|}^2, \tag{2.9}$$

where α and β are eigenstates that satisfy $|\bar{E}|/L \leq 0.025$, $\omega = |E_\alpha - E_\beta|$ takes values that vary throughout the entire spectrum, and $\overline{(\dots)}$ denotes a running average of the relevant quantity over eigenstates within a small ω window. If $O_{\alpha\beta}$ has a Gaussian distribution with zero mean, then $\Gamma_O(\omega) = \pi/2$ irrespectively of model parameters and the observable considered.

At the nonintegrable point, Figs. 2.7(b) and 2.7(d) show that both $\Gamma_A(\omega)$ and $\Gamma_B(\omega)$ are almost indistinguishable from $\pi/2$ for $\omega \lesssim 5$. Discrepancies from $\pi/2$ can be seen for $\omega \gtrsim 5$. In this regime, we find in the next section that the variance of the off-diagonal

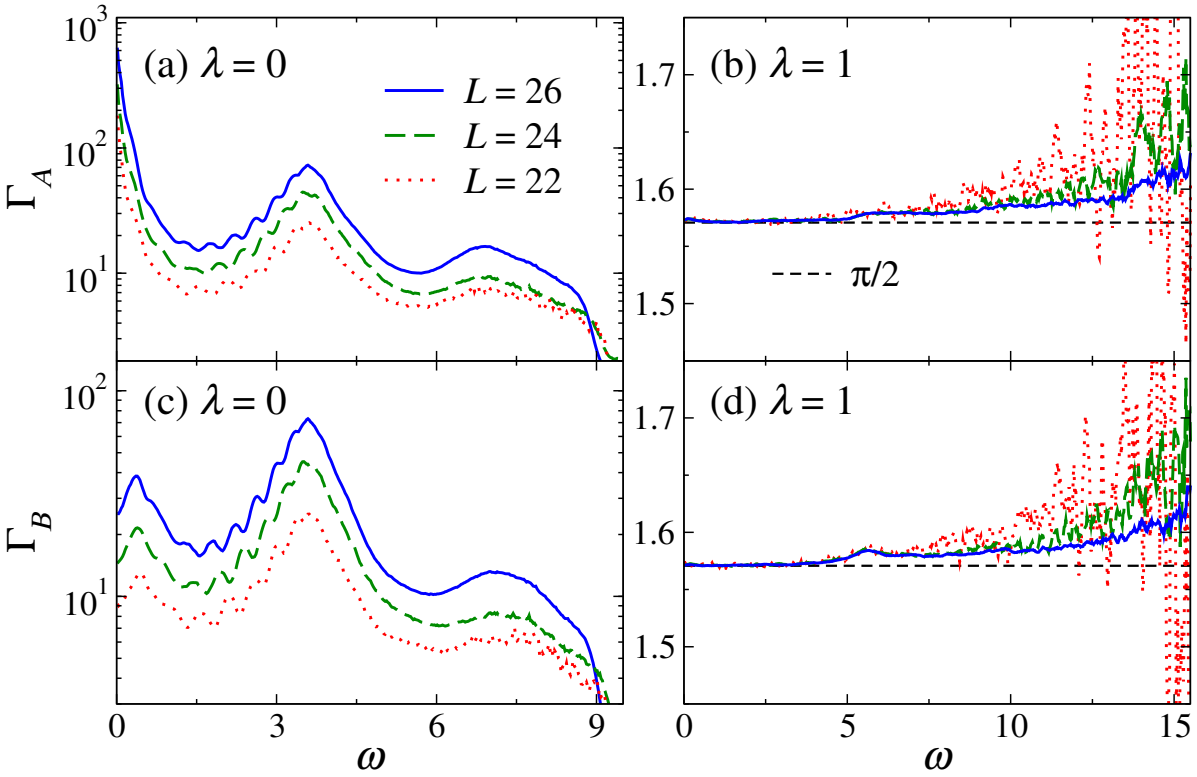

Figure 2.7 | **Gaussianity test for off-diagonal matrix elements.** Γ_O [see Eq. (2.9)] vs ω for observables $\hat{A}$ [(a) and (b)] and $\hat{B}$ [(c) and (d)] at integrable [(a) and (c), $\lambda = 0$] and nonintegrable [(b) and (d), $\lambda = 1$] points ($\Delta = 0.55$) and different system sizes. We compute Γ_O using eigenstates that satisfy $|\bar{E}|/L \leq 0.025$. The averages $\overline{|O_{\alpha\beta}|}$ and $\overline{|O_{\alpha\beta}|^2}$ are calculated with eigenstates in a window $\delta\omega = 0.175$ centered at points in ω separated by $\Delta\omega = 0.025$.

matrix elements decreases rapidly with increasing ω. For $5 \lesssim \omega \lesssim 8$ in Figs. 2.7(b) and 2.7(d), $\Gamma_A(\omega)$ and $\Gamma_B(\omega)$ appear converged to results that could signal a small system-size-independent deviation from the Gaussian distribution prediction. However, finite-size effects are evident for $\omega \gtrsim 8$ (where $\Gamma_A(\omega)$ and $\Gamma_B(\omega)$ decrease with increasing system size) and could also be affecting the regime $5 \lesssim \omega \lesssim 8$. Thus, whether $\Gamma_O(\omega)$ agrees with the Gaussian distribution prediction at high values of ω is something that requires future investigation. However, for $\omega \lesssim 5$, our results are a stringent test of the Gaussianity of the distributions of $O_{\alpha\beta}$ in the nonintegrable case.

In contrast, at the integrable point, Figs. 2.7(a) and 2.7(c) show that $\Gamma_A(\omega)$ and $\Gamma_B(\omega)$ depend on ω, L, and the observable considered. This shows that the distribution of $O_{\alpha\beta}$ is not Gaussian at any ω. A second point to be highlighted from the behavior of $\Gamma_O(\omega)$ at integrability is that, since $\Gamma_O(\omega)$ increases with increasing system size L, $\overline{|O_{\alpha\beta}|^2}$ decreases more slowly with increasing L than $\overline{|O_{\alpha\beta}|}^2$. Since $\overline{|O_{\alpha\beta}|^2}$ is the quantity that enters in fluctuation dissipation relations [2, 29], transport properties [30, 108], and heating rates under periodic driving [1], in what follows we focus on the scaling of $\overline{|O_{\alpha\beta}|^2}$ with increasing system size, and on the smooth function that characterizes the dependence of $\overline{|O_{\alpha\beta}|^2}$ on ω.

2.5.2 Variance

In Fig. 2.8, we show normalized distributions (color coded) of $\log_{10}|A_{\alpha\beta}|^2$ and $\log_{10}|B_{\alpha\beta}|^2$ vs ω at integrable and nonintegrable points of Hamiltonian (2.1), for eigenstates that satisfy $|\bar{E}|/L \leq 0.025$. These results were obtained for $\Delta = 0.55$ in chains with $L = 26$. While for all values of ω the distributions are clearly different between the integrable and nonintegrable cases in that the former have a much broader support, neither of them have an increasing fraction of matrix elements that vanish with increasing system size as in quadratic models [29]. This means that one can define a meaningful average $\overline{|O_{\alpha\beta}|^2}$ for each value of ω, which, given that $\overline{O_{\alpha\beta}} \simeq 0$, is also the variance of $O_{\alpha\beta}$. In Fig. 2.8, we also plot the variances of $O_{\alpha\beta}$. Again, while they are quantitatively different between the integrable and nonintegrable cases, the overall behavior is qualitatively similar. They exhibit a slow decay at intermediate values of ω ($0.5 \lesssim \omega \lesssim 4$) and a fast decay at larger values of ω.

Next, we study how $\overline{|O_{\alpha\beta}|^2}$ scales with increasing the system size (and, hence, with increasing the dimension D of the Hilbert space). In the quantum chaotic case, we expect the scaling to be the one prescribed by the ETH. However, as we did when studying the fluctuations of the diagonal matrix elements in Sec. 2.4, we need to update the ETH

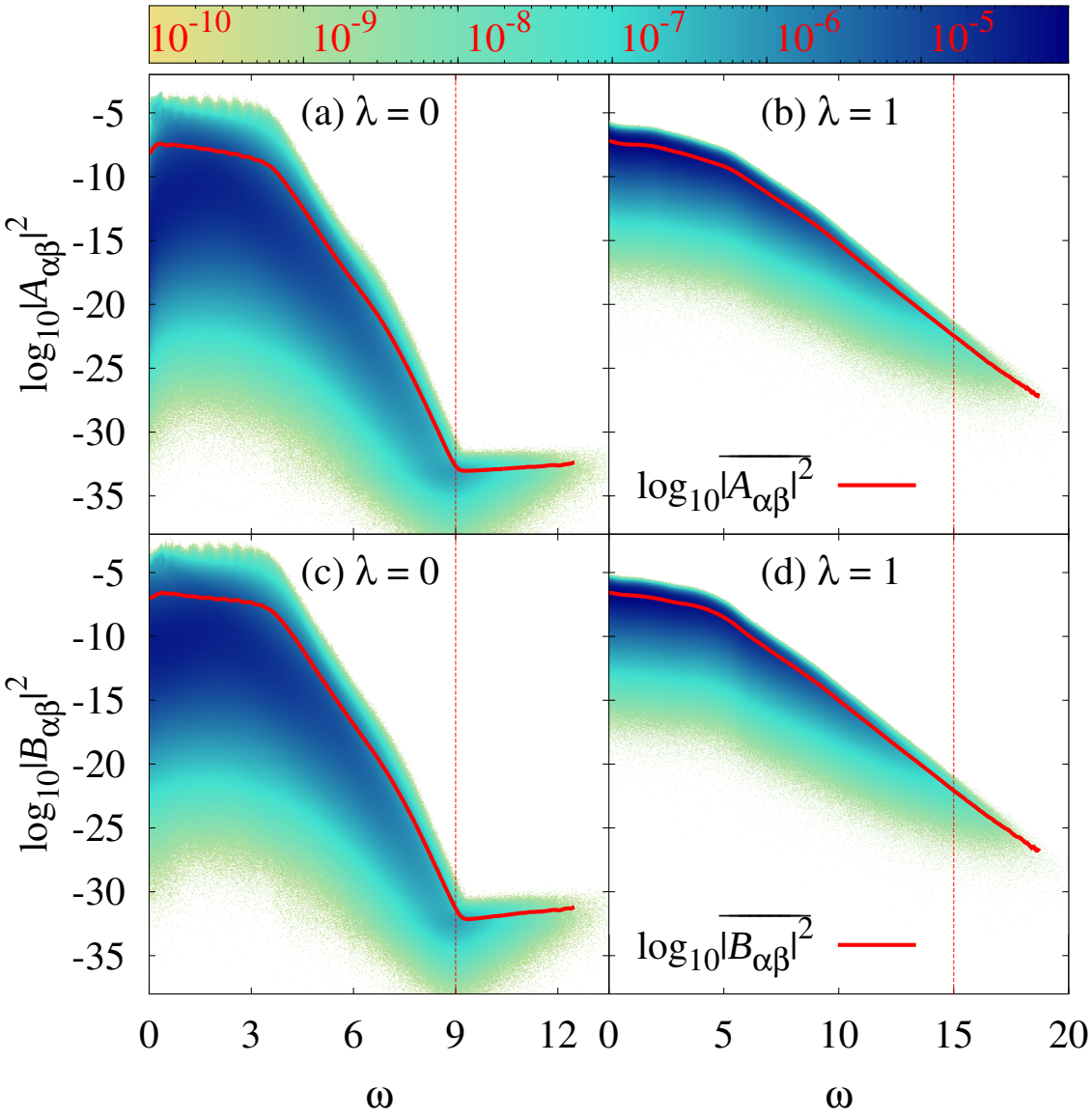

Figure 2.8 | **Normalized 2D histograms of** $\log_{10}|O_{\alpha\beta}|^2$ **vs** ω**.** We consider observables $\hat{A}$ [(a) and (b)] and $\hat{B}$ [(c) and (d)] at integrable [(a) and (c), $\lambda = 0$] and nonintegrable [(b) and (d), $\lambda = 1$] points of Hamiltonian (2.1) with $\Delta = 0.55$. We consider eigenstates that satisfy $|\bar{E}|/L \leq 0.025$. The solid (red) lines are averages calculated using all the matrix elements in windows of widths $\delta\omega = 0.175$ centered at points separated by $\Delta\omega = 0.025$. The red dashed lines show the values of ω up to which results for $|O_{\alpha\beta}|^2$ are included in the scaling analyses of Fig. 2.9.

ansatz to account for the fact that our translationally invariant operators $\hat{A}$ and $\hat{B}$ have a Hilbert-Schmidt norm that scales as $1/\sqrt{L}$. The ETH ansatz for the off-diagonal matrix

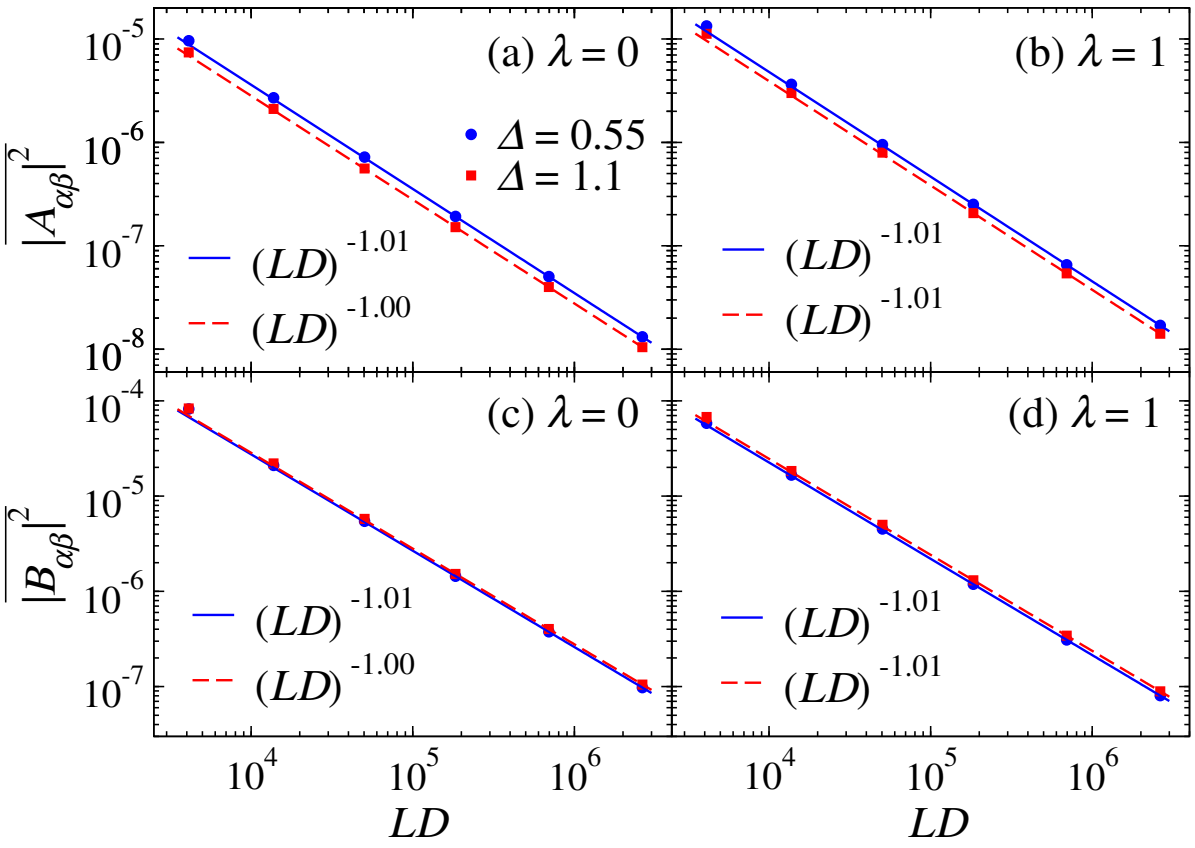

Figure 2.9 | **Scaling of the variance of off-diagonal matrix elements.** We plot $\overline{|A_{\alpha\beta}|^2}$ [(a) and (b)] and $\overline{|B_{\alpha\beta}|^2}$ [(c) and (d)] vs LD at integrable [(a) and (c), $\lambda = 0$] and nonintegrable [(b) and (d), $\lambda = 1$] points ($\Delta = 0.55$ and 1.1) of Hamiltonian (2.1). The straight lines show power-law fits to the results for $L = 22$ through $L = 26$. The average over $|O_{\alpha\beta}|^2$ for different system sizes was calculated using eigenstates that satisfy $|\bar{E}|/L \leq 0.025$. For the integrable cases we used eigenstates with $\omega < 9$ [see the vertical dashed lines in Figs. 2.8(a) and 2.8(c)], while for the nonintegrable ones we used eigenstates with $\omega < 15$ [see the vertical dashed lines in Figs. 2.8(b) and 2.8(d)]. These ranges of ω were the ones populated with matrix elements for the system sizes considered.

elements of $\hat{A}$ and $\hat{B}$ has the form

$$O_{\alpha\beta} = \frac{e^{-S(\bar{E})/2}}{\sqrt{L}} f_O(\bar{E}, \omega) R_{\alpha\beta}, \tag{2.10}$$

where $\bar{E} \equiv (E_\alpha + E_\beta)/2$, $\omega = E_\alpha - E_\beta$, and $S(\bar{E})$ is the thermodynamic entropy at energy $\bar{E}$. Since we are focusing on the regime $\bar{E}/L \simeq 0$, in which $S(\bar{E}) \simeq \ln(D)$, we expect $\overline{|O_{\alpha\beta}|^2} \propto (LD)^{-1}$, where D is the dimension of the symmetry sector studied. Figures 2.9(b) and 2.9(d) show that this is indeed the way $\overline{|O_{\alpha\beta}|^2}$ scales with increasing

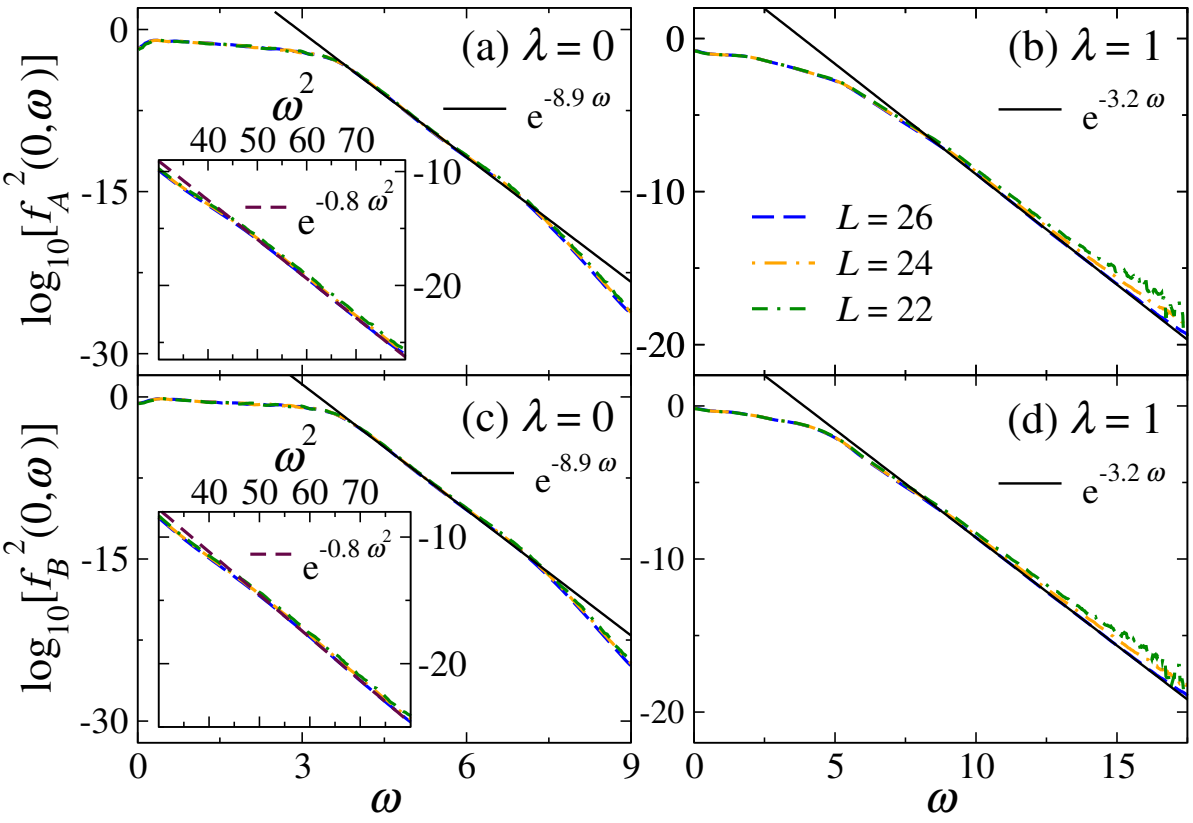

Figure 2.10 | **Smooth functions $|f_O(\bar{E} \simeq 0, \omega)|^2$ vs ω.** See Eq. (2.11). We use observables A [(a) and (b)] and B [(c) and (d)] vs ω at integrable [(a) and (c), $\lambda = 0$] and nonintegrable [(b) and (d), $\lambda = 1$] points ($\Delta = 0.55$) for different system sizes L. The straight continuous lines are exponential fits $\propto \exp(-a\omega)$ to $|f_O(\bar{E} \simeq 0, \omega)|^2$ for $L = 26$. The insets in (a) and (c) show $|f_O(\bar{E} \simeq 0, \omega)|^2$ vs ω^2, at high ω, for different system sizes L. The straight dashed lines are Gaussian fits $\propto \exp(-b\omega^2)$ to $|f_O(\bar{E} \simeq 0, \omega)|^2$ for $L = 26$.

system size. More remarkably, as shown in Figs. 2.9(a) and 2.9(c), the same is equally true for the integrable case as conjectured in Ref. [1].

Armed with this knowledge, we can now extract the smooth function $|f_O(\bar{E} \simeq 0, \omega)|^2$, which is independent of system size for nonvanishing values of ω [2], that characterizes $\overline{|O_{\alpha\beta}|^2}$. That function, calculated as

$$|f_O(\bar{E} \simeq 0, \omega)|^2 = LD\,\overline{|O_{\alpha\beta}|^2}\,, \tag{2.11}$$

is plotted in Fig. 2.10 for our two observables of interest, at integrable [Figs. 2.10(a) and 2.10(c)] and nonintegrable [Figs. 2.10(b) and 2.10(d)] points, for the three largest system sizes studied. As advanced, we obtain nearly perfect data collapse for different

system sizes. At the nonintegrable point, $|f_O(\bar{E} \simeq 0, \omega)|^2$ exhibits finite-size effects for $\omega \gtrsim 10$. This is the result of running out of spectrum in our finite-system calculations. However, Figs 2.10(b) and 2.10(d) show that, with increasing system size, the results for different values of L agree over a larger range of values of ω. Overall, the results in Fig. 2.10 strongly suggest that the function $|f_O(\bar{E}, \omega)|^2$ is a well defined smooth function of $\bar{E}$ and ω (independent of system size for nonvanishing values of ω) both in interacting integrable and nonintegrable systems.

Finally, we would like to discuss the decay of $|f_O(\bar{E} \simeq 0, \omega)|^2$ for large values of ω, after the slow decay mentioned before. (The behavior of $|f_O(\bar{E} \simeq 0, \omega)|^2$ for very small values of ω is of much interest, but it is also more challenging to address computationally [2]. It will not be discussed here.) As shown in Fig. 2.10, at both the integrable and nonintegrable points, $|f_A(\bar{E} \simeq 0, \omega)|^2$ and $|f_B(\bar{E} \simeq 0, \omega)|^2$ can be well described by exponentials after the initial slow decay. This is well known for nonintegrable systems [2], and we find that it also occurs for integrable ones. However, at the integrable point we find yet another regime beyond the exponential one. As shown in the insets in Figs. 2.10(a) and 2.10(c), we find that the final decay of $|f_A(\bar{E} \simeq 0, \omega)|^2$ and $|f_B(\bar{E} \simeq 0, \omega)|^2$ to zero (within machine precision) is nearly perfectly Gaussian. Whether a Gaussian decay occurs at nonintegrable points for larger values of ω than those accessible to us via full exact diagonalization remains an open question. Upon replotting the $|f_O(\bar{E} \simeq 0, \omega)|^2$ data reported in Ref. [40] for the Holstein polaron model, which was shown to be a quantum chaotic model, we found that it can be well described by a Gaussian decay (without any exponential part). This suggests that Gaussian decays of $|f_O(\bar{E}, \omega)|^2$ with ω are not unique to integrable models.

2.6 Summary

We studied the bipartite von Neumann entanglement entropy and matrix elements of local operators in highly excited eigenstates of interacting integrable (the spin-1/2 XXZ chain) and nonintegrable models.

For the average entanglement entropy over all eigenstates in the zero magnetization sector, we found that the leading term is extensive at interacting integrable points with a coefficient of the volume-law that is smaller (for nonvanishing ratios L_A/L) than the universal $\ln 2$ coefficient in quantum chaotic models. Finite-size scaling analyses suggested that the coefficient at $L_\mathrm{A}/L = 1/2$, and for arbitrary ratios L_A/L (not reported), is (almost) independent of the XXZ chain anisotropy parameter Δ, and that it is very

close or equal to that of translationally invariant free fermionic Hamiltonians. Since the average entanglement entropy over all eigenstates is dominated by eigenstates at "infinite temperature", the presence, or lack thereof, of interactions (and their values) at integrability may play no role in the leading extensive term. What may be essential is that the system is integrable so that it has an underlying quasiparticle description. Hence, we find it plausible that all translationally invariant (two-state per site) integrable models (noninteracting and interacting) have the same average entanglement entropy for any given ratio $L_{\rm A}/L$. If this is the case, then one could think of two universality classes for the average entanglement entropy of all "q-bit" based physical Hamiltonians, (translationally invariant) free fermions characterizing integrable models and random matrices characterizing nonintegrable ones.

For the diagonal matrix elements of observables at the center of the spectrum and at interacting integrable points, we showed evidence that the support does not vanish with increasing system size and that the average eigenstate to eigenstate fluctuation vanishes as a power law in system size. At nonintegrable points, however, both the support and the average eigenstate to eigenstate fluctuation vanish exponentially with increasing system size. For the off-diagonal matrix elements with $\bar{E} = (E_\alpha + E_\beta)/2$ at the center of the spectrum, we showed that at interacting integrable points they follow a distribution that is close to (but not quite) log-normal, and that their variance is a well-defined function of $\omega = E_\alpha - E_\beta$ whose magnitude scales as $1/D$, where D is the Hilbert space dimension. The latter is a known property of the off-diagonal matrix elements of observables in nonintegrable models, which, however, exhibit a Gaussian distribution. We also studied the smooth function $|f_O(\bar{E} \simeq 0, \omega)|^2$ that characterizes the variance and contrasted its behavior at interacting integrable and nonintegrable points. It was recently argued that this function can be measured in experiments with periodically driven systems, both nonintegrable and interacting integrable ones, by studying how heating rates change when changing the frequency of the drive [1]. An interesting open question is whether the Bethe ansatz can be used to analytically learn about the smooth function $|f_O(\bar{E}, \omega)|^2$ in interacting integrable systems. This would open a path for the analytic understanding of the effect of interactions in the matrix elements of observables in many-body quantum systems.

2.7 Acknowledgements

My contribution to the work presented here was supported by the National Science Foundation under Grant No. PHY-1707482. I carried out the computations on the Roar supercomputer of the Institute for Computational and Data Sciences (ICDS) at Penn State.

Chapter 3
Eigenstate Thermalization in a Locally Perturbed Integrable System

3.1 Introduction

How do statistical ensembles and thermal behavior emerge from the fundamental unitary dynamics of isolated quantum systems? This question, first posed in the earliest days of quantum mechanics [109–111], is still at the forefront of modern research in quantum statistical mechanics [2, 49, 50]. The current interest in this foundational topic can be attributed to advances in ultracold atomic experiments where many-body systems can be time propagated coherently over unprecedented time scales [3–5]. In particular, seminal experiments have demonstrated that integrability inhibits thermalization [6], and that integrability breaking perturbations can be used to controllably bring a system to thermal equilibrium [9]. The latter experimental results are consistent with the expectation that generic isolated quantum systems thermalize to a microcanonical distribution consistent with their energy density. The accepted mechanism for this is eigenstate thermalization, as prescribed by the eigenstate thermalization hypothesis (ETH) (1.14).

Integrable systems, which possess extensive sets of nontrivial conserved quantities, do not follow the ETH. The diagonal matrix elements of observables exhibit eigenstate to eigenstate fluctuations that do not vanish in the thermodynamic limit [13, 26–28, 30, 31, 45, 56], while their variance vanishes as a power law in the system size [45, 66–68]. Because of this, in general, integrable systems do not thermalize [112]. They do equilibrate and, after equilibration, they are described by generalized Gibbs ensembles (GGEs) [43, 51, 55, 56].

For the off-diagonal matrix elements of observables in interacting integrable systems, it was recently shown that their variance is a well-defined (exponentially small in the system size) function of the average energy and the energy difference of the eigenstates involved [1, 45], like in systems that satisfy the ETH.

Integrability is believed to be unstable to perturbations [2]. Surprisingly, it has been shown that even a single magnetic impurity perturbation at the center of the integrable spin-1/2 XXZ chain is enough to induce level repulsion and random matrix statistics in the spectrum [47, 113–118]. Recently, a study of both linear response and steady-state transport showed that this model displays ballistic spin transport [47], challenging our expectation that quantum chaotic systems (those exhibiting random matrix statistics in the spectrum) should exhibit diffusive transport. In this chapter we show that the matrix elements of observables in such a model are fully consistent with the ETH. Unique to breaking integrability with local perturbations, we argue that statistical mechanics and transport properties of the unperturbed integrable model can end up embedded in properties of the eigenstates of the perturbed (quantum chaotic) one.

3.2 Model and Observables

The Hamiltonian of the spin-1/2 XXZ (in short, the XXZ) chain can be written as (we set $\hbar = 1$):

$$\hat{H}_{\mathrm{XXZ}} = \sum_{i=1}^{N-1} \left(\hat{\sigma}_i^x \hat{\sigma}_{i+1}^x + \hat{\sigma}_i^y \hat{\sigma}_{i+1}^y + \Delta\, \hat{\sigma}_i^z \hat{\sigma}_{i+1}^z \right), \tag{3.1}$$

where $\hat{\sigma}_i^\nu$, $\nu = x, y, z$, correspond to Pauli matrices in the ν direction at site i in a chain with N (taken to be even) sites and open boundary conditions. In Eq. (3.1), Δ is the anisotropy parameter. We focus on $\Delta = 0.55$, for which spin transport is ballistic, but also show results for $\Delta = 1.1$, for which spin transport is diffusive [119].

The XXZ chain is a quintessential interacting integrable model [104, 120]. We study properties of its eigenstates along with those of eigenstates of the nonintegrable model obtained by perturbing it with a magnetic impurity about the center of the chain. This local perturbation produces an energy spectrum with a Wigner-Dyson distribution of nearest-neighbor level spacings [47, 113–115, 117, 118]. The single-impurity Hamiltonian has the form

$$\hat{H}_{\mathrm{SI}} = \hat{H}_{\mathrm{XXZ}} + h\, \hat{\sigma}_{N/2}^z, \tag{3.2}$$

where h is the strength of the magnetic impurity. We henceforth set $h = 1$ so that all energy scales in our perturbed Hamiltonian are $\mathcal{O}(1)$.

Both Hamiltonians of interest in this chapter, Eqs. (3.1) and (3.2), commute with the total magnetization operator in the z direction, $[\hat{H}_{\mathrm{XXZ}}, \sum_i \hat{\sigma}_i^z] = [\hat{H}_{\mathrm{SI}}, \sum_i \hat{\sigma}_i^z] = 0$, so they are $U(1)$ symmetric. We focus on the zero magnetization sector, $\sum_i \langle \hat{\sigma}_i^z \rangle = 0$, which is the largest sector. Reflection symmetry is present in $\hat{H}_{\mathrm{XXZ}}$. We explicitly break it by adding a very weak magnetic field at site $i = 1$, $h_1 = 10^{-1}$ (like open boundary conditions, this perturbation does not break integrability [113]). We use state of the art full exact diagonalization, and study chains with up to $N = 20$ sites, for which the Hilbert space dimension $\mathcal{D} = N!/[(N/2)!]^2 = 184\,756$.

3.3 Diagonal ETH

Let us first study the diagonal matrix elements of two related local observables. We choose the local kinetic energy at site $i = N/4$ (far away from the boundary and the impurity),

$$\hat{K} \coloneqq \hat{K}_{\frac{N}{4},\frac{N}{4}+1} = \left(\hat{\sigma}^x_{\frac{N}{4}} \hat{\sigma}^x_{\frac{N}{4}+1} + \hat{\sigma}^y_{\frac{N}{4}} \hat{\sigma}^y_{\frac{N}{4}+1} \right), \tag{3.3}$$

and the total kinetic energy per site, the average local kinetic energy, defined as

$$\hat{T} \coloneqq \frac{1}{N} \sum_{i=1}^{N-1} \left(\hat{\sigma}^x_i \hat{\sigma}^x_{i+1} + \hat{\sigma}^y_i \hat{\sigma}^y_{i+1} \right). \tag{3.4}$$

The contrast between the two shows the effect of averaging in nontranslation invariant systems. Qualitatively similar results were obtained for other local observables.

In Fig. 3.1, we show the diagonal matrix elements of $\hat{K}$ and $\hat{T}$ in the eigenstates of the Hamiltonians in Eqs. (3.1) and (3.2). The results are plotted as functions of the energy density defined as $\epsilon_n \coloneqq E_n - E_{\mathrm{min}}/E_{\mathrm{max}} - E_{\mathrm{min}}$, where E_n is the nth energy eigenvalue, and E_{min} (E_{max}) is the lowest (highest) energy eigenvalue. Despite the quantitative differences in the behavior of the two observables in each model (at each energy, the spread of T_{nn} is smaller than that of K_{nn}), they both exhibit a qualitatively similar behavior depending on whether the model is integrable ($\hat{H}_{\mathrm{XXZ}}$) or nonintegrable ($\hat{H}_{\mathrm{SI}}$). In the integrable model, the spread of T_{nn} and K_{nn} at each energy does not change with changing system size (the system does not satisfy the ETH), while in the nonintegrable model it decreases exponentially fast with increasing N [away from the edges of the spectrum, see insets in Figs. 3.1(b) and 3.1(d) for a variance indicator] suggesting that T_{nn} and K_{nn} satisfy the ETH [115, 116].

Since the single impurity is a subextensive local perturbation to the XXZ chain, it does

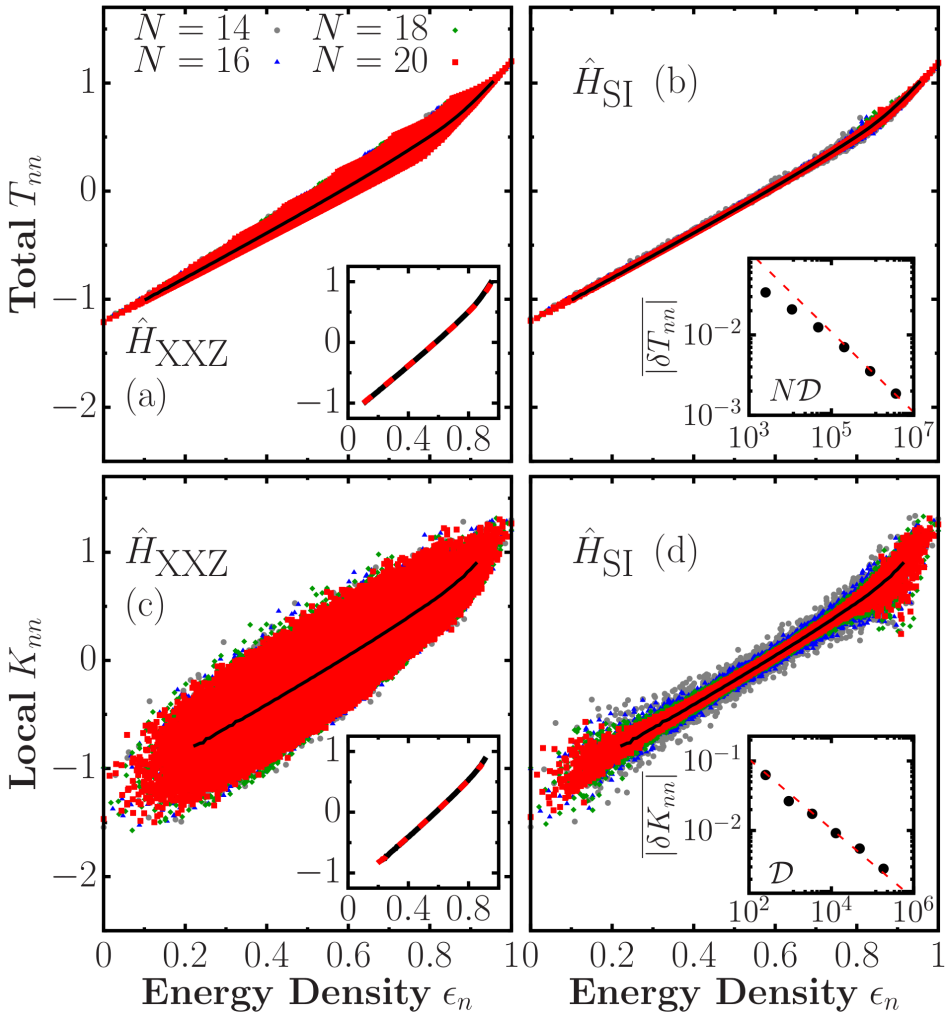

Figure 3.1 | **Diagonal matrix elements and equivalence of microcanonical predictions.** Diagonal matrix elements of operators $\hat{T}$ [(a), (b)] and $\hat{K}$ [(c), (d)] in the eigenstates of $\hat{H}_{\rm XXZ}$ [(a), (c)] and $\hat{H}_{\rm SI}$ [(b), (d)] ($\Delta = 0.55$). The black lines show microcanonical averages (within windows with $\delta\epsilon_n = 0.008$) in $\hat{H}_{\rm XXZ}$ for the largest chain ($N = 20$). The insets in (a) and (c) show the equivalence of the microcanonical predictions in both models for each observable, while the insets in (b) and (d) show the $(N\mathcal{D})^{-1/2}$ and $\mathcal{D}^{-1/2}$ scalings, respectively, of $\overline{|\delta O_{nn}|} \coloneqq \overline{|O_{nn} - O_{n+1n+1}|}$ (the dashed lines are $\propto x^{-1/2}$), where we average over the central 20% of the eigenstates in chains with $N = 10, 12, \ldots, 20$.

not affect the microcanonical predictions (away from the edges of the spectrum) for local observables (away from the impurity) in sufficiently large system sizes. This is confirmed in the insets in Figs. 3.1(a) and 3.1(c). Hence, a remarkable consequence of the single impurity producing eigenstate thermalization (something that is achieved via mixing nearby unperturbed energy eigenstates) is that the smooth functions T_{nn} and

K_{nn} are nothing but the microcanonical ensemble predictions for the integrable model. Another interesting consequence of it is that if one evolves highly excited eigenstates of $\hat{H}_{\rm SI}$ under the integrable dynamics generated by $\hat{H}_{\rm XXZ}$, thermalization will occur at long times (as in the limit of vanishingly small but extensive integrability breaking perturbations [112, 121]).

3.4 Off-diagonal ETH

Next we study the off-diagonal matrix elements of the total kinetic energy per site $\hat{T}$ [Eq. (3.4)], and of the spin current operator per site $\hat{J}$,

$$\hat{J} := \frac{1}{N}\sum_{i=1}^{N-1}\left(\hat{\sigma}_i^x\hat{\sigma}_{i+1}^y - \hat{\sigma}_i^y\hat{\sigma}_{i+1}^x\right). \tag{3.5}$$

Since $\hat{T}$ and $\hat{J}$ have Hilbert-Schmidt norms that scale as $1/\sqrt{N}$, the off-diagonal part of the ETH needs to be modified to read [41, 45]

$$O_{nm} = \frac{e^{-S(\bar{E})/2}}{\sqrt{N}} f_O(\bar{E},\omega) R_{nm}. \tag{3.6}$$

We focus on the "infinite-temperature" regime, in which $\bar{E} \approx 0$ and $S(\bar{E}) \approx \ln \mathcal{D}$.
In Figs. 3.2(a) and 3.2(b), we show the off-diagonal matrix elements $|T_{nm}|^2$ in the XXZ and single-impurity models, respectively. As expected, their overall dispersion is larger in the former (integrable) model than the latter (nonintegrable) one. For both models, Figs. 3.2(a) and 3.2(b) show that the coarse-grained average $\overline{|T_{nm}|^2}$ (which corresponds to the variance of the off-diagonal matrix elements as $\overline{T_{nm}} = 0$) is a smooth function of ω [45]. In Ref. [45], it was shown that the variance of the off-diagonal matrix elements of observables like the ones of interest here satisfies $\overline{|O_{nm}|^2} \propto (N\mathcal{D})^{-1}$ both for integrable interacting and nonintegrable models. Figures 3.2(c) and 3.2(d) for $\overline{|T_{nm}|^2}$, and Figs. 3.2(e) and 3.2(f) for $\overline{|J_{nm}|^2}$, show that such a scaling is satisfied by our observables in the XXZ and single-impurity models.
Figures 3.2(c) and 3.2(d) [Figs. 3.2(e) and 3.2(f)] also show that the variances $\overline{|T_{nm}|^2}$ ($\overline{|J_{nm}|^2}$) are very similar in the two models (the differences are consistent within present finite-size effects). For $\overline{|J_{nm}|^2}$, see insets in Figs. 3.2(e) and 3.2(f), the similarity extends to features that occur at low frequencies (see also Fig. 3.4). This opens the question of whether there is any difference between the off-diagonal matrix elements of observables

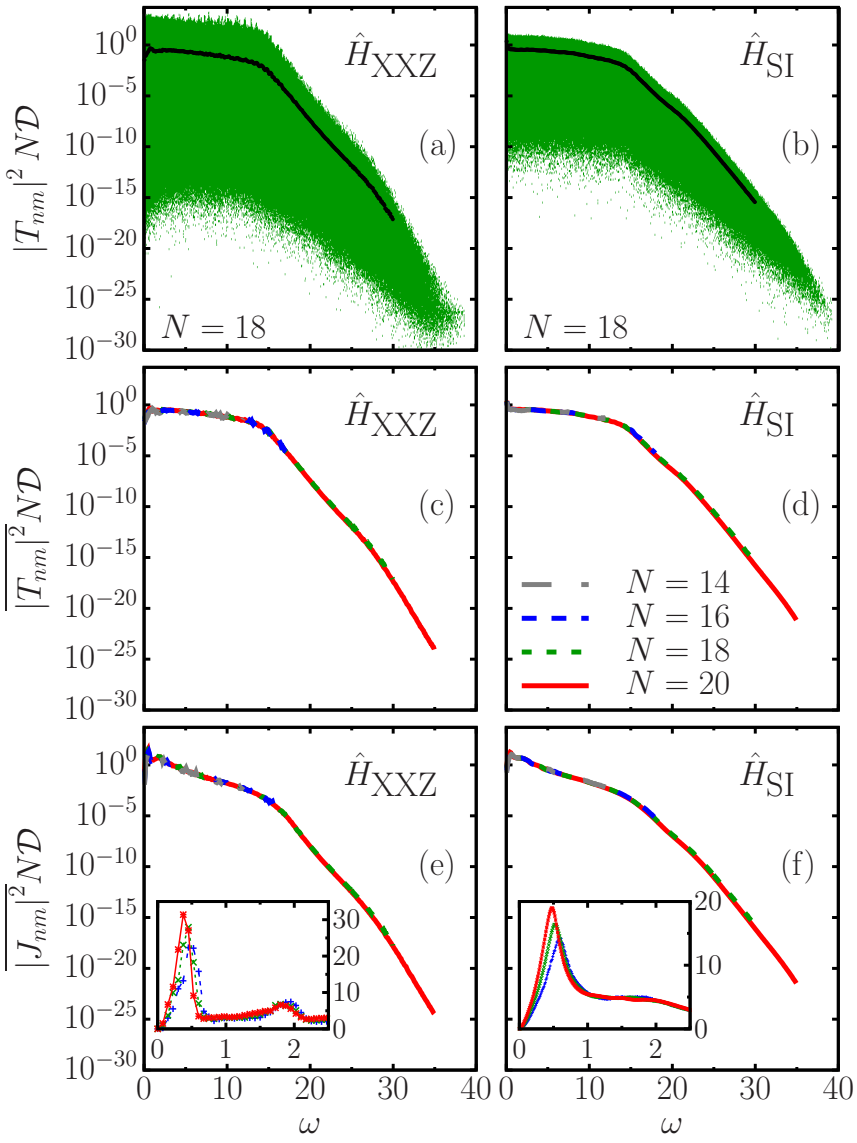

Figure 3.2 | **Off-diagonal matrix elements and their scaled variances.** [(a), (b)] Off-diagonal matrix elements of $\hat{T}$, and the corresponding coarse-grained average [continuous (black) line], plotted vs ω for chains with $N = 18$. [(c), (d)] Coarse-grained averages of T_{nm}, including the ones reported in (a) and (b), for different chain sizes. [(e), (f)] Coarse-grained averages of J_{nm} for different chain sizes (the insets show results at low ω, see also Fig. 3.4). The left panels [(a), (c), and (e)] show results for $\hat{H}_{\rm XXZ}$, while the right ones [(b), (d), and (f)] show results for $\hat{H}_{\rm SI}$ ($\Delta = 0.55$). The matrix elements were computed within a small window of energy around $\bar{E} \approx 0$ (center of the spectrum) of width 0.05ε (0.075ε for the insets), where $\varepsilon := E_{\rm max} - E_{\rm min}$. The coarse-grained averages were computed using a window $\delta\omega = 0.1$ [$\delta\omega = 0.075$ and $\delta\omega = 0.01$ for the insets in (e) and (f), respectively].

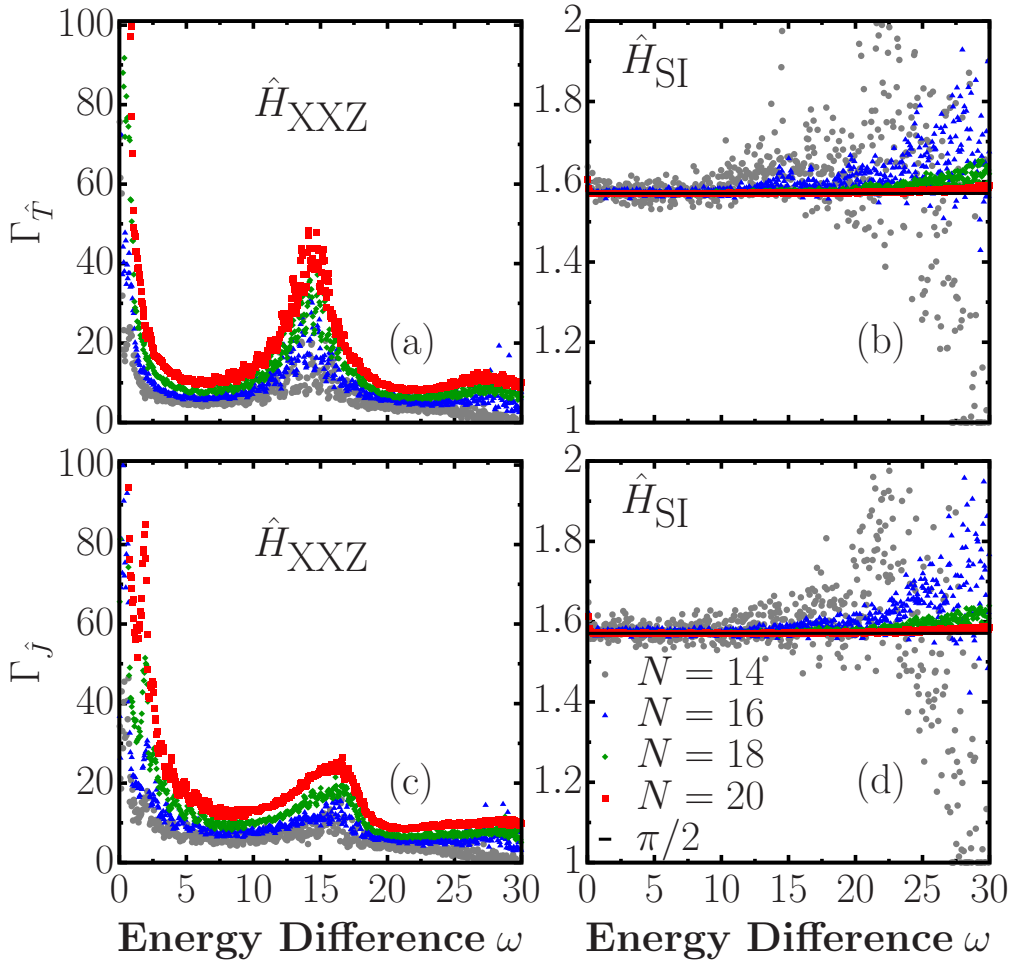

Figure 3.3 | **Gaussianity test of off-diagonal matrix elements.** $\Gamma_{\hat{O}}(\omega)$, see Eq. (3.7), for the total kinetic energy per site [(a), (b)] and for the current operator [(c), (d)], in the XXZ [(a), (c)] and single-impurity [(b), (d)] models ($\Delta = 0.55$). The horizontal line in (b) and (d) marks $\pi/2$. The matrix elements were computed using the same energy window as in Fig. 3.2, while the coarse-graining parameter is $\delta\omega = 0.05$.

in both models.

We find that the off-diagonal matrix elements of observables are normally distributed in the single-impurity model (qualitatively similar results have been obtained in other nonintegrable models [35, 37, 45]), while they are close to log-normally distributed in the XXZ chain [45]. To test the normality of the distribution in the single-impurity model for different values of ω, and to contrast it to the results for the XXZ chain, we compute [45]

$$\Gamma_{\hat{O}}(\omega) := \overline{|O_{nm}|^2}/\overline{|O_{nm}|}^2. \tag{3.7}$$

$\Gamma_{\hat{O}} = \pi/2$ for normally distributed matrix elements.

In Fig. 3.3, we show results for $\Gamma_{\hat{T}}(\omega)$ [Figs. 3.3(a) and 3.3(b)] and $\Gamma_{\hat{J}}(\omega)$ [Figs. 3.3(c) and 3.3(d)] in the XXZ [Figs. 3.3(a) and 3.3(c)] and single-impurity [Figs. 3.3(b) and 3.3(d)] models. For all values of ω shown in Figs. 3.3(b) and 3.3(d) for the single-impurity model, $\Gamma_{\hat{T}}(\omega)$ and $\Gamma_{\hat{J}}(\omega)$, respectively, approach $\pi/2$ as N increases, i.e., T_{nm} and J_{nm} are well described by a normal distribution. On the other hand, in Figs. 3.3(a) and 3.3(c) for the XXZ model, $\Gamma_{\hat{T}}(\omega)$ and $\Gamma_{\hat{J}}(\omega)$, respectively, depend on the system size, i.e., T_{nm} and J_{nm} are not normally distributed.

The results discussed so far for the matrix elements of local operators in the single-impurity model show that they are fully consistent with the ETH. The fact that the off-diagonal matrix elements are normally distributed (the variance sets all central moments) means that one can define a meaningful $f_O(\bar{E},\omega)$, while this is not the case for the XXZ chain. The question we address next is related to the ballistic spin transport in the single-impurity model [47], which is in stark contrast to the usual diffusive transport found in nonintegrable models.

3.5 Ballistic Transport

Within linear response, the real part of the conductivity reads ($k_B = 1$) [119, 122–125]

$$\mathrm{Re}[\sigma_N(\omega)] = \pi D_N \delta(\omega) + \frac{\pi}{N}\left(\frac{1-e^{-\beta\omega}}{\omega}\right)\sum_{\epsilon_n\neq\epsilon_m} p_n |J_{nm}|^2 \delta(\epsilon_m - \epsilon_n - \omega), \tag{3.8}$$

where D_N is known as the Drude weight, β is the inverse temperature, $p_n = e^{-\beta E_n}/Z$ is the Boltzmann weight of eigenstate $|n\rangle$, and Z is the partition function. J_{nm} are the matrix elements of the spin current operator. In integrable systems with open boundary conditions (e.g., our XXZ chain), D_N can be proved to be identically zero no matter the nature of the spin transport [125]. When transport is ballistic, a peak (or peaks) appear in $\mathrm{Re}[\sigma_N(\omega)]$ at a nonzero frequency (frequencies) proportional to $1/N$. When $N \to \infty$, the peak (peaks) move toward $\omega \to 0$ resulting in a peak in $\mathrm{Re}[\sigma_N(\omega = 0)]$ that signals ballistic transport [125]. Exactly the same was shown to occur in our single impurity model in Ref. [47]. Therefore, in our integrable and nonintegrable models ballistic transport emerges because of the $\omega \to 0$ behavior of the off-diagonal matrix elements of the current operator.

In Fig. 3.4(a), we show the scaled variances of the matrix elements of $\hat{J}$ in XXZ chains with $N = 16$, 18, and 20 as functions of $N\omega$ for $\Delta = 0.55$. A large peak can be seen at a frequency that scales as $1/N$ whose area does not change with increasing N. This is

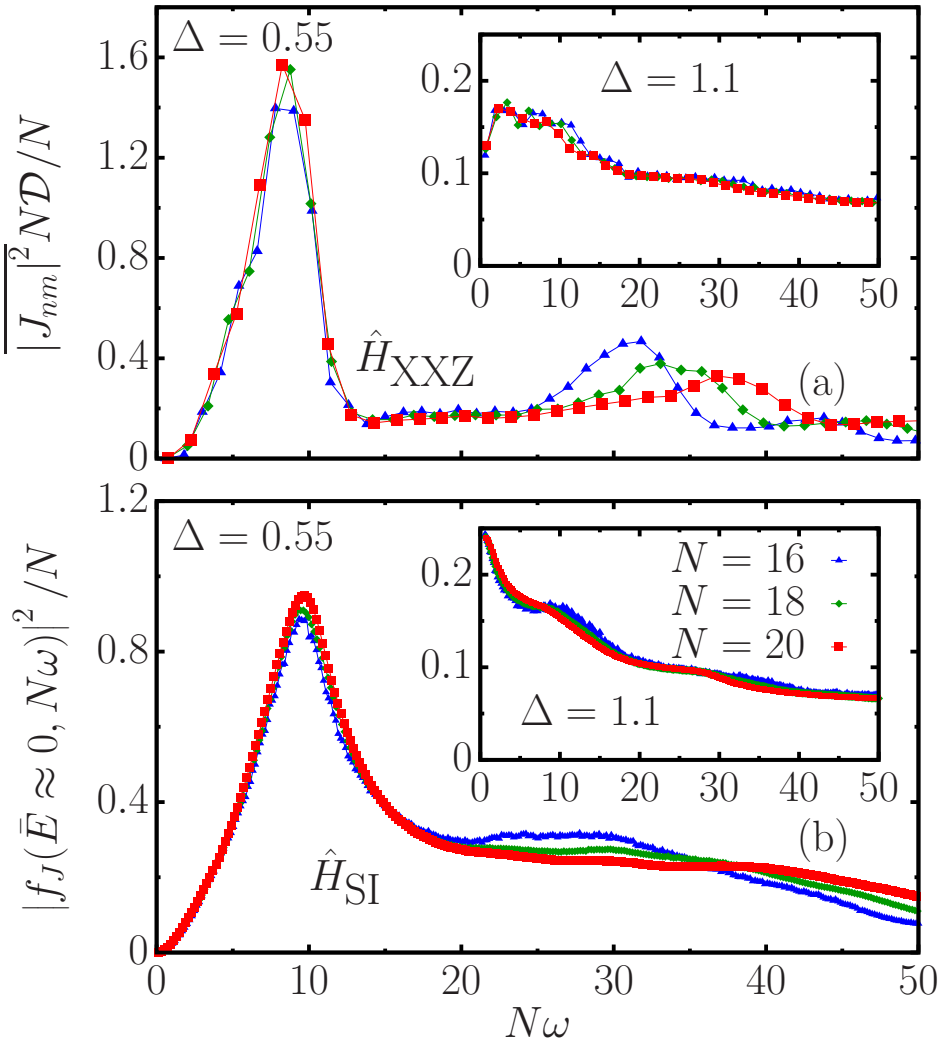

Figure 3.4 | **Ballistic scaling of off-diagonal matrix elements.** Scaled variances of the off-diagonal matrix elements of $\hat{J}$ in the eigenstates of $\hat{H}_{\rm XXZ}$ (a) and $\hat{H}_{\rm SI}$ (b) plotted vs $N\omega$. The main panels (insets) show results for $\Delta = 0.55$ ($\Delta = 1.1$). The matrix elements were computed within a small window of energies around $\bar{E} \approx 0$ of width 0.075ε. For the binned averages, we used $\delta\omega = 0.075$ in (a) and $\delta\omega = 0.01$ in (b).

consistent with the behavior of $\mathrm{Re}[\sigma_N(\omega)]$ [47,125] signaling coherent transport [126]. The position of the smaller (second) peak is nearly N independent [see inset in Fig. 3.2(e)], appearing to mark the onset of the N-independent behavior shown in Fig. 3.2. The variances of the matrix elements of $\hat{J}$ in the (nonintegrable) single-impurity model, which, remarkably, define a novel N-independent ETH function $|f_J(\bar{E} \approx 0, N\omega)|^2/N$ [Fig. 3.4(b)], display the same low-frequency behavior as in the (integrable) XXZ chain. In contrast, as shown in the insets in Fig. 3.4, the scaled variances of the matrix elements

of $\hat{J}$ behave completely differently for $\Delta = 1.1$ (for which spin transport is diffusive). The nature of the spin transport in the absence and presence of the single magnetic defect, for Δ in the easy-plane and easy-axis regimes, is something that can readily be probed in ultracold gases experiments [127].

3.6 Summary

We showed that the ETH is fully fulfilled when breaking integrability with a local perturbation and that, in such setups, it can inherit statistical mechanics and transport properties of the integrable model. Specifically, we showed that the diagonal matrix elements of observables in the perturbed energy eigenstates can follow the microcanonical predictions for the integrable model, and that ballistic transport in the integrable model can result in a novel N-independent ETH function $|f_J(\bar{E} \approx 0, N\omega)|^2/N$ that characterizes the off-diagonal matrix elements of the current operator in the perturbed energy eigenstates at low frequencies.

3.7 Acknowledgements

My contribution to the work presented here was supported by the National Science Foundation under Grant No. PHY-1707482. I carried out preliminary computations on the Roar supercomputer of the Institute for Computational and Data Sciences (ICDS) at Penn State. All the numerical results reported in this chapter were obtained by M. Brenes.

Chapter 4
Eigenstate thermalization for observables that break Hamiltonian symmetries and its counterpart in interacting integrable systems

4.1 Introduction

The emergence of thermalization under unitary dynamics in generic isolated quantum systems has been intensively explored over the past decade [2, 49, 50, 128]. On the experimental side, where high levels of control and isolation in ultracold atomic gases have recently enabled the study of quantum dynamics over long time scales [3–5], both thermalization and the lack thereof have been observed in chaotic [9–12] and (near-)integrable [6–9] quantum systems, respectively. Thermalization in quantum chaotic systems is generally understood in the context of the eigenstate thermalization hypothesis (ETH) [2, 13, 64, 65]. On the integrable side, thermalization is precluded by an extensive set of local conserved quantities, though equilibration in these systems has also been the subject of much interest [43, 56, 61–63]. As the outcomes of quantum dynamics are ultimately determined by properties of matrix elements, the content of the ETH is usually expressed through a matrix-element ansatz for few-body operators (observables) in the eigenstates of chaotic Hamiltonians (1.14) [2, 24].

In quantum integrable systems, the presence of extensive sets of local conserved quantities is manifest in the properties of the matrix elements of observables. It is known that the diagonal matrix elements have both a support that does not vanish in the thermodynamic

limit and average fluctuations that decay as a power law in system size [26–28, 30, 31, 36, 41, 44, 45, 56, 66–68, 129], and thus defy Eq. (1.14). In an interacting integrable system (the spin-1/2 XXZ chain), the off-diagonal matrix elements were recently found to be nearly log-normally distributed [45]. In addition, it was found that the variance is a smooth function of ω (for $\bar{E}$ at the center of the spectrum) that scales as prescribed by the ETH (as a result, it can also be probed experimentally by measuring heating rates in periodically driven systems [1]). The scaling of other moments, of course, is not determined by the scaling of the variance, which means that there is no equivalent of the off-diagonal part of Eq. (1.14) in integrable models.

Using that in interacting integrable systems one can define a smooth scaled variance $V_O(\bar{E}, \omega) \equiv e^{S(\bar{E})}\mathrm{Var}(O_{\alpha\beta})$ [45], recent works have unveiled properties of that function at low values of ω (for $\bar{E}$ at the center of the spectrum of spin-1/2 lattice Hamiltonians, $\bar{E} \approx 0$) [42, 130–132]. Via the computation of the adiabatic gauge potential (AGP) norm, in Ref. [42] it was shown that at exponentially small (in system size) frequencies $V_O(0, \omega)$ vanishes for observables that do not break integrability if added as perturbations to the Hamiltonian, while it scales as in quantum chaotic models for observables that do. Such behaviors were observed in Ref. [131] at frequencies that are polynomially small in the system size. In the latter work it was also shown that observables for which $V_O(0, \omega \to 0)$ scales as in quantum chaotic models do not exhibit eigenstate thermalization at integrability.

By now, several studies have explored properties of the off-diagonal matrix elements of observables in quantum chaotic [2,13,27–30,35,37,39,40,42,45,130–136] and integrable [27–29, 35, 42, 45, 130–136] models. In this chapter we contribute to that existing body of literature by studying the off-diagonal matrix elements (in the energy eigenbasis) of observables that break symmetries of the Hamiltonian. Specifically, we study the off-diagonal matrix elements of observables that break translational symmetry in the eigenstates of translationally invariant Hamiltonians. This means that the off-diagonal matrix elements are nonvanishing between eigenstates from different total quasimomentum sectors. We are not aware of previous studies of the structure of such matrix elements. We compute these matrix elements in the eigenstates of both a quantum-chaotic model and an interacting integrable model, for average energies at the center of the spectrum. In the quantum-chaotic model, we find that the off-diagonal matrix elements exhibit all of the properties prescribed by the ETH. We also find that finite-size effects are larger in matrix elements that connect eigenstates from different total quasimomentum sectors (the overwhelming majority of the matrix elements) than in matrix elements that

connect eigenstates from the same quasimomentum sector. Since, for eigenstates from the same quasimomentum sector, the matrix elements of operators that break translational symmetry are identical to those of the corresponding translationally invariant operator, another way to phrase the latter finding is that non-translationally invariant observables exhibit larger finite-size effects than their translationally invariant counterparts. In the interacting integrable model, we find that the distribution of the matrix elements of the non-translationally invariant observables is skewed log-normal-like with zero mean and a variance that scales as $1/D$ (D is the Hilbert space dimension), as found in Ref. [45] for translationally invariant observables.

Another major goal of this chapter is to understand the low-frequency behavior of the scaled variances. For quantum-chaotic systems, for which the ETH (1.14) is expected to be valid, we refer to the scaled variances as $|f_O(\bar{E},\omega)|^2$. For integrable systems, for which there is no well defined $f_O(\bar{E},\omega)$ function (the scaling of the moments of the distribution of $O_{\alpha\beta}$ is not determined by the scaling of the variance, as mentioned before), we refer to the scaled variances as $V_O(\bar{E},\omega)$. We focus on $\bar{E}$ at the center of the spectrum ($\bar{E} \approx 0$), which is where the overwhelming majority of matrix elements is located in our local Hamiltonians. In the quantum-chaotic model, we find $|f_O(0,\omega)|^2$ to be consistent with random matrix theory, namely, to exhibit a plateau as $\omega \to 0$ (with a diffusive scaling) [2]. In the interacting integrable model, we find the behavior and scaling of $V_O(0,\omega)$ to be rich and observable dependent. For matrix elements that connect energy eigenstates from within the same total quasimomentum sector, we find two possible behaviors as $\omega \to 0$. Either $V_O(0,\omega)$ goes to a nonzero value proportional to L (as in quantum-chaotic models), or it vanishes. For matrix elements that connect energy eigenstates from different quasimomentum sectors, we find that $V_O(0,\omega)$ always goes to a nonzero value proportional to L. Hence, there are observables for which the $\omega \to 0$ behavior of $V_O(0,\omega)$ is qualitatively different between matrix elements that connect energy eigenstates from the same quasimomentum sector and those that connect eigenstates from different quasimomentum sectors. In Sec. 4.4, we discuss the connection between these findings and the results in Refs. [42, 130–132].

The presentation is organized as follows: In Sec. 4.2, we introduce the spin-1/2 chains and the specific observables studied, and discuss details of our numerical calculations. In Sec. 4.3, we report our results for the off-diagonal matrix elements of observables in the quantum-chaotic model, which include a characterization of their distributions and the study of their variances. In Sec. 4.4, we carry out a parallel analysis for the interacting integrable model. In Sec. 4.5, we summarize our results.

4.2 Model

We study the same spin-1/2 chains as in Chapter 2, namely, the XXZ chain with the addition of next-nearest neighbor interactions and periodic boundary conditions. The Hamiltonian reads

$$\begin{aligned}\hat{H} &= \sum_{i=1}^{L}\left[\frac{1}{2}\left(\hat{S}_i^+\hat{S}_{i+1}^- + \text{H.c.}\right) + \Delta\hat{S}_i^z\hat{S}_{i+1}^z\right] \\ &\quad +\lambda\sum_{i=1}^{L}\left[\frac{1}{2}\left(\hat{S}_i^+\hat{S}_{i+2}^- + \text{H.c.}\right) + \frac{1}{2}\hat{S}_i^z\hat{S}_{i+2}^z\right], \end{aligned} \tag{4.1}$$

where $\hat{S}_i^\nu$ are spin-1/2 operators in the $\nu \in \{x, y, z\}$ directions on site i (represented by Pauli matrices), $\hat{S}_i^\pm = \hat{S}_i^x \pm i\hat{S}_i^y$ are the corresponding ladder operators, and L is the number of lattice sites. Δ is the so-called anisotropy parameter in the XXZ chain, and $\lambda \neq 0$ breaks the integrability of the XXZ chain [105]. In Sec. 4.3, we set $\lambda = 1$ to study matrix elements of Hamiltonian (4.1) in the quantum-chaotic regime, while in Sec. 4.4 we set $\lambda = 0$ to study matrix elements at integrability. We mostly compare results for $\Delta = 0.55$ (easy-plane regime of the XXZ chain) and $\Delta = 1.1$ (easy-axis regime of the XXZ chain).

To study the matrix elements of observables in the energy eigenstates of Hamiltonian (4.1), it is important to resolve all of its symmetries [2,28]. First, we note that the Hamiltonian commutes with $\hat{M}^z = \sum_i \hat{S}_i^z$, which is the total magnetization in the z-direction. We focus on the zero magnetization sector of chains with an even number of lattice sites. This sector has an additional spin inversion (Z_2) symmetry; we focus on the even-Z_2 sector. Next, translational symmetry allows us to block-diagonalize the Hamiltonian in different total quasimomentum k sectors. Lastly, within the $k = 0$ and π sectors, we resolve the space reflection (P) symmetry.

We study the matrix elements of three local operators that break the translation symmetry of Hamiltonian (4.1): the nearest neighbor z-interaction

$$\hat{U}_\text{n} = \hat{S}_1^z\hat{S}_2^z, \tag{4.2}$$

the next-nearest neighbor z-interaction

$$\hat{U}_\text{nn} = \hat{S}_1^z\hat{S}_3^z, \tag{4.3}$$

and the next-nearest neighbor flip-flop operator

$$\hat{K}_{\rm nn} = \hat{S}_1^+ \hat{S}_3^- + \hat{S}_3^+ \hat{S}_1^- . \tag{4.4}$$

These local operators connect all total quasimomentum sectors of the Hamiltonian. Since the Hamiltonian is translationally invariant, the sites used to define $\hat{U}_{\rm n}$, $\hat{U}_{\rm nn}$, and $\hat{K}_{\rm nn}$ do not influence the results.

The first important consequence of the translational symmetry of the Hamiltonian is that the diagonal matrix elements of $\hat{U}_{\rm n}$, $\hat{U}_{\rm nn}$, and $\hat{K}_{\rm nn}$ (referred to in what follows as "symmetry-breaking" operators) are identical to the diagonal matrix elements of the corresponding translationally invariant operators (referred to in what follows as "symmetry-preserving" operators)

$$\hat{U}_{\rm n}^T = \frac{1}{L}\sum_{i=1}^{L} \hat{S}_i^z \hat{S}_{i+1}^z, \tag{4.5}$$

$$\hat{U}_{\rm nn}^T = \frac{1}{L}\sum_{i=1}^{L} \hat{S}_i^z \hat{S}_{i+2}^z, \tag{4.6}$$

$$\hat{K}_{\rm nn}^T = \frac{1}{L}\sum_{i=1}^{L} \left(\hat{S}_i^+ \hat{S}_{i+2}^- + \hat{S}_{i+2}^+ \hat{S}_i^- \right). \tag{4.7}$$

In addition, within a given total quasimomentum sector, the off-diagonal matrix elements of $\hat{U}_{\rm n}$, $\hat{U}_{\rm nn}$, and $\hat{K}_{\rm nn}$ are identical to those of $\hat{U}_{\rm n}^T$, $\hat{U}_{\rm nn}^T$, and $\hat{K}_{\rm nn}^T$, respectively.

The diagonal and the off-diagonal matrix elements of symmetry-preserving operators were studied in detail (within the $k = 0$ sector) in Ref. [45] (reproduced in Chapter 2). In this chapter our focus will be on off-diagonal matrix elements. In our discussions, by way of comparing the set of all matrix elements with the set of matrix elements that connect energy eigenstates from the same quasimomentum sector, we contrast the behaviors of matrix elements of the symmetry-breaking operators with those of their symmetry-preserving counterparts, respectively.

The off-diagonal matrix elements ($O_{\alpha\beta}$) of symmetry-breaking operators in the energy eigenstates are obtained using full exact diagonalization within the even-Z_2 sector of the $M^z = 0$ sector (with dimension $D_{Z_2}^e$) that, in turn, is split in L total quasimomentum k sectors. Whenever k_α or k_β are neither 0 nor π, one generally has $O_{\alpha\beta} \neq 0$. For the off-diagonal matrix elements within the $k = 0$, π sectors and between them, for which space reflection symmetry is resolved, we remove from our analyses the blocks of matrix

elements that are zero [1]. We note that, when reporting the $k_\alpha = k_\beta$ results for $O_{\alpha\beta}$, we exclude the $k = 0$ and π sectors (two out of L sectors) due to the extra symmetry present in those sectors.

The dimension D of the Hilbert space used in our normalization for each observable is the square root of the total number of matrix elements that do not vanish for symmetry reasons. Since the number of blocks with vanishing off-diagonal matrix elements is only $O(1)$, $D \simeq D^e_{Z_2}$. We carry out calculations for chains with up to $L = 22$, including all quasimomentum sectors. For matrix elements that connect eigenstates from the same quasimomentum sectors, we carry out calculations up to $L = 24$. For our low-frequency analyses, we also report results for the $k = 0$, even-P, even-Z_2 sector up to $L = 26$ [45].

4.3 Quantum-Chaotic Chain

In this section, we study the off-diagonal matrix elements of our observables of interest in the eigenstates of Hamiltonian (4.1) with $\Delta = 0.55$, 1.1, and $\lambda = 1$. We focus on the regime $\bar{E} = (E_\alpha + E_\beta)/2 \approx 0$, namely, on average energies at the center of the spectrum (the so-called infinite-temperature regime).

4.3.1 Distributions

Here we characterize the distribution of $|O_{\alpha\beta}|$. We take the absolute value because $O_{\alpha\beta}$ is complex whenever k_α or k_β are neither 0 nor π. In addition to considering $\bar{E} \approx 0$, we first focus on the regime in which $\omega = |E_\alpha - E_\beta| \approx 0$. In the context of the ETH ansatz, $|f_O(\bar{E}, \omega)|$ exhibits a plateau in this regime [2], and the distribution of $|O_{\alpha\beta}|$ is expected to be the same as in random matrix theory.

Figure 4.1 shows the probability distributions of $|(U_{\rm n})_{\alpha\beta}|$ [(a), (b)] and $|(U_{\rm nn})_{\alpha\beta}|$ [(c), (d)] for Hamiltonian (4.1) with $\Delta = 0.55$, in a chain with $L = 22$ (qualitatively similar results were obtained, not shown, for $|(K_{\rm nn})_{\alpha\beta}|$). Figures 4.1(a) and 4.1(c) show the distributions for pairs of energy eigenstates with $k_\alpha = k_\beta$, and Figs. 4.1(b) and 4.1(d) show the distributions for pairs that connect all quasimomentum sectors. In all panels in Fig. 4.1 we also show half-normal distributions, for which the variances are the same as those of the numerical results, as continuous black lines.

[1] Within the $k = 0$ ($k = \pi$) sector, the off-diagonal matrix elements vanish between blocks with different parity (under space reflection). Between the $k = 0$ and π sectors, the off-diagonal matrix elements of $\hat{U}_{\rm n}$ vanish between blocks with different parity, while they vanish for $\hat{U}_{\rm nn}$ and $\hat{K}_{\rm nn}$ between blocks with the same parity.

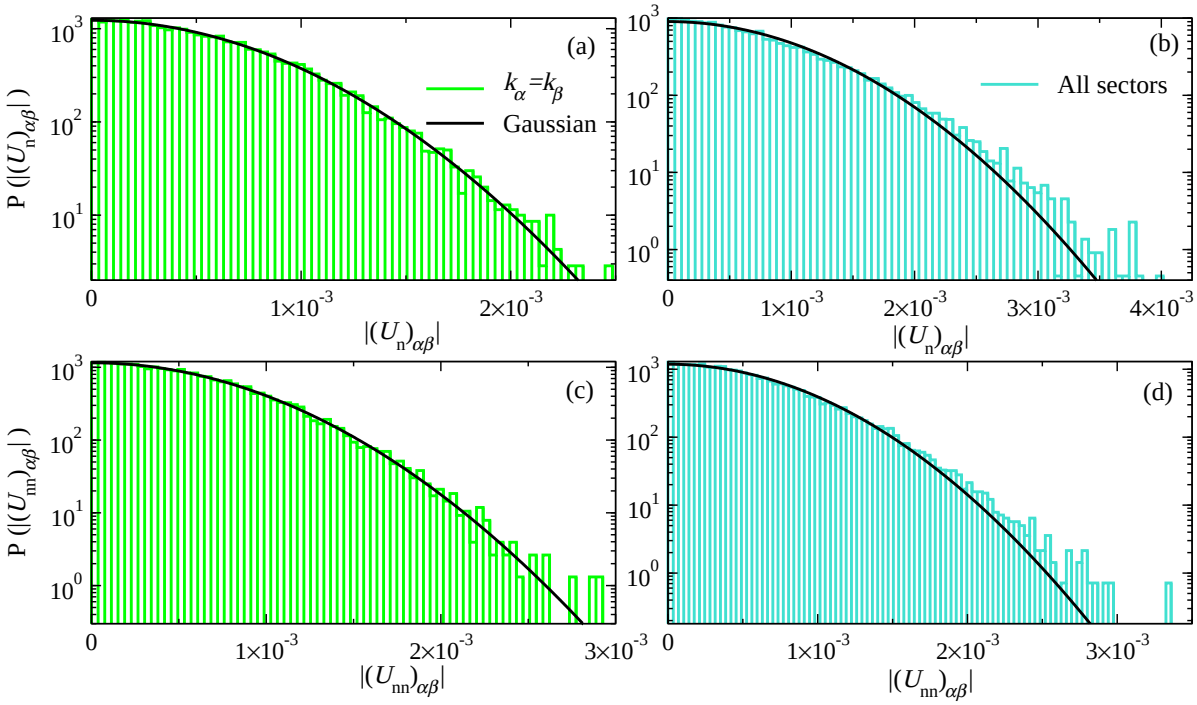

Figure 4.1 | **Probability distributions $P(|O_{\alpha\beta}|)$ for off-diagonal matrix elements.** We consider observables $\hat{U}_{\rm n}$ [(a), (b)] and $\hat{U}_{\rm nn}$ [(c), (d)] for Hamiltonian (4.1) with $\Delta = 0.55$ (similar results were obtained for $\Delta = 1.1$) and $\lambda = 1$ (quantum-chaotic regime). We consider pairs of energy eigenstates for which $|\bar{E}|/L \leq 0.025$, and choose the 40,000 matrix elements with the lowest ω (this results in $\omega \leq 0.001$). We show results for matrix elements with $k_\alpha = k_\beta$ (excluding the $k = 0$ and π sectors, we do the same in all plots that follow) [(a), (c)] and matrix elements that mix all quasimomentum sectors [(b), (d)], in the $L = 22$ chain. The continuous lines are half-normal distributions with the same variance as the distributions $P(|O_{\alpha\beta}|)$.

Overall, the results in Fig. 4.1 show that $|(U_{\rm n})_{\alpha\beta}|$ and $|(U_{\rm nn})_{\alpha\beta}|$ are normally distributed regardless of whether one looks at eigenstate pairs for which $k_\alpha = k_\beta$ (i.e., at symmetry-preserving operators) or at all eigenstate pairs (i.e., at symmetry-breaking operators). A comparison between the results in the left columns ($k_\alpha = k_\beta$) and the right columns (all eigenstate pairs) of Fig. 4.1 suggests that the variances of the distributions are generally different between the symmetry-preserving and the symmetry-breaking versions of any given observable, and that the magnitude of the difference depends on the observable. We continue to explore those observations in the next subsections.

Next, we probe the Gaussianity of the distributions of matrix elements for $\omega > 0$. For

that purpose we calculate the ratio [45]

$$\Gamma_O(\omega) = \overline{|O_{\alpha\beta}|^2}/\overline{|O_{\alpha\beta}|}^2. \tag{4.8}$$

In Eq. (4.8), $\overline{(\dots)}$ denotes a coarse-grained average (over small $\delta\omega$ windows) for pairs of energy eigenstates that satisfy $|\bar{E}|/L \leq 0.025$. If $O_{\alpha\beta}$ has a Gaussian distribution with zero mean, then $\Gamma_O(\omega) = \pi/2$. $\Gamma_O(\omega)$ has been computed recently for various models and observables [45, 130, 131, 135], as the normality of the distribution of off-diagonal matrix elements of observables has started to be used to identify the occurrence of eigenstate thermalization.

In Fig. 4.2(a), we show $\Gamma_{U_{\rm nn}}(\omega)$ for matrix elements that connect energy eigenstates with the same quasimomentum ($k_\alpha = k_\beta$) and, in Fig. 4.2(b), we show $\Gamma_{U_{\rm nn}}(\omega)$ for matrix elements that connect all sectors. The results in Fig. 4.2(a) appear to have converged to $\Gamma_{U_{\rm nn}}(\omega) = \pi/2$, with deviations at large values of ω occurring because of finite-size effects (the curves move toward $\pi/2$ with increasing L). Figure 4.2(b) contains deviations from Gaussianity (small bumps) for $\omega < 6$, but overall exhibits the same behavior as Fig. 4.2(a). Both other observables we studied ($\hat{U}_{\rm n}$ and $\hat{K}_{\rm nn}$) exhibited qualitatively similar behaviors for both sets of matrix elements, indicating that, for the chain sizes accessible to us: (i) the distributions of matrix elements appear to be Gaussian at all frequencies and (ii) finite-size effects (in the form of deviations from Gaussianity at intermediate values of ω)

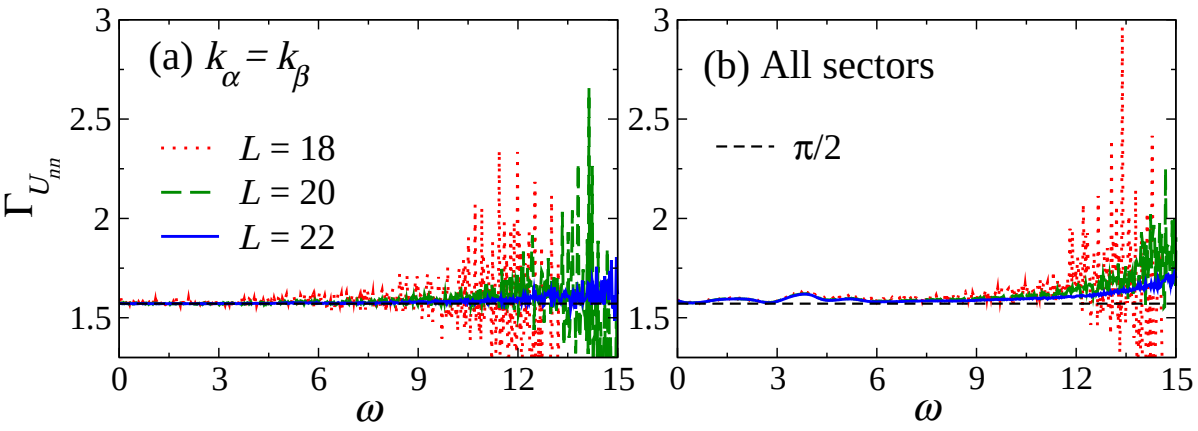

Figure 4.2 | **Gaussianity test of off-diagonal matrix elements.** $\Gamma_{U_{\rm nn}}$ [see Eq. (4.8)] at a nonintegrable point ($\lambda = 1$) of Hamiltonian (4.1) with $\Delta = 0.55$ for different chain sizes (similar results were obtained for $\Delta = 1.1$). We show results for pairs of energy eigenstates with $k_\alpha = k_\beta$ (a) and pairs that mix all quasimomentum sectors (b). All pairs of eigenstates satisfy $|\bar{E}|/L \leq 0.025$. The averages $\overline{|(U_{\rm nn})_{\alpha\beta}|}$ and $\overline{|(U_{\rm nn})_{\alpha\beta}|^2}$ were coarse-grained in windows of width $\delta\omega = 0.025$.

are stronger for symmetry-breaking observables than for symmetry-preserving ones.
In Ref. [45], for translationally invariant observables within the $k = 0$ quasimomentum sector, a small nearly L-independent deviation in $\Gamma_O(\omega)$ from $\pi/2$ was observed for $5 \lesssim \omega \lesssim 8$ (for the chain sizes available). That deviation was argued to be consistent with strong finite-size effects. In Fig. 4.2(a), which includes results from all pairs of energy eigenstates with $k_\alpha = k_\beta$, one can see that $\Gamma_{U_{\rm nn}}(\omega)$ approaches $\pi/2$ with increasing L in that frequency regime. This further strengthens the case that the deviations from Gaussianity seen in Ref. [45] for translationally invariant observables are the result of finite-size effects. In Fig. 4.2(b), and for $\hat{U}_{\rm n}$ and $\hat{K}_{\rm nn}$ (not shown), we see similar small nearly L-independent deviations from $\pi/2$. No such deviations have been observed in recent full exact diagonalization calculations in systems with broken translational symmetry [130, 131], so we attribute them here to strong finite-size effects for symmetry-breaking observables in our translationally invariant energy eigenstates. To further test this, we performed calculations for larger [but still $O(1)$] values of λ and found that the deviations from $\pi/2$ decrease deeper in the quantum chaotic regime.

4.3.2 Variances

Next we study the behavior of the off-diagonal matrix elements and their variances as functions of the frequency ω, as well as the scaling of the variances with system size. Since the average $\overline{O_{\alpha\beta}} = 0$, the variances are given by the averages $\overline{|O_{\alpha\beta}|^2}$, namely, $\mathrm{Var}(O_{\alpha\beta}) = \overline{|O_{\alpha\beta}|^2}$.
In Fig. 4.3, we visualize the distribution of $\log_{10}|(U_{\rm nn})_{\alpha\beta}|^2$ as a function of ω using normalized 2D histograms for matrix elements between pairs of energy eigenstates with $k_\alpha = k_\beta$ [Fig. 4.3(a)] and between pairs that connect all quasimomentum sectors [Fig. 4.3(b)]. In both panels, we have included matrix elements for pairs of energy eigenstates for which $\bar{E}/L \leq 0.025$, and used $\Delta = 0.55$ for chains with $L = 22$. The results are qualitatively similar in Fig. 4.3(a) and 4.3(b), and they are qualitatively similar to the results for translationally invariant operators in the $k = 0$ sector reported in Ref. [45]. This reveals that the matrix elements of symmetry-breaking operators are not qualitatively affected by the block diagonal structure of the Hamiltonian matrix.
In Fig. 4.3, we also plot the variances $\overline{|(U_{\rm nn})_{\alpha\beta}|^2}$ (solid lines) vs ω for the two sets of matrix elements considered. Comparing these variances makes apparent that they are qualitatively similar, but quantitatively different. The differences are best seen for $\omega \lesssim 5$. For $\omega \gtrsim 5$, both variances exhibit a similar exponential decay. Qualitatively similar results were obtained, not shown, for $\hat{U}_{\rm n}$ and $\hat{K}_{\rm nn}$.

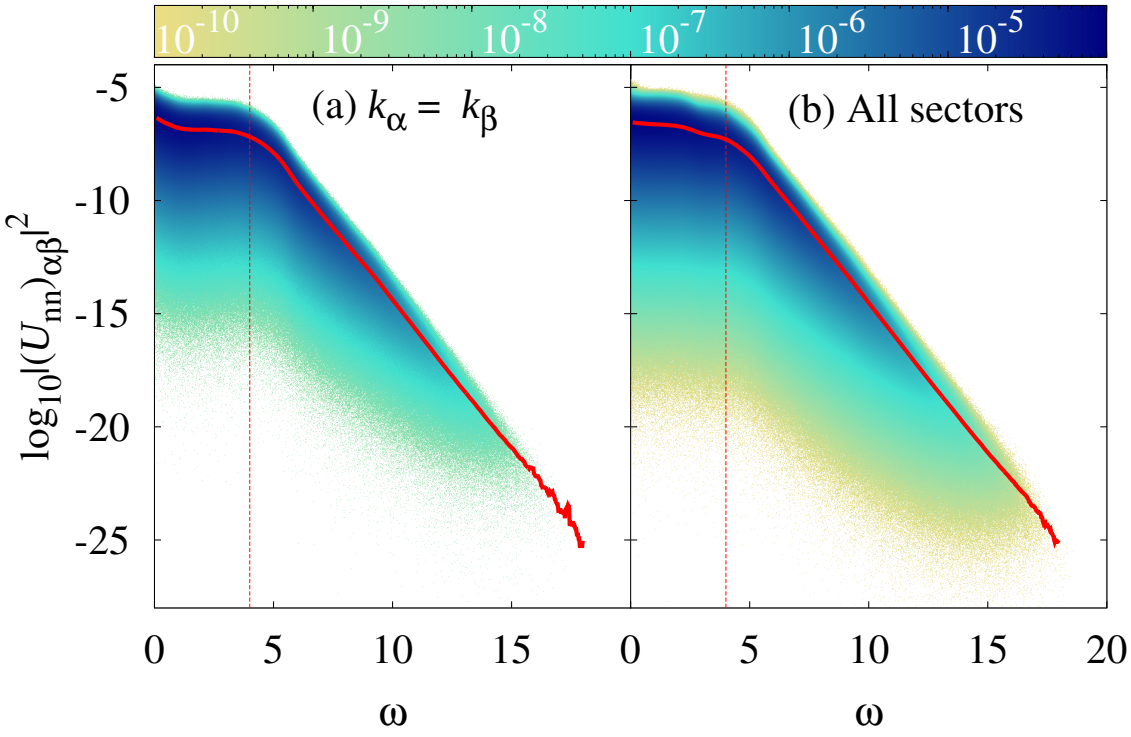

Figure 4.3 | **Normalized 2D histograms of** $\log_{10}|(U_{\mathbf{nn}})_{\alpha\beta}|^2$ **vs** ω**.** We consider a nonintegrable ($\lambda = 1$) point of Hamiltonian (4.1) with $\Delta = 0.55$ for $L = 22$ (qualitatively similar results were obtained for $\Delta = 1.1$). We consider pairs of energy eigenstates with $k_\alpha = k_\beta$ (a) and pairs that mix all quasimomentum sectors (b). All pairs of energy eigenstates satisfy $|\bar{E}|/L \leq 0.025$. The (red) solid lines are running averages $\log_{10}\overline{|(U_{\rm nn})_{\alpha\beta}|^2}$ calculated in windows of width $\delta\omega = 0.175$ centered at points separated by $\Delta\omega = 0.025$. The vertical dashed lines show the values of ω up to which results for $|O_{\alpha\beta}|^2$ are included in the scaling analysis of Fig. 4.4.

Next, we study the scaling of the variances. Figure 4.4 shows $\overline{|(U_{\rm n})_{\alpha\beta}|^2}$ [(a), (b)] and $\overline{|(U_{\rm nn})_{\alpha\beta}|^2}$ [(c), (d)] for $\Delta = 0.55$, 1.1 in chains with $L = 16 - 22$. The averages are calculated over frequencies $\omega < 4$ (qualitatively similar results were obtained averaging over other intervals of frequencies, see also Ref. [45]). The ETH ansatz (1.14) advances that the variances should scale as $1/D$ in the "infinite-temperature" regime, where $e^{S(\bar{E})} \simeq D$. The results in Fig. 4.4 confirm that the variances for both observables and both sets of matrix elements (those for which $k_\alpha = k_\beta$ [(a), (c)] and those that connect all k-sectors [(b), (d)]) scale as $1/D$. In this respect, matrix elements of symmetry-breaking observables are no different than those of symmetry-preserving ones, despite the fact that the latter are nonvanishing only for $k_\alpha = k_\beta$.

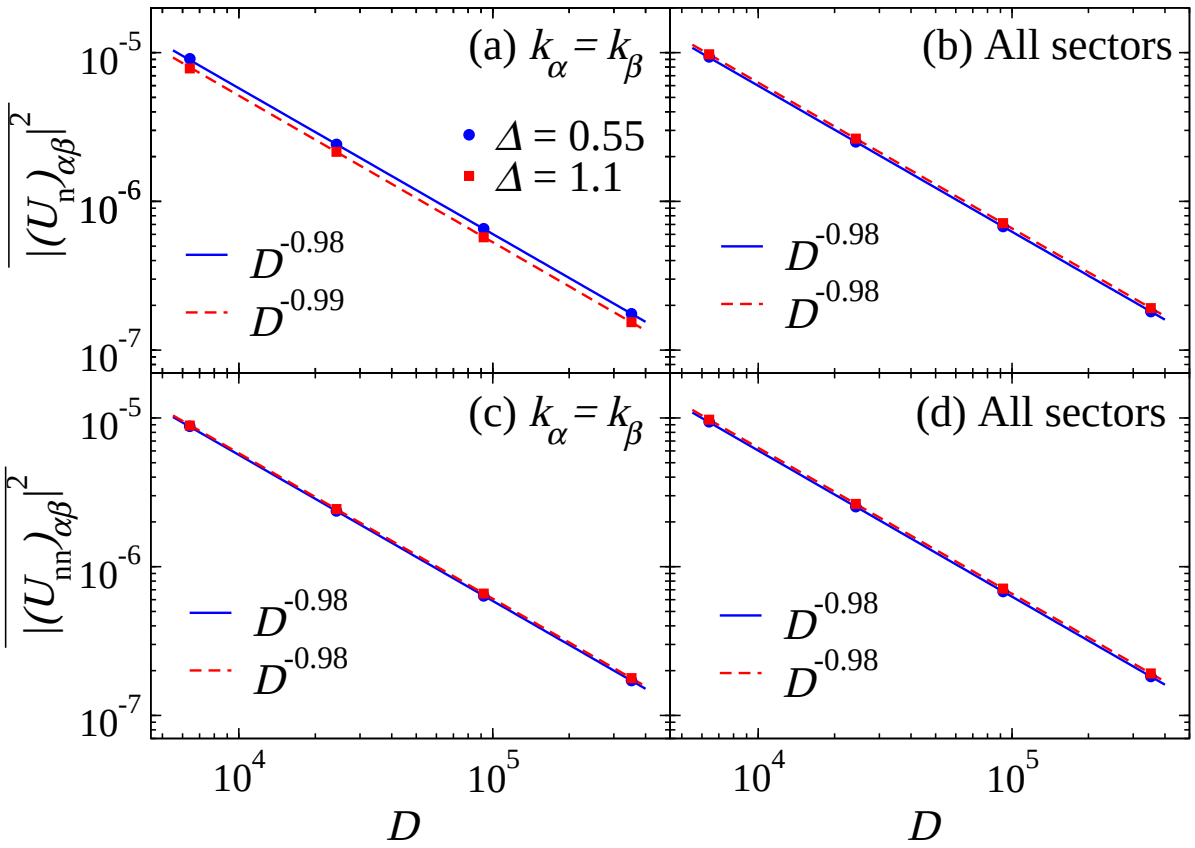

Figure 4.4 | **Scaling of the variance of off-diagonal matrix elements.** We plot $\overline{|(U_n)_{\alpha\beta}|^2}$ [(a), (b)] and $\overline{|(U_{nn})_{\alpha\beta}|^2}$ [(c), (d)] vs D at the nonintegrable ($\lambda = 1$) point of Hamiltonian (4.1) with $\Delta = 0.55$ and 1.1. We consider pairs of energy eigenstates with $k_\alpha = k_\beta$ [(a), (c)] and pairs that mix all quasimomentum sectors [(b), (d)]. The straight lines show power-law fits to the results for $L = 18$ through $L = 22$. The average over $|O_{\alpha\beta}|^2$ for different chain sizes was calculated using pairs of energy eigenstates that satisfy $|\bar{E}|/L \leq 0.025$. We restricted the average to pairs of eigenstates for which $\omega < 4$, the regime in which the variances exhibit a plateau-like behavior in Fig. 4.3 (see Ref. [45] for scalings when one averages over all frequencies).

4.3.3 Scaled Variances

The results in Fig. 4.4 suggest that, for $\bar{E} \approx 0$, one can define a Hilbert-space-size independent scaled variance

$$|f_O(0,\omega)|^2 = D\,\mathrm{Var}(O_{\alpha\beta}), \tag{4.9}$$

as advanced by the ETH (1.14).

In Fig. 4.5, we plot the scaled variance $|f_{U_{nn}}(0,\omega)|^2$ for three chain sizes. One can see

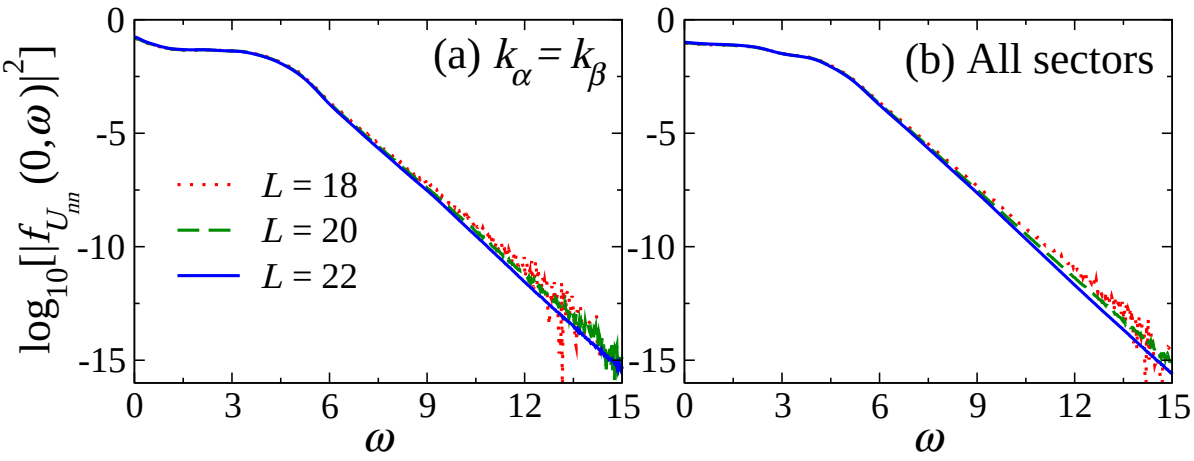

Figure 4.5 | **Scaled variance $|f_{U_{\rm nn}}(0,\omega)|^2$ vs ω.** We consider the nonintegrable ($\lambda = 1$) point of Hamiltonian (4.1) with $\Delta = 0.55$ for different chain sizes L (qualitatively similar results were obtained for $\Delta = 1.1$). We show results for pairs of energy eigenstates with $k_\alpha = k_\beta$ (a) and pairs that mix all quasimomentum sectors (b). All pairs of eigenstates satisfy $|\bar{E}|/L \leq 0.025$. The averages $\overline{|(U_{\rm nn})_{\alpha\beta}|^2}$ were coarse-grained in windows of width $\delta\omega = 0.025$.

that there is excellent data collapse away from the exponential regime at high ω. In the latter regime, the scaled variances for contiguous chain sizes collapse over a larger ω window with increasing L. This points to finite-size effects as the reason for the lack of data collapse at high ω. Larger finite-size effects are expected in finite chains at high frequencies because the matrix elements probe pairs of energy eigenstates at opposite edges of the energy spectrum [45]. Qualitatively similar results were found for all three observables studied irrespective of the Hamiltonian parameter Δ. Altogether, our calculations show that for symmetry-breaking observables the function $|f_O(0,\omega)|^2$ is a well-defined smooth function of ω.

We note that, for translationally invariant intensive observables such as the ones in Eqs. (4.5)–(4.7), which have a Hilbert-Schmidt norm that scales as $1/\sqrt{L}$, the scaled variance was computed in Ref. [45] as

$$|f_O^T(0,\omega)|^2 = \mathcal{D}L\,\mathrm{Var}(O^T_{\alpha\beta}), \tag{4.10}$$

where $\mathcal{D}$ was the dimension of the specific symmetry sector considered. The results from Eq. (4.10) are consistent with the results from Eq. (4.9) when one restricts the variance in the latter to only include pairs of states with $k_\alpha = k_\beta$. This is the case because, for $k_\alpha = k_\beta$, $\mathrm{Var}(O_{\alpha\beta}) = \mathrm{Var}(O^T_{\alpha\beta})$ and $D \simeq \mathcal{D}L$.

4.3.4 Low-Frequency Scaling

For local operators in quantum chaotic systems, because of diffusion, one expects all dynamics to occur within times that scale with L^2. In the frequency domain, this means that $|f_O(\bar{E},\omega)|^2$ is expected to exhibit a plateau as $\omega \to 0$ whose size (which defines the so-called Thouless energy) scales as $1/L^2$. Below the Thouless energy, the

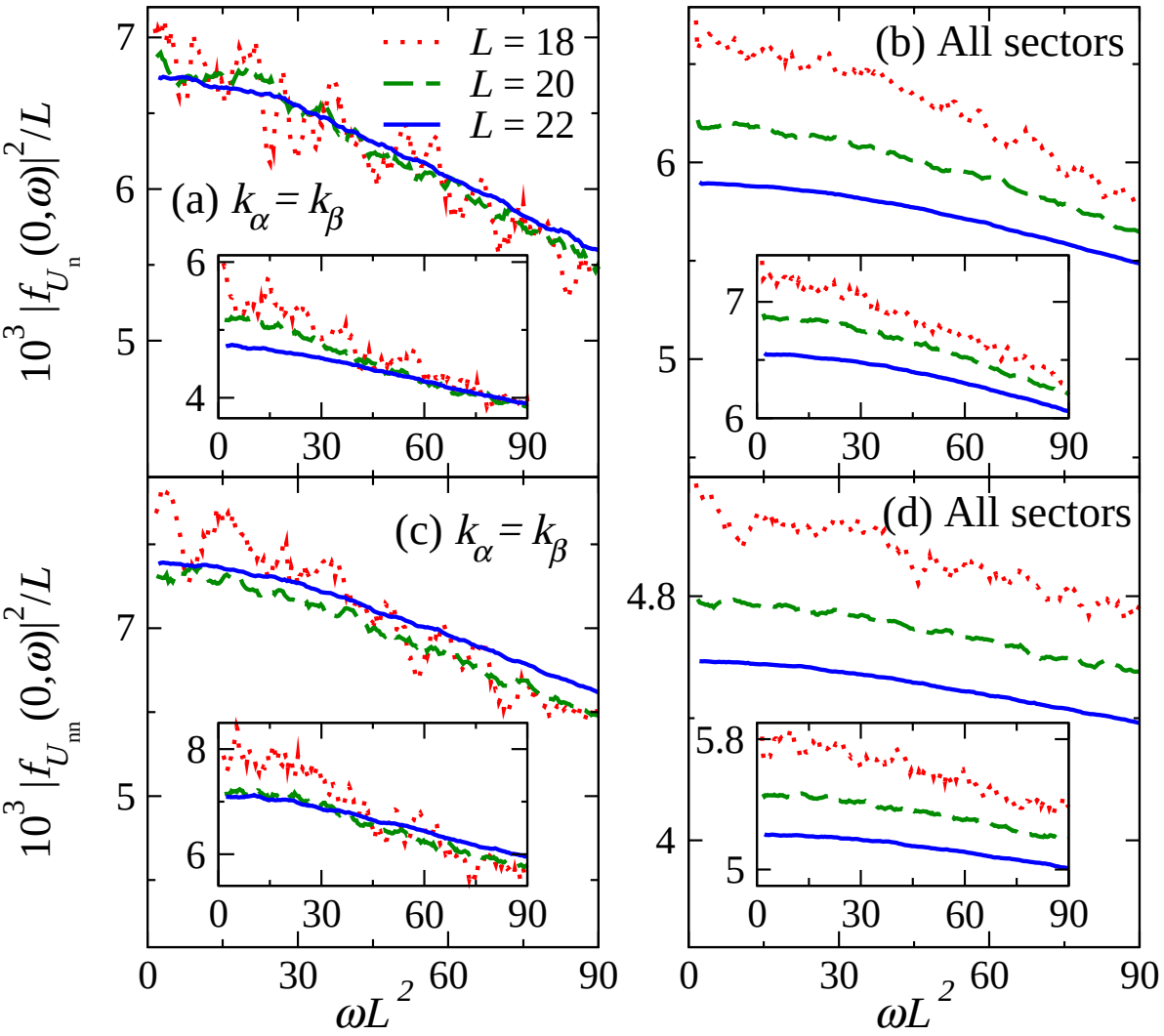

Figure 4.6 | **Low-frequency plots of the scaled variances $|f_O(0,\omega)|^2/L$ vs ωL^2 ($k_\alpha = k_\beta$ vs. all sectors).** We consider observables $\hat{U}_{\rm n}$ [(a), (b)] and $\hat{U}_{\rm nn}$ [(c), (d)] at the nonintegrable ($\lambda = 1$) point of Hamiltonian (4.1), with $\Delta = 0.55$ (main panels) and 1.1 (insets), for different chain sizes L. We consider pairs of energy eigenstates with $k_\alpha = k_\beta$ [(a), (c)] and pairs that mix all quasimomentum sectors [(b), (d)]. All pairs of eigenstates satisfy $|\bar{E}|/L \leq 0.025$. The running averages $\overline{|O_{\alpha\beta}|^2}$ were calculated in windows of width $\delta\omega = 0.009$ centered at points separated by $\Delta\omega = 0.001$.

ETH ansatz coincides with the (featureless) predictions of random matrix theory. The magnitude of $|f_O(\bar{E},\omega)|^2$ in the plateau is expected to be proportional to L [2]. Such expectations have been confirmed in lattice systems with no translational symmetry (but no disorder) [2, 131], and the plateau has also been observed and its size characterized in systems with weak disorder [137].

Next, we study the low-frequency behavior of $|f_O(\bar{E},\omega)|^2$ for translational symmetry-breaking and symmetry-preserving operators in the energy eigenstates of the translationally invariant Hamiltonian (4.1) with $\lambda = 1$ (in the quantum-chaotic regime).

In Fig. 4.6, we plot $|f_O(0,\omega)|^2/L$ vs ωL^2 for $\hat{U}_{\rm n}$ [(a), (b)] and $\hat{U}_{\rm nn}$ [(c), (d)] using pairs of energy eigenstates with $k_\alpha = k_\beta$ [(a), (c)] and pairs that connect all quasimomentum sectors [(b), (d)]. The main panels (insets) show results for $\Delta = 0.55$ ($\Delta = 1.1$). All the results reported in Fig. 4.6 are consistent with the function $|f_O(0,\omega L^2)|^2/L$ becoming system-size independent for large systems at low ω. Namely, they are consistent with the scaling advanced for quantum chaotic systems [2]. From Fig. 4.6, given the finite-size effects, it remains a challenge to extract the Thouless energy.

Since the results in Fig. 4.6 for pairs of energy eigenstates with $k_\alpha = k_\beta$ [(a), (c)] are qualitatively similar to those of pairs that connect all quasimomentum sectors [(b), (d)], albeit with smaller finite-size effects in the former (i.e., for symmetry-preserving observables) than in the latter (i.e., for symmetry-breaking observables), we focus on symmetry-preserving observables next. In Figs. 4.7(a) and 4.7(c), we plot $|f_O(0,\omega)|^2/L$ vs ωL^2 for $\hat{U}_{\rm n}$ and $\hat{K}_{\rm nn}$, respectively, in pairs of energy eigenstates with $k_\alpha = k_\beta$ for chains with up to $L = 24$, for $\Delta = 0.55$ (main panels) and for $\Delta = 1.1$ (insets). The agreement between the results for $\Delta = 1.1$ (insets) in the two largest chains is much better than in Fig. 4.6 [finite-size effects remain large for $\Delta = 0.55$ (main panels)]. The results in Figs. 4.7(a) and 4.7(c) further strengthen the expectation that the function $|f_O(0,\omega L^2)|^2/L$ becomes, at low ω, system-size independent for large systems.

In Figs. 4.7(b) and 4.7(d), we plot $|f^T_O(0,\omega)|^2/L$ vs ωL^2 for $\hat{U}^T_{\rm n}$ and $\hat{K}^T_{\rm nn}$, in the even-Z_2, even-P subsector of the $k = 0$ sector for chains with up to $L = 26$, for $\Delta = 0.55$ (main panels) and for $\Delta = 1.1$ (insets). These are low-frequency results corresponding to the scaled variances reported in Ref. [45] for intermediate and large values of ω. Figures 4.7(b) and 4.7(d) show that the behavior in the $k = 0$ sector is qualitatively similar to the behavior for all pairs of energy eigenstates with $k_\alpha = k_\beta$ [Figs. 4.7(a) and 4.7(c)], but exhibits stronger finite-size effects. This suggests that, in exact diagonalization studies of matrix elements of translationally invariant operators, it may be better (in terms of reducing finite-size effects) to study averages over all quasimomentum sectors (excluding

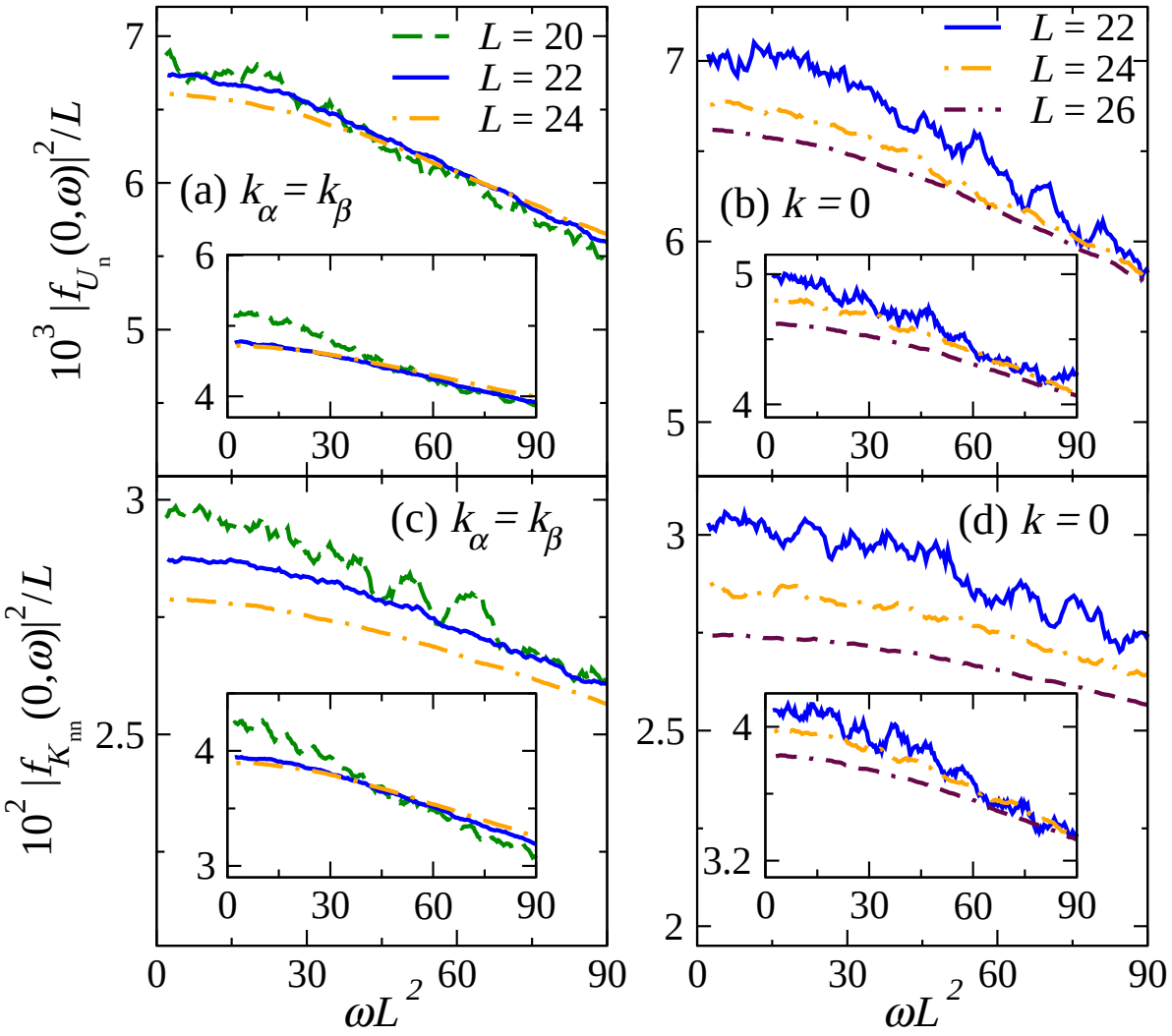

Figure 4.7 | **Low-frequency plots of the scaled variances $|f_O(0,\omega)|^2/L$ vs ωL^2 ($k_\alpha = k_\beta$ vs. $k = 0$).** We consider observables $\hat{U}_{\rm n}$ (a) and $\hat{K}_{\rm nn}$ (c), and of $|f_O^T(0,\omega)|^2/L$ for observables $\hat{U}_{\rm n}^T$ (b) and $\hat{K}_{\rm nn}^T$ (d), at the nonintegrable ($\lambda = 1$) point of Hamiltonian (4.1), with $\Delta = 0.55$ (main panels) and 1.1 (insets), for different chain sizes L. We consider pairs of energy eigenstates with $k_\alpha = k_\beta$ [(a), (c)] and within the even-Z_2, even-P sub-sector of the $k = 0$ sector [(b), (d)]. All pairs of eigenstates satisfy $|\bar{E}|/L \leq 0.025$. The running averages $\overline{|O_{\alpha\beta}|^2}$ were calculated in windows of width $\delta\omega = 0.009$ centered at points separated by $\Delta\omega = 0.001$.

the $k = 0$ and π sectors) in smaller chains than to focus on the $k = 0$ sector in larger ones.

4.4 Interacting Integrable Chain

Next, for the interacting integrable XXZ chain [$\lambda = 0$ in Hamiltonian (4.1)], we carry out an analysis parallel to the one in the previous section. We show that the key results of Ref. [45] remain valid for symmetry-breaking observables, including a skewed log-normal-like distribution of off-diagonal matrix elements and a variance that is a smooth function of ω that scales as $1/D$. Additionally, we extend the analysis of Ref. [45] by identifying low-frequency ballistic and diffusive scalings of the variance of the off-diagonal matrix elements of both symmetry-breaking and symmetry-preserving observables. Lastly, we highlight differences between integrability-breaking and integrability-preserving observables, supporting the findings of Refs. [42, 131].

4.4.1 Distributions

Figure 4.8 shows the distributions of $|O_{\alpha\beta}|$ for $\hat{U}_{\rm n}$ [(a), (b)] and $\hat{U}_{\rm nn}$ [(c), (d)] for matrix elements for which $\bar{E} \approx 0$ and $\omega \approx 0$. One can see that, regardless of whether matrix elements connect pairs of eigenstates from the same quasimomentum sectors [(a), (c)] or from all sectors [(b), (d)], the distributions are close to log-normal (the solid black lines are log-normal distributions with the same mean and variance as $\ln|O_{\alpha\beta}|$). Qualitatively similar results were obtained (not shown) for other frequencies, and for $\hat{K}_{\rm nn}$.

A closer inspection of the distributions of $\ln|O_{\alpha\beta}|$ (insets) reveals the nature of the differences between the $P(|O_{\alpha\beta}|)$ and log-normal distributions. Specifically, the insets show that the $\ln|O_{\alpha\beta}|$ distributions are skewed normal, with a skewness that depends both on the observable [compare the insets in Figs. 4.8(a) and 4.8(c)] and on whether one looks at matrix elements that connect energy eigenstates from the same [Figs. 4.8(a) and 4.8(c)] or from all [Figs. 4.8(b) and 4.8(d)] quasimomentum sectors. For the three observables and the two values of Δ ($\Delta = 0.55$ and 1.1) studied, we found that the distributions of matrix elements involving eigenstates from all quasimomentum sectors are the ones that exhibit a higher skewness. In Appendix 4.7, we report a preliminary analysis that suggests that the distributions are skewed log-normal-like in the thermodynamic limit.

4.4.2 Variances

The lack of normality in the distribution of off-diagonal matrix elements of observables in integrable models means that the variance of the distribution does not determine

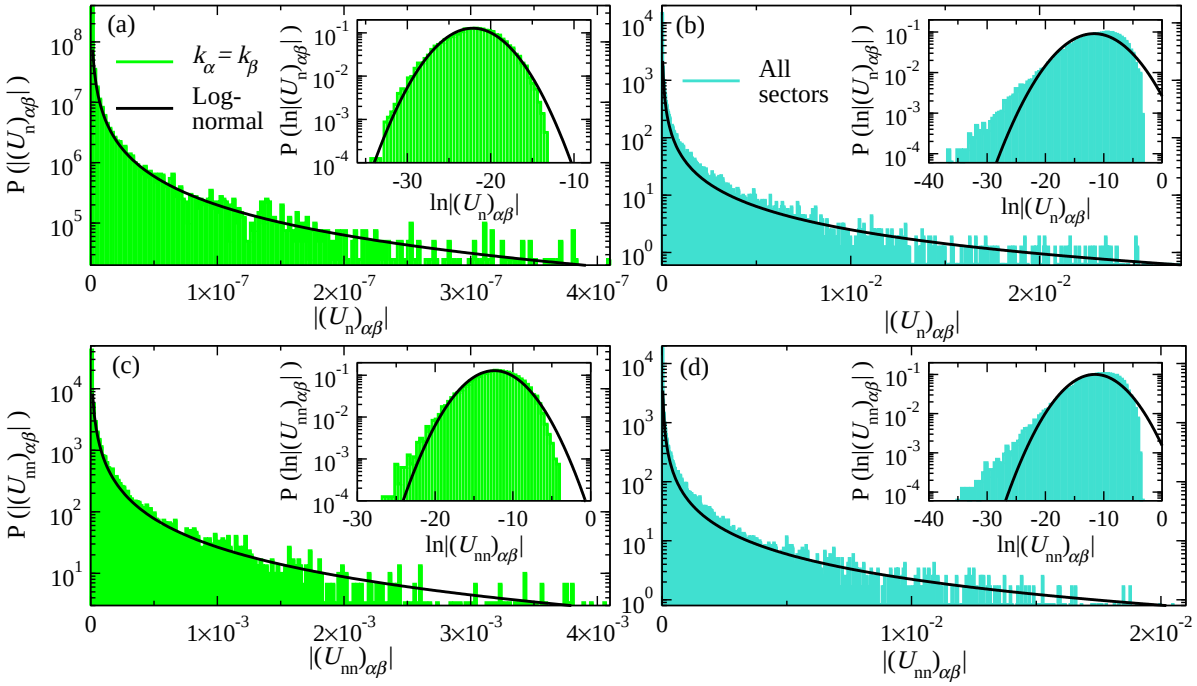

Figure 4.8 | **Probability distributions $P(|O_{\alpha\beta}|)$ of off-diagonal matrix elements.** We consider observables $\hat{U}_{\rm n}$ [(a), (b)] and $\hat{U}_{\rm nn}$ [(c), (d)] for Hamiltonian (4.1) with $\Delta = 0.55$ (similar results were obtained for $\Delta = 1.1$) and $\lambda = 0$ (the integrable XXZ chain). We consider pairs of energy eigenstates for which $|\bar{E}|/L \leq 0.025$, and choose the 40,000 matrix elements with the lowest ω (this results in $\omega \leq 0.001$). We show results for matrix elements with $k_\alpha = k_\beta$ [(a), (c)] and matrix elements that mix all quasimomentum sectors [(b), (d)] in the $L = 22$ chain. The insets show the probability distributions $P(\ln|O_{\alpha\beta}|)$, along with Gaussian distributions (continuous lines) with the same mean and variance. The continuous lines in the main panels are the corresponding log-normal distributions.

other moments. Thus, there is no meaningful equivalent of the off-diagonal part of the ETH (1.14) in integrable systems. Still, the variance $\mathrm{Var}(O_{\alpha\beta}) = \overline{|O_{\alpha\beta}|^2}$ (because $\overline{O_{\alpha\beta}} = 0$) is what is physically relevant, e.g., for fluctuation-dissipation relations [2, 29], heating rates [1], transport properties [30, 130], and the multipartite entanglement structure of energy eigenstates [138]. Thus, next, we seek to characterize the variance of the distribution of off-diagonal elements for symmetry-breaking observables and compare it to that of symmetry-preserving ones in the integrable XXZ chain.

In Fig. 4.9, we show normalized 2D histograms of $\log_{10}|(U_{\rm nn})_{\alpha\beta}|^2$ for pairs of energy eigenstates that satisfy $|\bar{E}|/L \leq 0.025$ in chains with $L = 22$. We report results for $\Delta = 0.55$ (the ones obtained for $\Delta = 1.1$, not shown, are qualitatively similar) between pairs of eigenstates with $k_\alpha = k_\beta$ [Fig. 4.9(a)] and between pairs that connect

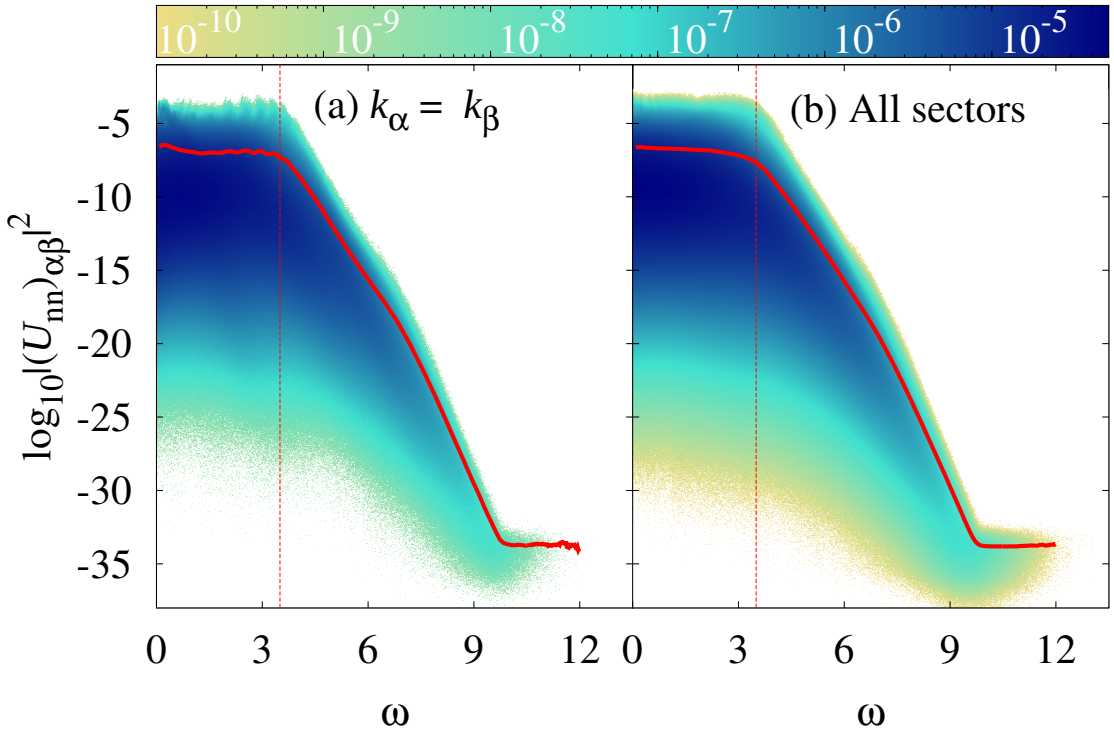

Figure 4.9 | **Normalized 2D histograms of** $\log_{10}|(U_{\mathbf{nn}})_{\alpha\beta}|^2$ **vs** ω**.** We consider the XXZ chain with $\Delta = 0.55$ for $L = 22$ (qualitatively similar results were obtained for $\Delta = 1.1$). We consider pairs of energy eigenstates with $k_\alpha = k_\beta$ (a) and pairs that mix all quasimomentum sectors (b). All pairs of energy eigenstates satisfy $|\bar{E}|/L \leq 0.025$. The (red) solid lines are running averages $\log_{10}\overline{|(U_{\rm nn})_{\alpha\beta}|^2}$ calculated in windows of width $\delta\omega = 0.175$ centered at points separated by $\Delta\omega = 0.025$. The vertical dashed lines show the values of ω up to which results for $|O_{\alpha\beta}|^2$ are included in the scaling analysis of Fig. 4.10.

all quasimomentum sectors [Fig. 4.9(b)]. We note that the results in Fig. 4.9(a) are qualitatively similar to those reported in Ref. [45] for translationally invariant observables in the $k = 0$ sector. As in Ref. [45], the support of the distribution for $\hat{U}_{\rm nn}$ is much broader for the interacting integrable system [Fig. 4.9(a)] than for the nonintegrable one [Fig. 4.3(a)]. Also, in Fig. 4.9(a), no significant fraction of matrix elements has a vanishing magnitude as seen in quadratic models [29]. Because of this, for interacting integrable models, one can define a meaningful average $\overline{|O_{\alpha\beta}|^2}$ at each value of ω. Figure 4.9(b) shows that the same is true for symmetry-breaking observables that connect all quasimomentum sectors.

The (red) solid lines in Fig. 4.9 show the ω-resolved variances of $|(U_{\rm nn})_{\alpha\beta}|$. As in the quantum chaotic case (Fig. 4.3), differences can be seen in the variances of matrix elements connecting the same quasimomentum sectors [Fig. 4.9(a)] and all sectors [Fig. 4.9(b)] for

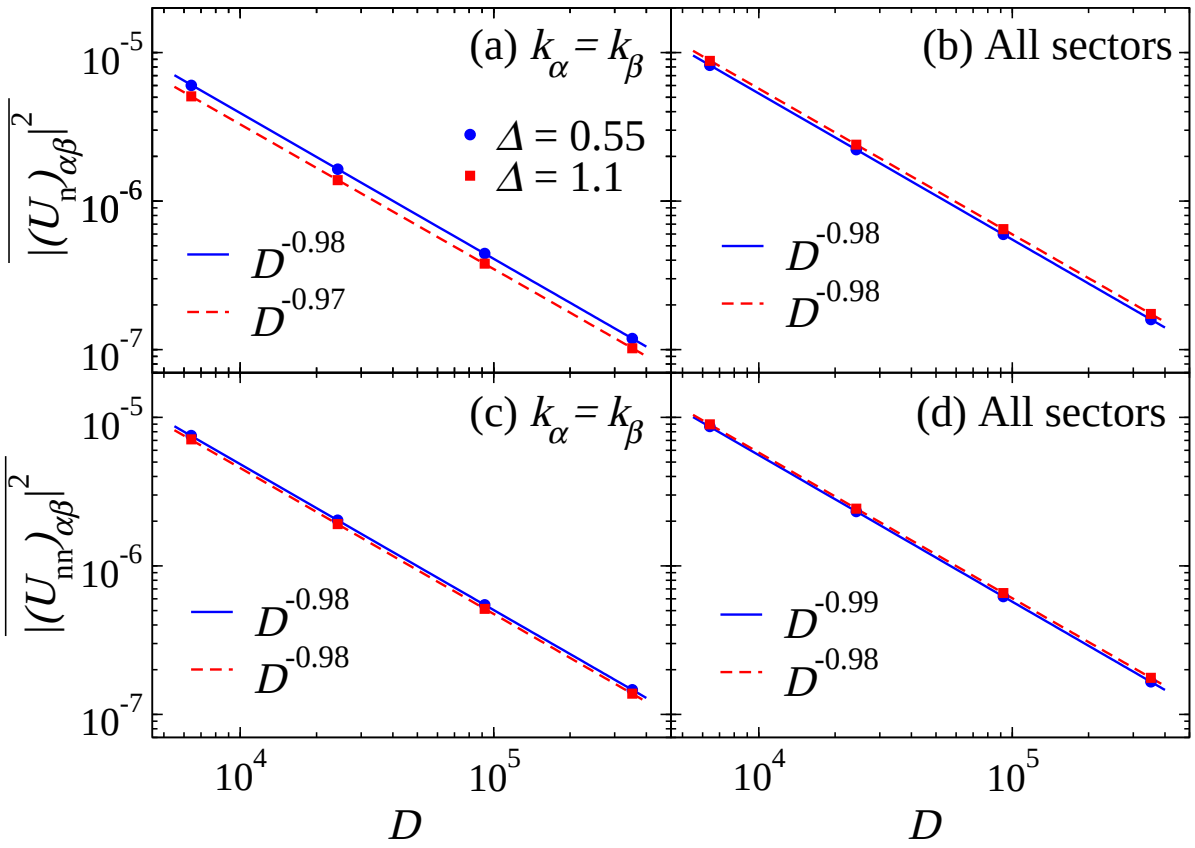

Figure 4.10 | **Scaling of the variance of off-diagonal matrix elements.** We plot $\overline{|(U_{\rm n})_{\alpha\beta}|^2}$ [(a), (b)] and $\overline{|(U_{\rm nn})_{\alpha\beta}|^2}$ [(c), (d)] vs D in the (integrable) XXZ chain with $\Delta = 0.55$ and 1.1. We consider pairs of energy eigenstates with $k_\alpha = k_\beta$ [(a), (c)] and pairs that mix all quasimomentum sectors [(b), (d)]. The straight lines show power-law fits to the results for $L = 18$ through $L = 22$. The average over $|O_{\alpha\beta}|^2$ for different chain sizes was calculated using pairs of energy eigenstates that satisfy $|\bar{E}|/L \leq 0.025$. We restricted the average to pairs of eigenstates for which $\omega < 3.5$, the regime in Fig. 4.9 in which the variances exhibit a plateau-like behavior (see Ref. [45] for scalings when one averages over all frequencies).

$\omega \lesssim 4$. The exponential and Gaussian regimes at high ω (see Ref. [45]) are similar in both sets of matrix elements.

Next, we study how the variances scale with increasing chain size. In Fig. 4.10, we show finite-size scaling analyses of the variance $\overline{|O_{\alpha\beta}|^2}$ vs D for $\hat{U}_{\rm n}$ [(a), (b)] and $\hat{U}_{\rm nn}$ [(c), (d)] for chains with $L = 16 - 22$. The average is calculated over frequencies $\omega < 3.5$ (qualitatively similar results were obtained averaging over other intervals of frequencies, see also Ref. [45]). As found in Ref. [45] for translationally invariant observables in the $k = 0$ sector of the XXZ chain, all variances in Fig. 4.10 scale as $1/D$ (as they do in the quantum chaotic system in Fig. 4.4). This occurs regardless of whether the matrix

elements are computed between pairs of energy eigenstates from the same quasimomentum sector [(a), (c)] or between pairs that mix all quasimomentum sectors [(b), (d)].

4.4.3 Scaled Variances

The results in Fig. 4.10 suggest that, for $\bar{E} \approx 0$, one can define a Hilbert-space-size independent scaled variance

$$V_O(0,\omega) = D\,\mathrm{Var}(O_{\alpha\beta}), \tag{4.11}$$

as for quantum-chaotic systems (4.9). Note that we use a different label for the scaled variance in integrable systems to emphasize that there is no equivalent of the off-diagonal part of the ETH (1.14) for them.

In Fig. 4.11, we plot the scaled variance $V_{U_{\mathrm{nn}}}(0,\omega)$ for three chain sizes. The results in Fig. 4.11(a) confirm the data collapse expected from Ref. [45] for symmetry-preserving observables, while the results in Fig. 4.11(b) demonstrate that the same is true for symmetry-breaking ones. We note that, for translationally invariant intensive observables such as the ones in Eqs. (4.5)–(4.7), which have a Hilbert-Schmidt norm that scales as

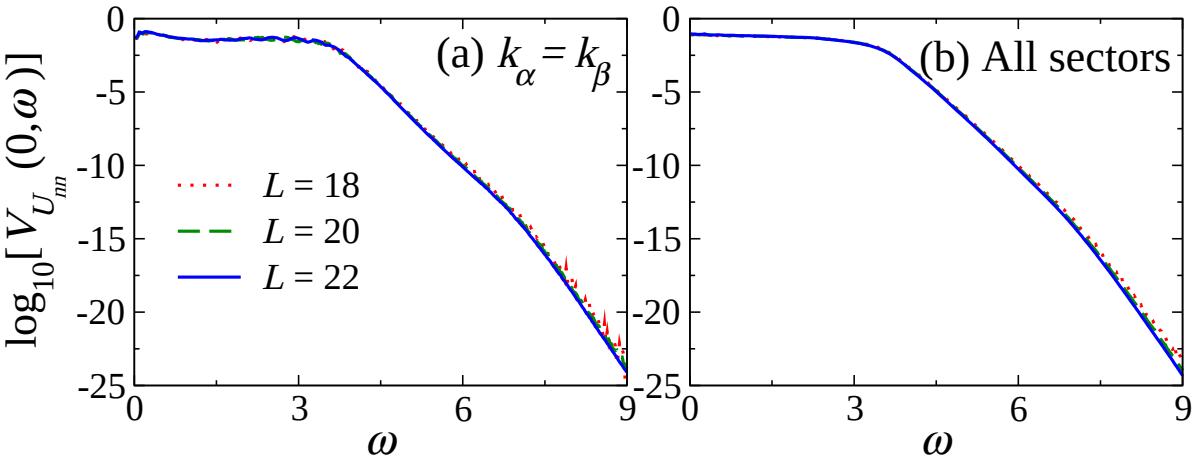

Figure 4.11 | **Scaled variance $V_{U_{\mathrm{nn}}}(0,\omega)$ vs ω.** We consider the XXZ chain with $\Delta = 0.55$ for different chain sizes L (qualitatively similar results were obtained for $\Delta = 1.1$). We show results for pairs of energy eigenstates with $k_\alpha = k_\beta$ (a) and pairs that mix all quasimomentum sectors (b). All pairs of eigenstates satisfy $|\bar{E}|/L \leq 0.025$. The averages $\overline{|(U_{\mathrm{nn}})_{\alpha\beta}|^2}$ were coarse-grained in windows of width $\delta\omega = 0.025$.

$1/\sqrt{L}$, the scaled variance was computed in Ref. [45] as

$$V_O^T(0,\omega) = \mathcal{D}L\,\mathrm{Var}(O_{\alpha\beta}^T), \tag{4.12}$$

where $\mathcal{D}$ was the dimension of the specific symmetry sector considered. The results from Eq. (4.12) are consistent with the results from Eq. (4.11) for states with $k_\alpha = k_\beta$ because $\mathrm{Var}(O_{\alpha\beta}) = \mathrm{Var}(O_{\alpha\beta}^T)$ and $D \simeq \mathcal{D}L$.

In Fig. 4.11, finite-size effects are smaller for the smallest values of $V_{U_{\rm nn}}(0,\omega)$ computed than in nonintegrable systems (see Fig. 4.5). The reason is that $V_{U_{\rm nn}}(0,\omega)$ decays more quickly with ω in integrable systems [1,45] so that, for the smallest values of $V_{U_{\rm nn}}(0,\omega)$ computed (limited by the machine precision) for the largest chains, the matrix elements are not probing the edges of the spectrum.

Overall, the results in Fig. 4.11 strengthen the conclusion in Ref. [45], explored recently in non-translationally invariant XXZ chains [130, 131], that in interacting integrable systems there is a well defined scaled variance $V_O(\bar{E},\omega)$. As per our results here, the scaled variance is well defined even for observables that break Hamiltonian symmetries.

4.4.4 Low-Frequency Scaling

Next we study the low-frequency behavior of the scaled variances $V_O(0,\omega)$. Two recent works [130, 131] have studied the low-frequency behavior of scaled variances of non-translationally invariant operators like the ones in Eqs. (4.2)–(4.4), and of averages like the ones in Eqs. (4.5)–(4.7), in the XXZ chain with open boundary conditions (namely, without translational symmetry). For the average spin current operator per site, in Ref. [130] it was shown that the scaled variance exhibits a large low-frequency peak in the easy-plane regime ($\Delta = 0.55$) whose height is proportional to L and location in frequency scales as $1/L$. The area under the peak does not change with increasing system size, and in the thermodynamic limit it is expected to signal ballistic DC transport (the peak would be at $\omega = 0$ and it would have a nonzero weight) [47,139]. Such a peak was absent in the scaled variance in the easy-axis ($\Delta = 1.1$) regime [130]. For other observables, the results in Ref. [131] are qualitatively similar to results that we report here so we will mention them along with our discussion.

In Fig. 4.12, we plot $V_O(0,\omega)/L$ vs ωL in chains with up to $L = 22$ for $\hat{U}_{\rm n}$ [(a), (b)], $\hat{U}_{\rm nn}$ [(c), (d)], and $\hat{K}_{\rm nn}$ [(e), (f)]. In the left column [(a), (c), (e)], we show results for pairs of energy eigenstates from the same quasimomentum sectors and, in the right column [(b), (d), (f)], we show results for pairs that connect all quasimomentum sectors.

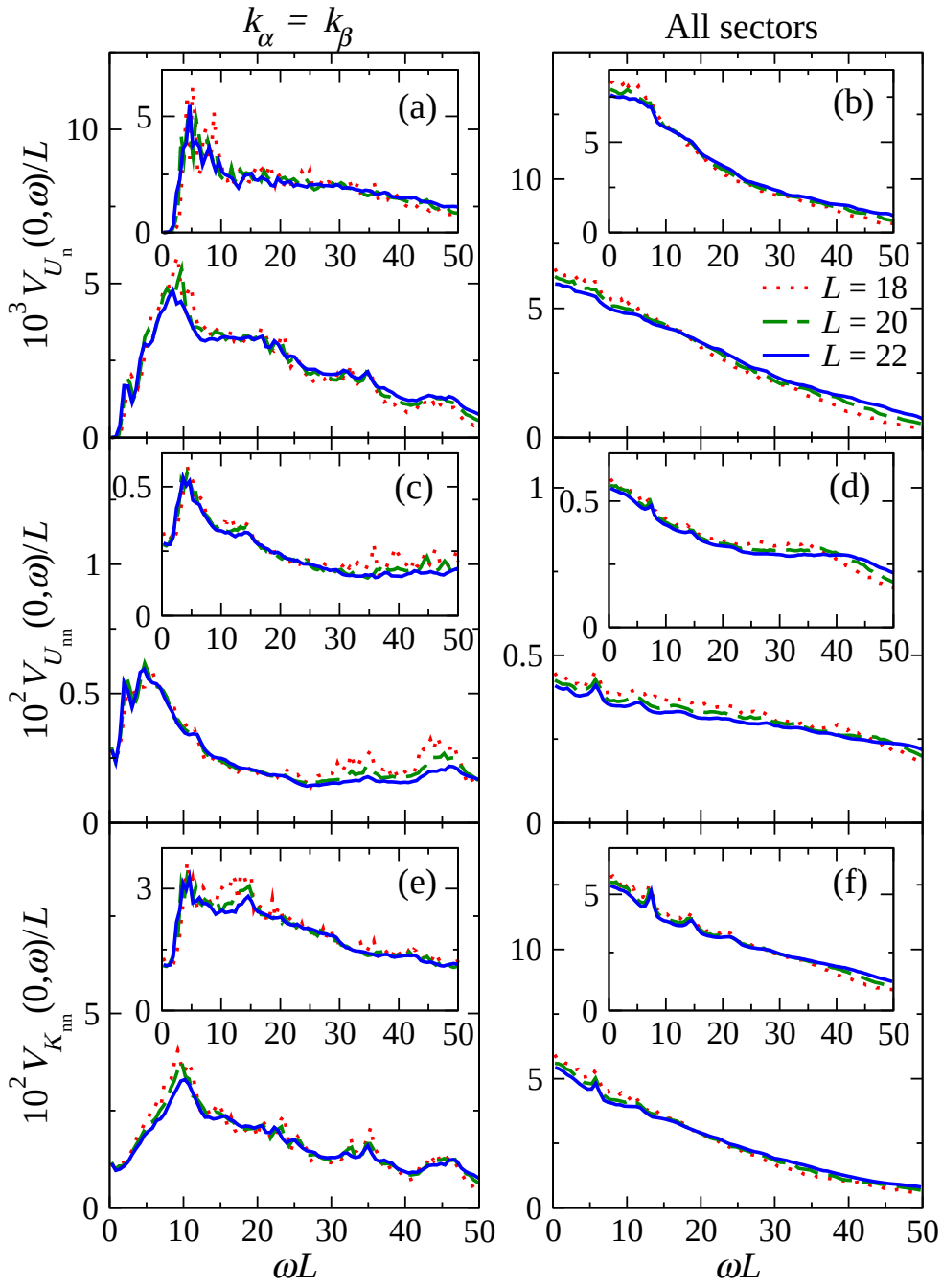

Figure 4.12 | **Low-frequency plots of the scaled variances $V_O(0,\omega)/L$ vs ωL.** We consider observables $\hat{U}_{\rm n}$ [(a), (b)], $\hat{U}_{\rm nn}$ [(c), (d)], and $\hat{K}_{\rm nn}$ [(e), (f)] in the (integrable) XXZ chain with $\Delta = 0.55$ (main panels) and 1.1 (insets), for different chain sizes L. We consider pairs of energy eigenstates with $k_\alpha = k_\beta$ [(a), (c), (e)] and pairs that mix all quasimomentum sectors [(b), (d), (f)]. All pairs of eigenstates satisfy $|\bar{E}|/L \leq 0.025$. The averages $\overline{|O_{\alpha\beta}|^2}$ were coarse-grained in windows of width $\delta\omega = 0.025$.

In the main panels (insets), we show results for $\Delta = 0.55$ ($\Delta = 1.1$). All plots in Fig. 4.12 exhibit good data collapse. In particular, one can see that the location of small features (e.g., peaks and valleys) does not change for different chain sizes (see also the results in Appendix 4.8). This shows that in the XXZ chain, both in the easy-plane and easy-axis regimes, as well as for both symmetry-preserving and symmetry-breaking observables, there is a robust regime in which the variances $V_O(0,\omega)/L$ exhibit ballistic scalings. Qualitatively similar results were reported in Ref. [131] for the XXZ chain with open boundary conditions. Ballistic scalings of variances have also been observed in quantum-chaotic systems [2, 130]. The collapse of the scaled variances $V_O(0,\omega)/L$ when plotted vs ωL degrades as ω increases and one enters the L independent regime depicted in Fig. 4.11. Characterizing the transition between these two regimes is an interesting problem that should be tackled in future works.

Let us focus first on the behavior of $V_O(0,\omega)/L$ for matrix elements that connect energy eigenstates from the same quasimomentum sectors (symmetry-preserving observables). Comparing the results in Fig. 4.12(a) with those in Figs. 4.12(c) and 4.12(e), one can see that $V_{U_{\rm n}}(0,\omega\to 0)/L$ vanishes while $V_{U_{\rm nn}}(0,\omega\to 0)/L$ and $V_{K_{\rm nn}}(0,\omega\to 0)/L$ converge to a nonzero system-size-independent value (see also the results in Appendix 4.8). This behavior is qualitatively similar to the one reported in Ref. [131] for the XXZ chain with open boundary conditions. There, the scaled variance was found to vanish as $\omega\to 0$ for observables that do not break the integrability of the XXZ chain (as is the case here for $\hat{U}^T_{\rm n}$), while $V_O(0,\omega)/L$ was found to converge to a nonzero system-size-independent value for observables that do (as is the case here for $\hat{U}^T_{\rm nn}$ and $\hat{K}^T_{\rm nn}$). This is consistent with the results from Ref. [42] for frequencies that are exponentially small in system size. However, we must emphasize that the results in Fig. 4.12 and in Ref. [131] are for frequencies that are polynomially small in system size and, as such, involve an average over a rapidly (exponentially) growing number of matrix elements with increasing system size.

An interesting feature in the behavior of $V_O(0,\omega)/L$ in Figs. 4.12(a), 4.12(c), and 4.12(e), for both $\Delta = 0.55$ (main panels) and 1.1 (insets), is that there is a worsening of the data collapse as $\omega\to 0$ (it is difficult to see in the plots because it occurs at small values of ωL). This was also noticed in results reported in Ref. [131]. In Figs. 4.13(a), 4.13(c), and 4.13(e), we replot (using a finer coarse graining) the lowest frequency results from Figs. 4.12(a), 4.12(c), and 4.12(e) but against ωL^2. The excellent data collapse in Figs. 4.13(a), 4.13(c), and 4.13(e) at the lowest frequencies (see also the results in Appendix 4.8) suggests that, no matter whether the XXZ chain is in the easy-plane

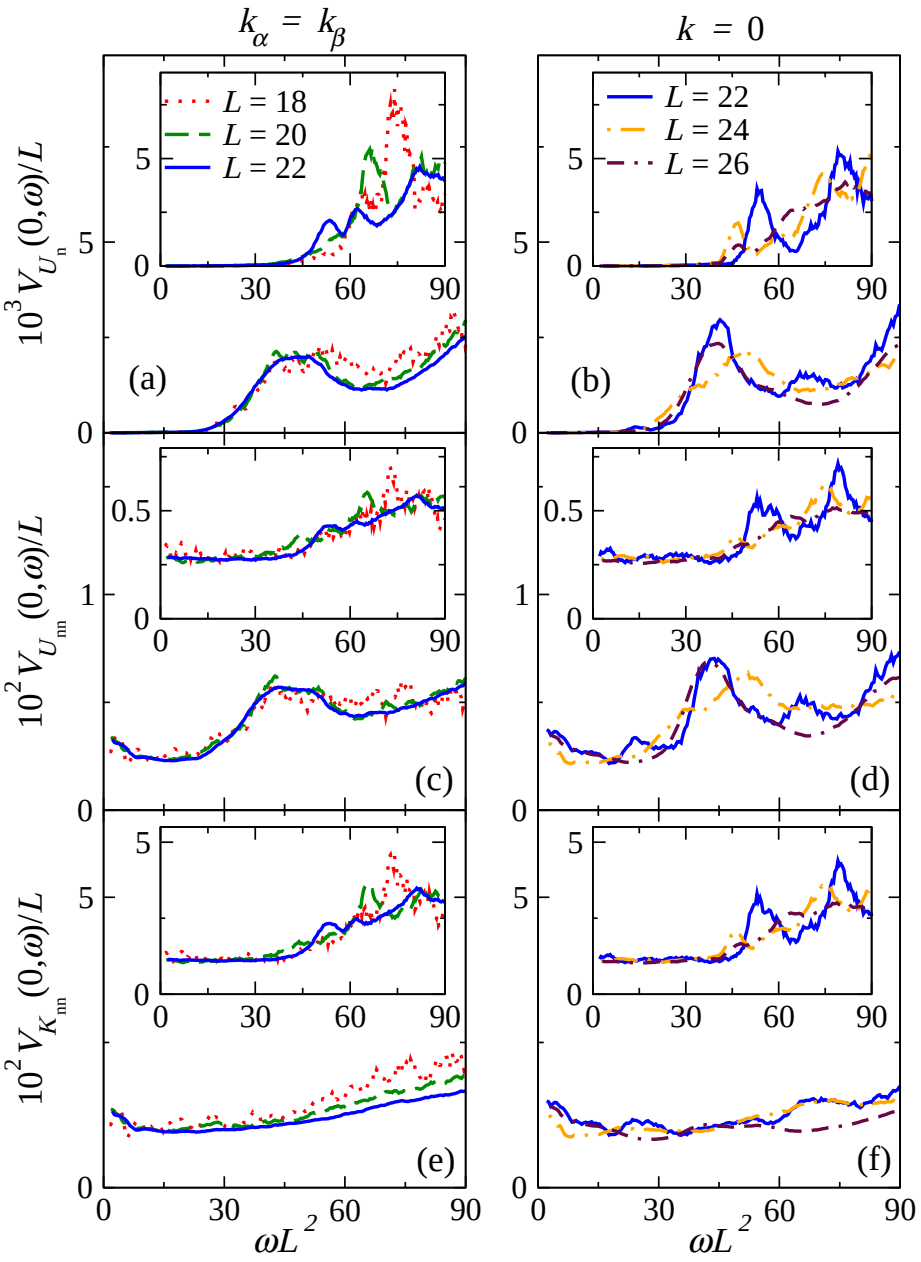

Figure 4.13 | **Low-frequency plots of the scaled variances $V_O(0,\omega)/L$ vs ωL^2 for symmetry-preserving observables.** We consider observables $\hat{U}_{\rm n}$ (a), $\hat{U}_{\rm nn}$ (c), $\hat{K}_{\rm nn}$ (e), and of $V_O^T(0,\omega)/L$ for observables $\hat{U}_{\rm n}^T$ (b), $\hat{U}_{\rm nn}^T$ (d), and $\hat{K}_{\rm nn}^T$ (f), in the XXZ chain with $\Delta = 0.55$ (main panels) and 1.1 (insets), for different chain sizes L. We consider pairs of energy eigenstates with $k_\alpha = k_\beta$ [(a), (c), (e)] and within the even-Z_2, even-P sub-sector of the $k = 0$ sector [(b), (d), (f)]. All pairs of eigenstates satisfy $|\bar{E}|/L \leq 0.025$. The running averages $\overline{|O_{\alpha\beta}|^2}$ were calculated in windows of width $\delta\omega = 0.009$ centered at points separated by $\Delta\omega = 0.001$.

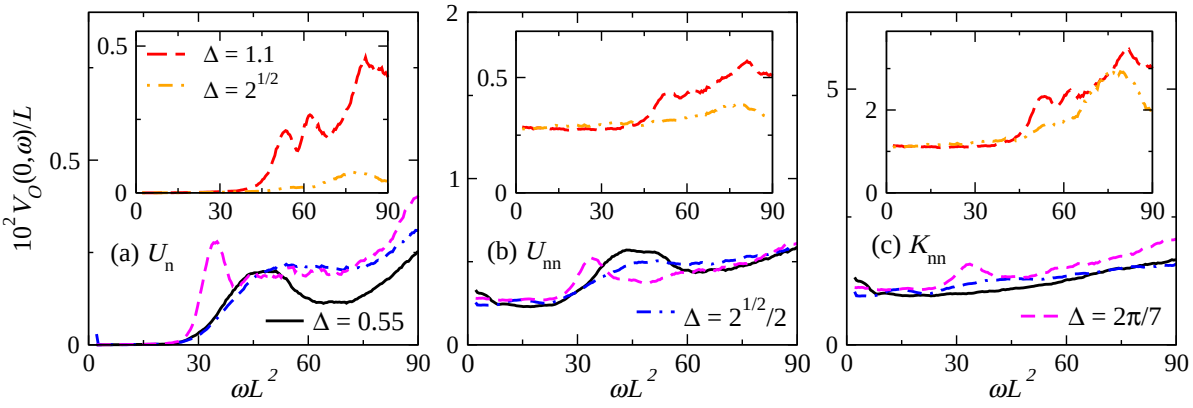

Figure 4.14 | **Comparison of low-frequency behavior of the scaled variances $V_O(0,\omega)/L$ vs ωL^2 for different Δ.** We consider observables $\hat{U}_{\rm n}$ (a), $\hat{U}_{\rm nn}$ (b), and $\hat{K}_{\rm nn}$ (c) in the XXZ chain with Δ in the easy-plane regime ($\Delta < 1$, main panels) and the easy-axis regime ($\Delta > 1$, insets). We consider pairs of energy eigenstates with $k_\alpha = k_\beta$. All pairs of eigenstates satisfy $|\bar{E}|/L \leq 0.025$. The running averages $\overline{|O_{\alpha\beta}|^2}$ were calculated in windows of width $\delta\omega = 0.009$ centered at points separated by $\Delta\omega = 0.001$.

or easy-axis regimes, the variances exhibit diffusive scalings. For completeness, in Figs. 4.13(b), 4.13(d), and 4.13(f), we plot $V_O^T(0,\omega)/L$ vs ωL^2 for $\hat{U}_{\rm n}^T$, $\hat{U}_{\rm nn}^T$, and $\hat{K}_{\rm nn}^T$ in the even-Z_2, even-P subsector of the $k = 0$ sector for chains with up to $L = 26$ for both $\Delta = 0.55$ (main panels) and $\Delta = 1.1$ (insets). The results resemble the ones from Figs. 4.13(a), 4.13(c), and 4.13(e), but exhibit larger finite-size effects, as found in Fig. 4.7 for quantum-chaotic systems.

To further explore the role of Δ in the low-frequency behavior of the scaled variances of symmetry preserving operators, in Fig. 4.14 we plot $V_{U_{\rm n}}(0,\omega)/L$ (a), $V_{U_{\rm nn}}(0,\omega)/L$ (b), and $V_{K_{\rm nn}}(0,\omega)/L$ (c) vs ωL^2 for different values of the anisotropy parameter Δ for lattices with $L = 22$ [2]. The main panels show results in the easy-plane regime, while the insets show results in the easy-axis regime. For $\hat{U}_{\rm n}$, which is the integrability-preserving observable, $V_{U_{\rm n}}(0,\omega \to 0)/L$ vanishes irrespective of Δ. Conversely, for the integrability-breaking observables $\hat{U}_{\rm nn}$ and $\hat{K}_{\rm nn}$, $V_{U_{\rm nn}}(0,\omega \to 0)/L$ and $V_{K_{\rm nn}}(0,\omega \to 0)/L$ do not vanish for any Δ. In the lowest frequency regime for the latter observables, a robust plateau is seen in the scaled variances for $\Delta > 1$, and the results for $\Delta < 1$ are consistent with a plateau. Hence, our results suggest that, as in quantum chaotic systems, diffusion puts the ultimate limit on the equilibration time for integrability-breaking observables in the XXZ chain.

[2]Note that the new values of Δ considered are irrational numbers. Irrational values of Δ help eliminate non-generic features that may appear in the matrix elements because of finite-size effects.

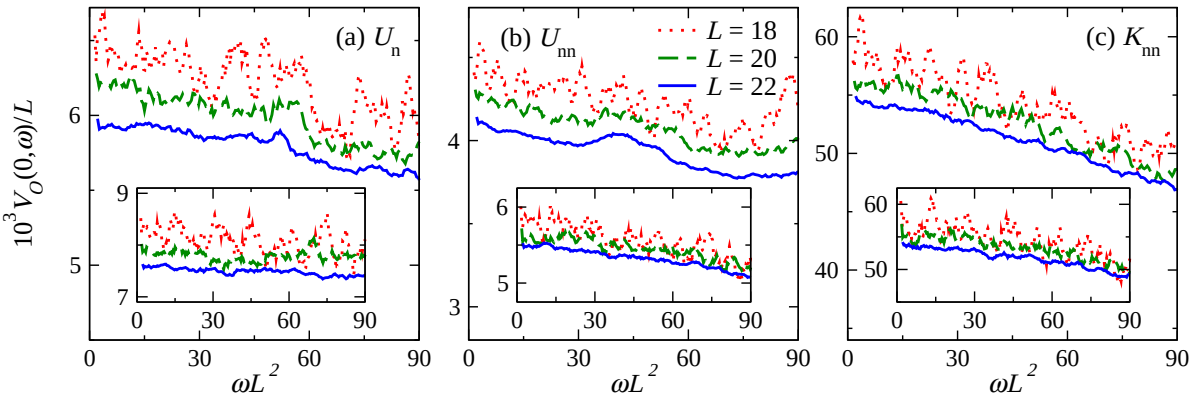

Figure 4.15 | **Low-frequency plots of the scaled variances $V_O(0,\omega)/L$ vs ωL^2 for symmetry-breaking observables.** We consider observables $\hat{U}_{\rm n}$ (a), $\hat{U}_{\rm nn}$ (b), and $\hat{K}_{\rm nn}$ (c), in the XXZ chain with $\Delta = 0.55$ (main panels) and 1.1 (insets), for different chain sizes L. We consider pairs of energy eigenstates that mix all quasimomentum sectors. All pairs of eigenstates satisfy $|\bar{E}|/L \leq 0.025$. The running averages $\overline{|O_{\alpha\beta}|^2}$ were calculated in windows of width $\delta\omega = 0.009$ centered at points separated by $\Delta\omega = 0.001$.

To conclude, let us discuss the behavior of the variances for the operators that break translational symmetry. In Figs. 4.12(b), 4.12(d), and 4.12(f), we show results for $V_O(0,\omega)/L$ vs ωL when averaging over all matrix elements (i.e., for the symmetry-breaking operators). The scaled variances for the three observables, for $\Delta = 0.55$ (main panels) and 1.1 (insets), are all qualitatively similar. The contrast with the results in Figs. 4.12(a), 4.12(c), and 4.12(e) for matrix elements within the same quasimomentum sectors (symmetry-preserving operators) is remarkable. Breaking translational symmetry does not affect the ballistic scaling of the variances but erases many features in $V_O(0,\omega)/L$, especially the vanishing [Fig. 4.12(a)] or the fast decrease [Figs. 4.12(c), and 4.12(e)] seen in $V_O(0,\omega)/L$ as $\omega \to 0$. For all results in Figs. 4.12(b), 4.12(d), and 4.12(f), $V_O(0,\omega \to 0)/L$ is seen to plateau to a (close to) system-size-independent value. Since $\hat{U}_{\rm n}$, $\hat{U}_{\rm nn}$, and $\hat{K}_{\rm nn}$ break the integrability of the XXZ chain if added as perturbations, the observed behavior is consistent with our previous discussion for integrability-breaking observables. In Figs. 4.15(a), 4.15(b), and 4.15(c), we replot (using a finer coarse-graining) the lowest frequency results from Figs. 4.12(b), 4.12(d), and 4.12(f), respectively, but against ωL^2. They are qualitatively similar to the results shown in Fig. 4.6 for quantum chaotic systems. As in Fig. 4.6, larger finite-size effects for the symmetry-breaking observables appear to disrupt the expected scaling for the magnitude of the variance.

4.5 Summary and Discussion

We studied the off-diagonal matrix elements of observables that break translational symmetry in eigenstates of translationally invariant Hamiltonians. In contrast to translationally invariant observables, the matrix elements of the observables considered here connect sectors with different total quasimomentum. We probed properties of the matrix elements in a quantum-chaotic Hamiltonian, as well as in an interacting integrable one (the XXZ chain).

In the quantum-chaotic model, we found that the qualitative behavior of the off-diagonal matrix elements is unaffected by the block diagonal structure of the Hamiltonian in quasimomentum space. Namely, they exhibit all the properties prescribed by the ETH for pairs of eigenstates that mix quasimomentum sectors and pairs of eigenstates that do not. Also, the scaled variances $|f_O(\bar{E},\omega)|^2$ exhibit the expected diffusive scaling in both sets of matrix elements as $\omega \to 0$. We do find that there are quantitative differences between matrix elements that mix or do not mix quasimomentum sectors; specifically, the scaled variances were found to be generally different, and finite-size effects appear to be stronger in the ones that mix quasimomentum sectors.

A much richer behavior was found in interacting integrable models. While the main findings of Ref. [45] for translationally invariant observables still apply to observables that break translational symmetry, namely that the off-diagonal matrix elements exhibit skewed log-normal-like distributions and the scaled variances $V_O(\bar{E},\omega)$ are well-defined smooth functions, new behaviors were found for symmetry-breaking operators at low frequencies. Most notably, for the operators that have a translationally invariant counterpart that does not break integrability if added as a perturbation to the Hamiltonian, $V_O(\bar{E},\omega)$ vanishes as $\omega \to 0$ for matrix elements that do not mix quasimomentum sectors while it approaches a nonvanishing value proportional to L for matrix elements that do. For other observables, $V_O(\bar{E},\omega)$ approaches a nonvanishing value proportional to L as $\omega \to 0$ regardless of whether or not the matrix elements mix quasimomentum sectors. However, the low-frequency behavior of $V_O(\bar{E},\omega)$ for those other observables is still clearly different between the two sets of matrix elements. For matrix elements that do not mix quasimomentum sectors, there is a dip at low frequencies in $V_O(\bar{E},\omega)$ that is absent for those that do. The scaled variances in the latter exhibit a behavior that is qualitatively similar to the one seen in quantum chaotic systems.

We also showed that, for the observables studied in the integrable XXZ chain (which do not include the spin current [130]), the lowest frequency scaling of $V_O(\bar{E},\omega)$ is consistent

with being diffusive regardless of whether the chain is in the easy-plane or easy axis regimes. For integrability-breaking observables, our results suggest that diffusion puts the ultimate limit on the equilibration time in the XXZ chain. In addition, we found a robust frequency regime in which the scaling of $V_O(\bar{E}, \omega)$ is ballistic for all observables. These results are complementary to the rich recent literature on the interplay between ballistic, superdiffusive, and diffusive spin transport in the XXZ chain and other lattice models [140–147] (see Ref. [119] for a recent review on this topic).

4.6 Acknowledgements

My contribution to the work presented here was supported by the National Science Foundation under Grant No. PHY-2012145. I carried out the computations on the Roar supercomputer of the Institute for Computational and Data Sciences (ICDS) at Penn State.

4.7 Appendix: Skewed log-normal-like distributions in the XXZ Chain

In order to probe whether the skewness observed in Fig. 4.8 is a finite-size effect or remains in the thermodynamic limit, we consider $P(\ln|O_{\alpha\beta}|)$ to be a more general function of $\ln|O_{\alpha\beta}|$ than just a Gaussian. Specifically, we take

$$P(\ln|O_{\alpha\beta}|) \propto \exp\left[(\ln D) f\left(\frac{\ln|O_{\alpha\beta}|}{\ln D}\right)\right], \tag{4.13}$$

where $f(x)$ is an unknown concave function (quadratic for the log-normal distribution). This form is motivated by studies of multiplicative noise and multifractals in which similar skewed log-normal-like distributions appear [148]. We focus on matrix elements that connect pairs of eigenstates from the same quasimomentum sectors as those are the ones that have been found to exhibit smaller finite-size effects.

In Fig. 4.16 we plot $\ln P(\ln|(K_{\rm nn})_{\alpha\beta}|)/(\ln D)$ as a function of $\ln|(K_{\rm nn})_{\alpha\beta}|/(\ln D)$ for the three largest chain sizes considered in this work. The data collapse observed suggests that $P(\ln|(K_{\rm nn})_{\alpha\beta}|)$ is described by the ansatz (4.13) with an $f(x)$ function that is not quadratic, namely, that $P(\ln|(K_{\rm nn})_{\alpha\beta}|)$ is a skewed log-normal-like distribution in the thermodynamic limit. We defer finding the $f(x)$ function to future studies. Similar

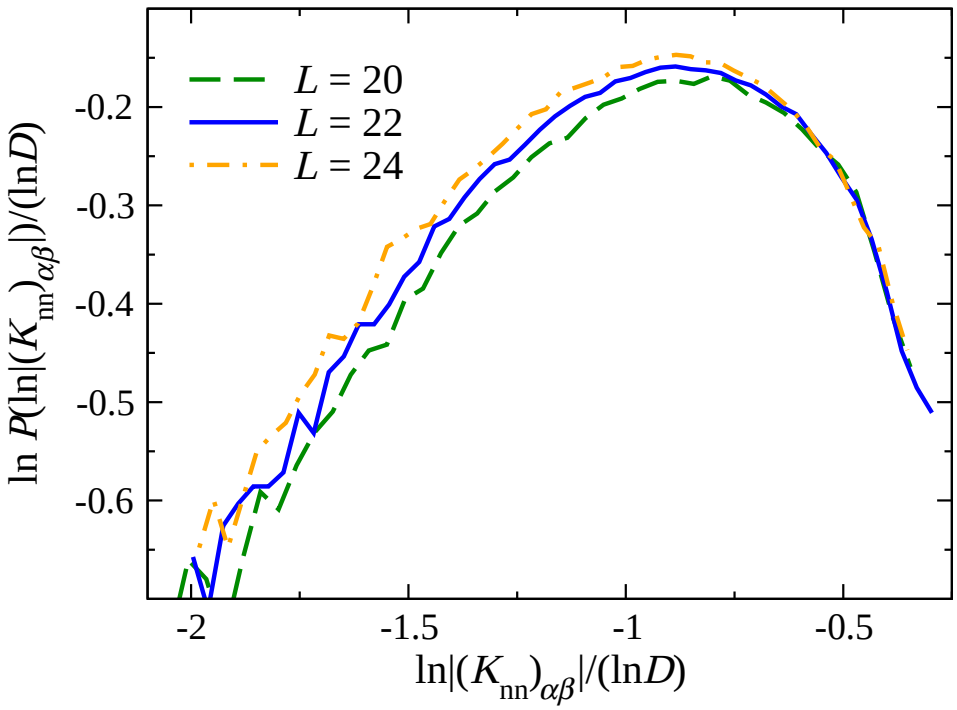

Figure 4.16 | **Probability distributions $P(\ln|(K_{\mathbf{nn}})_{\alpha\beta}|)/(\ln D)$ plotted as functions of $\ln|(K_{\mathbf{nn}})_{\alpha\beta}|/(\ln D)$.** We consider XXZ chains with $\Delta = 0.55$ and $L = 20$, 22, and 24. We show results for matrix elements with $k_\alpha = k_\beta$ selected as explained in Fig. 4.8.

results were obtained for the other integrability-breaking observable $\hat{U}_{\rm nn}$ which, like $\hat{K}_{\rm nn}$, has a well defined plateau at low frequency in which the scaled variance $V_O(\bar{E},\omega)$ is nonvanishing.

4.8 Appendix: Ballistic vs Diffusive Scalings in the XXZ Chain

Here we show the low-frequency behavior of the scaled variances $V_{U_{\rm n}}(0,\omega)/L$ [Figs. 4.17(a) and 4.17(b)] and $V_{K_{\rm nn}}(0,\omega)/L$ [Fig. 4.17(c) and 4.17(d)] plotted vs ωL [Figs. 4.17(a) and 4.17(c)] and vs ωL^2 [Figs. 4.17(b) and 4.17(d)] side-by-side for the two largest (integrable) XXZ chains studied ($L = 22$ and $L = 24$). The main panels show results for $\Delta = 0.55$ while the insets show results for $\Delta = 1.1$. Figure 4.17 makes apparent that the data collapses discussed in the main text improve with increasing chain size. Also, plotting only two chain sizes in Fig. 4.17 allows one to better see the level of detail at which the data collapses occur, including the various features in the scaled variances whose location remains system-size independent in the plots vs ωL and vs ωL^2.

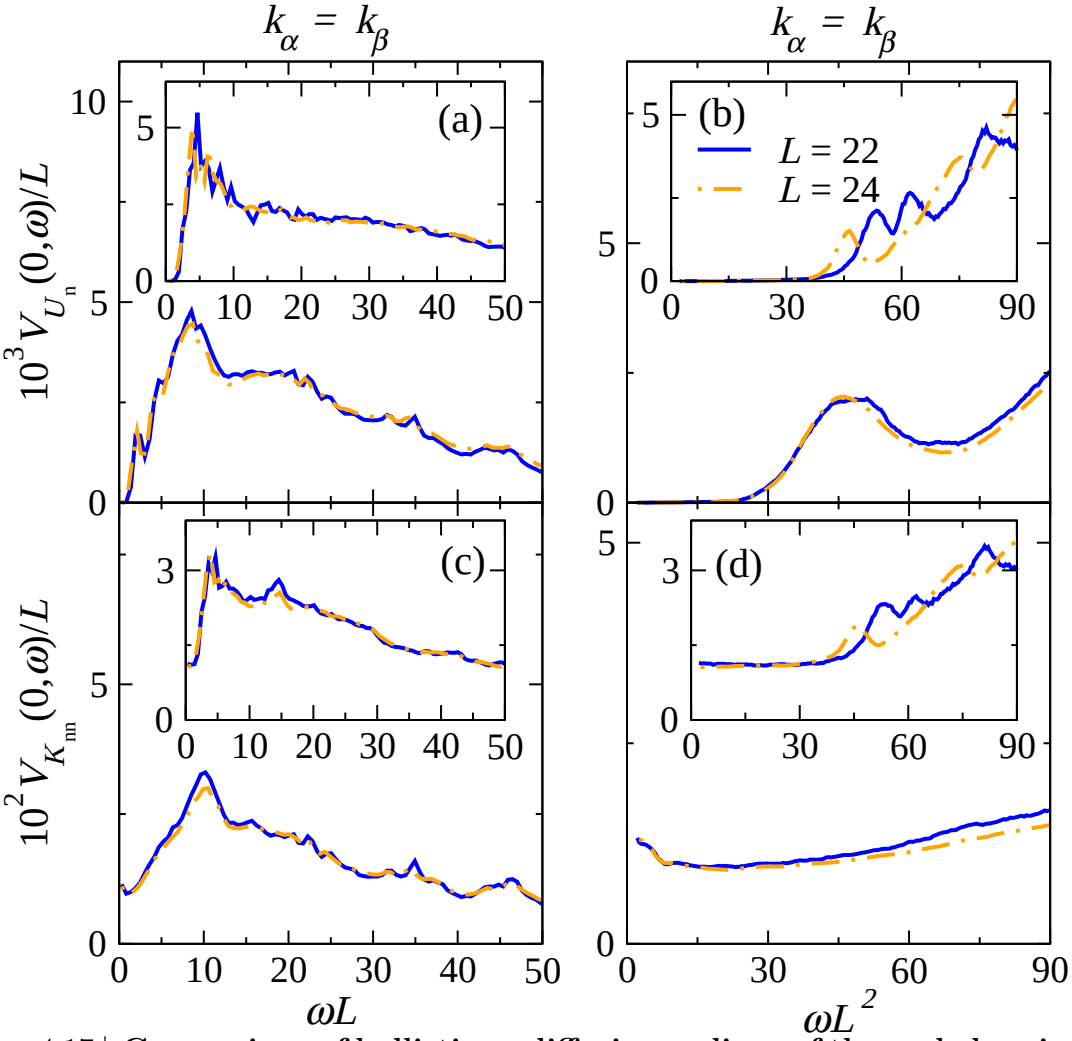

Figure 4.17 | **Comparison of ballistic vs diffusive scalings of the scaled variances.** Low-frequency plots of the scaled variances $V_O(0,\omega)/L$ vs ωL [(a), (c)] and vs ωL^2 [(b), (d)] for observables $\hat{U}_{\rm n}$ [(a), (b)] and $\hat{K}_{\rm nn}$ [(c), (d)] in the integrable XXZ chain with $\Delta = 0.55$ (main panels) and 1.1 (insets). The results are for the two largest chain sizes studied ($L = 22$ and 24) for matrix elements between pairs of energy eigenstates with $k_\alpha = k_\beta$. All pairs of eigenstates satisfy $|\bar{E}|/L \leq 0.025$. The averages $\overline{|O_{\alpha\beta}|^2}$ in (a) and (c) were coarse-grained in windows of width $\delta\omega = 0.025$. The running averages $\overline{|O_{\alpha\beta}|^2}$ in (b) and (d) were calculated in windows of width $\delta\omega = 0.009$ centered at points separated by $\Delta\omega = 0.001$.

Chapter 5
Universality in the Onset of Quantum Chaos in Many-Body Systems

5.1 Introduction

Quantum chaos and eigenstate thermalization are two intertwined fields that have been the focus of much recent attention in the context of the emergence of statistical mechanics and thermodynamics in isolated quantum systems [2, 128, 149]. Those two fields are built on foundational analytical and computational results [13, 17, 24, 64, 65, 150–155], and they have been recently linked to typicality ideas that date back to von Neumann's work [121, 156, 157]. When quantum chaotic systems (which are expected to exhibit eigenstate thermalization) are taken far from equilibrium, few-body operators (observables) generically equilibrate under unitary dynamics to the predictions of traditional statistical mechanics (they "thermalize"). This has been verified in experiments with ultracold quantum gases [9–12]. The "nonthermalizing" counterpart to quantum chaotic systems are integrable [51, 52, 55, 56, 59] and disorder-localized [59,158–160] systems, which have also been probed in experiments with ultracold quantum gases [6–9, 161–163].

In the clean case, a deeper understanding of what happens when quantum chaotic systems approach integrable points is still needed. In finite systems there is a crossover in which quantum chaos [28, 36, 37, 42, 105, 164–166] and eigenstate thermalization [26–28, 36, 37] indicators worsen. In the thermodynamic limit one expects quantum chaos and eigenstate thermalization to break down only at the integrable point [28, 36, 37, 42, 105, 164–166],

but the time scale for thermalization to diverge as one approaches that point. The latter has been seen in recent experiments [9] and numerical experiments [167], and can be understood in the context of Fermi's golden rule [168] and of the scaling of the quantum metric tensor with system size [42]. In the disorder-localized case, localization was argued to be perturbatively stable against weak short-range interactions [169, 170] and against strong interactions in one-dimension (1D) [19]. Disorder-induced localization in interacting systems is known as many-body localization and has attracted much theoretical and experimental research in the strongly interacting regime [59, 158–160]. Recent works have discussed the possible absence of localization in that regime in the thermodynamic limit [171–175].

We explore the onset of quantum chaos at infinite temperature in perturbed integrable and noninteracting disorder-localized chains, as well as its destruction upon approaching trivial classical limits. Our goal is to identify universal features and differences between the clean and disordered cases. We compute fidelity susceptibilities χ, which are equivalent to the diagonal components of the quantum geometric tensor [176, 177] or the norm of the adiabatic gauge potential [42], and spectral functions. Fidelity susceptibilities are commonly used to detect quantum phase transitions [176–180]. We find that the departure from quantum chaos is characterized by a higher sensitivity of eigenstates to perturbations [42, 132, 174], which results in maxima of the typical fidelity susceptibility that scale with the square of the inverse level spacing. The shifts in the maxima's positions with system size are consistent with, at infinite temperature in the thermodynamic limit, quantum chaos only failing to occur at the integrable, noninteracting disorder-localized, and integrable infinite-interaction (classical) limits.

5.2 Model and Observables

We study the (clean) extended spin-1/2 XXZ chain:

$$\hat{H}_{\text{cln}} = \sum_{i=1}^{L} \left[\frac{J}{2} \left(\hat{S}_i^+ \hat{S}_{i+1}^- + \text{H.c.} \right) + \Delta \hat{S}_i^z \hat{S}_{i+1}^z + \Delta' \hat{S}_i^z \hat{S}_{i+2}^z \right], \tag{5.1}$$

with $J = \sqrt{2}$, $\Delta = (\sqrt{5}+1)/4$, and $\Delta' \in [10^{-4}, 10^{1}]$. $\hat{H}_{\text{cln}}$ is Bethe-ansatz integrable for $\Delta' = 0$, and corresponds to two disconnected Ising chains for $\Delta' = \infty$. We also study the Anderson chain with added nearest neighbor interactions, which we write in the spin

language as

$$\hat{H}_{\rm dsr} = \sum_{i=1}^{L} \left[\frac{J}{2} \left(\hat{S}_i^+ \hat{S}_{i+1}^- + \text{H.c.} \right) + h_i \hat{S}_i^z + \Delta \hat{S}_i^z \hat{S}_{i+1}^z \right], \tag{5.2}$$

with $J = \sqrt{2}$, h_i uniformly distributed in $[-h, h]$ with $h = (\sqrt{5}+1)/4$, and $\Delta \in [10^{-3}, 10^{1}]$. $\hat{H}_{\rm dsr}$ is the Anderson model for $\Delta = 0$, and the Ising chain for $\Delta = \infty$.

To probe the eigenkets $|n\rangle$ of the models above, we compute the typical fidelity susceptibility $\chi_{\rm typ}(O) = \exp(\overline{\ln[\chi_n(O)]})$ (in short, the susceptibility) associated to observable $\hat{O}$, where

$$\chi_n(O) = L \sum_{m \neq n} \frac{|\langle n|\hat{O}|m\rangle|^2}{(E_n - E_m)^2}. \tag{5.3}$$

The average $\overline{\ln[\chi_n(\hat{O})]}$ is carried out over the central 50% of eigenstates in the spectrum. We also compute the average spectral function $|f_O(\omega)|^2 = \overline{|f_n^O(\omega)|^2}$ over the same 50% of eigenstates, where

$$|f_n^O(\omega)|^2 = L \sum_{m \neq n} |\langle n|\hat{O}|m\rangle|^2 \delta(\omega - \omega_{nm}). \tag{5.4}$$

We replace $\delta(x) \to \mu/[2\pi(x^2 + \mu^2)]$ with $\mu = 0.9\,\omega_{\rm min}$, where $\omega_{\rm min}$ is the minimum level spacing. The factor of L in Eqs. (5.3) and (5.4) accounts for the Hilbert-Schmidt norm of our translationally invariant intensive observables.

The specific observables $\hat{O}$ considered [181] are the nearest neighbor "kinetic" $\hat{K}_{\rm n}$ and interaction $\hat{U}_{\rm n}$ energies:

$$\hat{K}_{\rm n} = \frac{1}{L} \sum_{i=1}^{L} \left(\hat{S}_i^+ \hat{S}_{i+1}^- + \text{H.c.} \right), \quad \hat{U}_{\rm n} = \frac{1}{L} \sum_{i=1}^{L} \hat{S}_i^z \hat{S}_{i+1}^z, \tag{5.5}$$

and the next-nearest neighbor kinetic energy $\hat{K}_{\rm nn}$. As shown recently [42, 46, 131], in integrable systems the response of eigenstates to perturbations depends on whether the perturbations do or do not break integrability. Keeping in mind that if $\hat{U}_{\rm n}$ ($\hat{K}_{\rm nn}$) is added to $\hat{H}_{\rm cln}$ integrability is preserved (destroyed), while if $\hat{K}_{\rm n}$ ($\hat{U}_{\rm n}$) is added to $\hat{H}_{\rm dsr}$ localization is preserved (destroyed), in what follows we show results for $\hat{U}_{\rm n}$ and $\hat{K}_{\rm nn}$ ($\hat{K}_{\rm n}$ and $\hat{U}_{\rm n}$) when studying $\hat{H}_{\rm cln}$ ($\hat{H}_{\rm dsr}$).

5.3 Clean System

In Fig. 5.1 we show $\chi_{\rm typ}$ vs Δ' (strength of the integrability breaking next-nearest neighbor interaction), for $\hat{U}_{\rm n}$ [Fig. 5.1(a)] and $\hat{K}_{\rm nn}$ [Fig. 5.1(b)]. The susceptibilities are scaled as expected for quantum chaotic systems, for which $\chi_{\rm typ} \propto LD^{-1}\omega_H^{-2}$ (ω_H is the mean

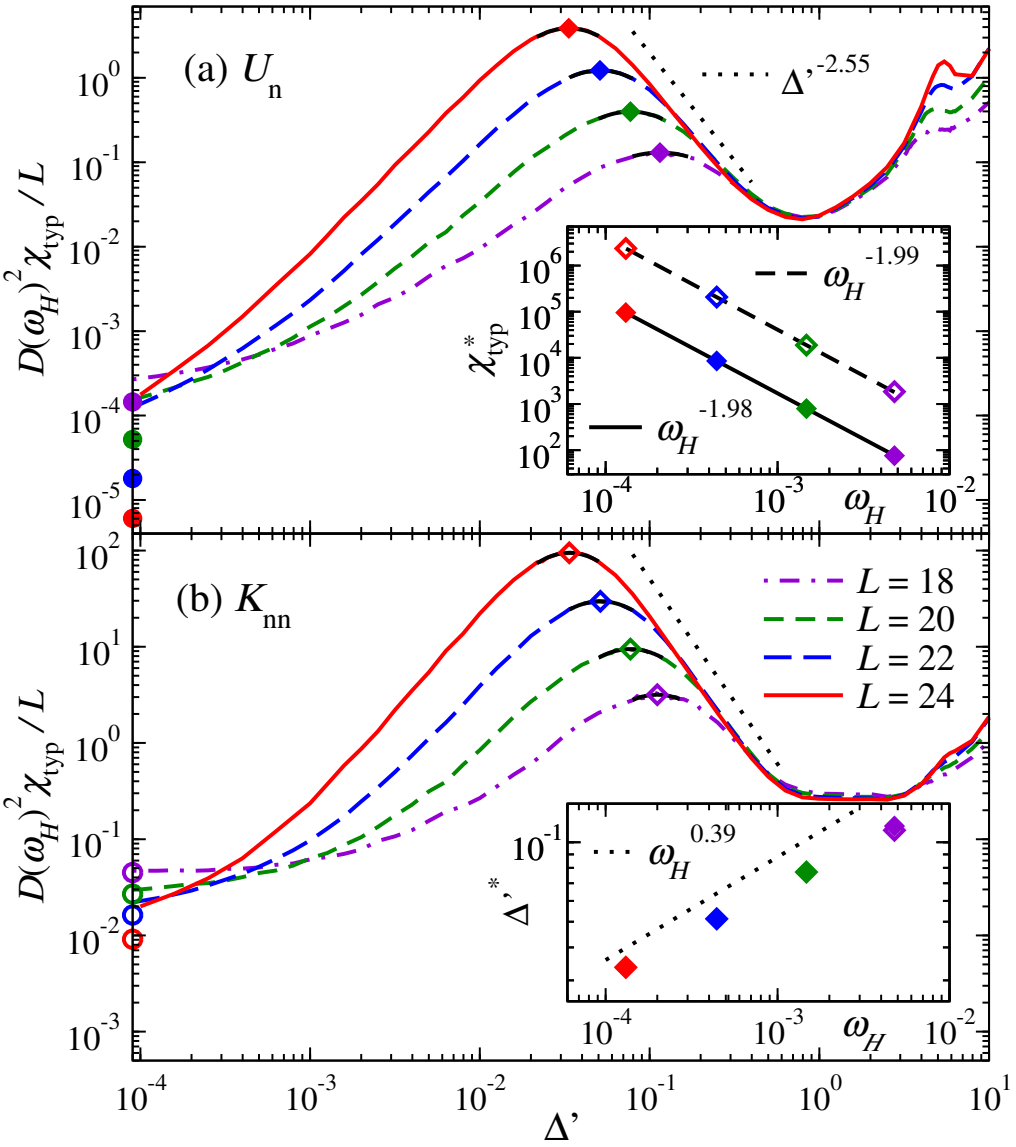

Figure 5.1 | **Typical fidelity susceptibility in clean periodic chains.** Typical fidelity susceptibility χ_{typ} (scaled to exhibit collapse in the quantum chaotic regime) vs the integrability-breaking parameter Δ' for observables $\hat{U}_{\text{n}}$ (a) and $\hat{K}_{\text{nn}}$ (b) in clean periodic chains. To calculate χ_{typ} and ω_H we average over the central 50% of the eigenstates in each total quasimomentum sector considered. For $L < 24$, we report the weighted average over all $k \neq (0, \pi)$ sectors, while for $L = 24$ we report results for the $k = \pi/2$ sector. Circles on the y-axis show χ_{typ} at the integrable point ($\Delta' = 0$), and diamonds show the maximal χ^*_{typ} (at $\Delta'^* = -b/2a$) obtained from polynomial fits $ax^2 + bx + c$ (black solid lines about the maxima). The dotted line on the right of the first peaks depicts $\Delta'^{-2.5}$ behavior. Inset in (a): χ^*_{typ} vs ω_H for both observables, along with the results of power-law fits. Inset in (b): Δ'^* vs ω_H for both observables (the values of Δ'^* overlap). The dotted line depicts $\omega_H^{0.39}$ behavior

level spacing [1]) because $|\langle n|\hat{O}|m\rangle|^2 \propto D^{-1}$ for $E_n - E_m \to \omega_H$ [2,46]. For all chain sizes, the scaled susceptibilities exhibit an excellent collapse for about a decade in Δ' when $\Delta' \sim 1$. The region over which the scaled susceptibilities collapse increases (both towards smaller and larger values of Δ') with increasing system size. This highlights a robust, and increasing with system size, quantum chaotic regime.

The quantum-chaotic regime in Fig. 5.1 is separated from the integrable ones at small and large Δ' by maxima in $\chi_{\rm typ}$ [181]. As a result of the trivial nature of the $\Delta' = \infty$ model, the large-Δ' maxima are more affected by finite-size effects than the small-Δ' ones. In what follows we focus on the latter. The inset in Fig. 5.1(a) shows that $\chi_{\rm typ}$ at the small Δ' maxima scales as the square of the inverse average level spacing ω_H. This scaling corresponds to the maximum possible sensitivity of quantum eigenstates to a perturbation [42]. It is exponentially larger, in system size, than expected from random matrix theory. The position of the maxima, Δ'^*, appears to move towards $\Delta' = 0$ exponentially fast with increasing system size (notice the near equal shift with increasing L and the log scale in the Δ'-axis). In the inset in Fig. 5.1(b), we plot of Δ'^* vs ω_H showing that our numerical results are consistent with $\Delta'^* \propto (\omega_H)^\alpha$, with $\alpha \sim 0.39$. We note that our results in Fig. 5.1 are robust, Δ'^* and the scaling of $\chi^*_{\rm typ}$ are nearly identical for both observables [181].

The susceptibility is related to the spectral function defining the dynamical response of the system [42,177]. Indeed, it follows from Eqs. (5.3) and (5.4) that

$$\chi_n(O) = \int_{-\infty}^{\infty} \frac{|f_n^O(\omega)|^2}{\omega^2} d\omega. \tag{5.6}$$

In integrable systems, $|f_O(\omega \to 0)|^2$ vanishes for integrability preserving perturbations [42, 46, 131, 181], leading to a polynomial in L scaling of $\overline{\chi_n(O)}$ [42]. Typical, integrability breaking, perturbations in contrast have $|f_O(\omega \to 0)|^2 = O(1)$ [42, 46, 131, 181] resulting in exponential in L, $\sim D$ scaling of the susceptibility $\overline{\chi_n(O)}$ [42]. As mentioned before, in quantum chaotic systems $\chi_n(O) \propto L/[D(\omega_H)^2] \sim D$. The faster scaling at the maxima $\chi^*_{\rm typ} \propto 1/\omega_H^2 \sim D^2$ implies that the spectral function diverges as $|f_O(\omega_H)|^2 \sim 1/\omega_H$ around Δ'^*.

Figures 5.2(a) and 5.2(c) show $|f_O(\omega)|^2$ vs ω/Δ' for different values of Δ' about Δ'^* for $L = 24$. The data for both observables collapse at frequencies $\omega/\Delta' \lesssim 1$ showing that $|f_O(\omega)|^2 \sim (\Delta'/\omega)^2$ in that regime [2]. In the top insets, we plot $F_O = (\omega/\Delta')^2 |f_O(\omega)|^2$

[1] For large systems $\omega_H \sim \sqrt{L} D^{-1}$, because the effective width of the many-body energy spectrum is $\propto \sqrt{L}$ (D is the number of energy levels).

[2] The differences in the extent of the $(\Delta'/\omega)^2$ regime is due to the difference in behavior of $|f_O(\omega)|^2$

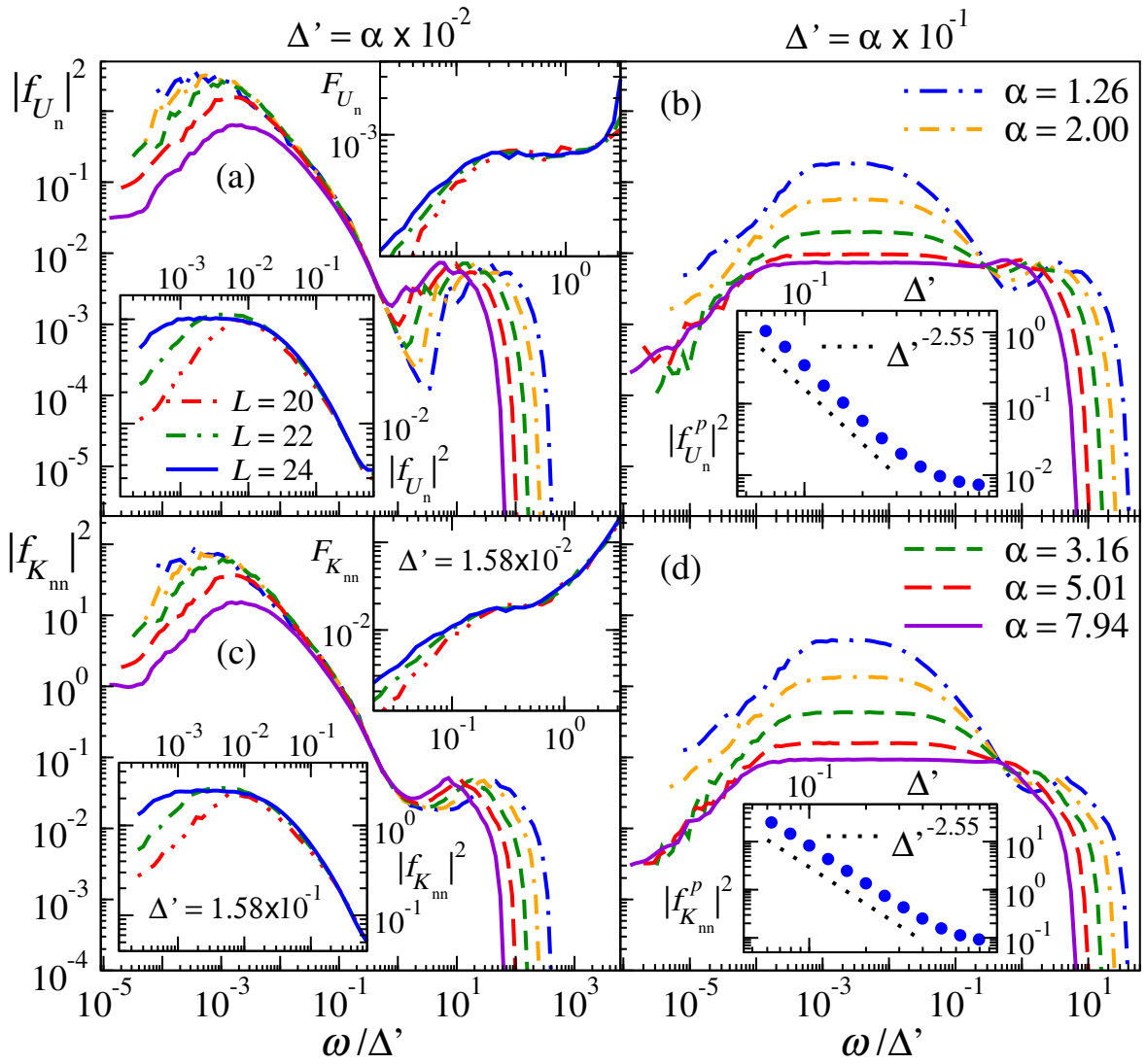

Figure 5.2 | **Spectral functions in clean periodic chains.** Spectral functions in clean periodic chains with $L = 24$ for observables $\hat{U}_{\rm n}$ [(a) and (b)] and $\hat{K}_{\rm nn}$ [(c) and (d)] over two decades of the integrability-breaking parameter Δ' [see labels at the top and legends in (b) and (d)]. In (a) and (c), the top insets show $F_O = (\omega/\Delta')^2|f_O(\omega)|^2$ vs ω/Δ' at $\Delta' = 1.58 \times 10^{-2}$, while the bottom insets show $|f_O(\omega)|^2$ vs ω/Δ' at $\Delta' = 1.58 \times 10^{-1}$, for the three largest chains studied. The insets in (b) and (d) show $|f_O^p(\omega)|^2$ vs Δ', where $|f_O^p(\omega)|^2$ is the value of $|f_O(\omega)|^2$ at the plateaus in the main panels (and for other values of Δ' for which $|f_O(\omega)|^2$ is not shown). The dotted lines depict $\Delta'^{-2.55}$ behavior. All computations were done as for Fig. 5.1.

for different chain sizes when $\Delta' < \Delta'^*$. The plateaus show that the $|f_O(\omega)|^2 \sim (\Delta'/\omega)^2$ behavior is robust to changing L [181]. For $\Delta' < \Delta'^*$, the susceptibilities in Figs. 5.2(a)

for integrability preserving ($\hat{U}_{\rm n}$) vs breaking ($\hat{K}_{\rm nn}$) operators at $\Delta' = 0$, which results in a spectral gap for the former when Δ' is very small.

and 5.2(c) also collapse at lower frequencies showing a nontrivial dependence of ω/Δ' [181], but this collapse gradually disappears as Δ' approaches Δ'^*.

When Δ' increases beyond Δ'^* and the system enters in the quantum chaotic regime [Figs. 5.2(b) and 5.2(d)], a plateau develops in the spectral function at low frequencies [3]. The formation and growth of the plateau with increasing L, at a fixed $\Delta' \gtrsim \Delta'^*$, is illustrated in the bottom insets in Figs. 5.2(a) and 5.2(c). The plateau and the $|f_O(\omega)|^2 \sim (\Delta'/\omega)^2$ behavior coexist in the regime in which $\Delta' \gtrsim \Delta'^*$, which is consistent with the occurrence of thermalization with relaxation rates dictated by Fermi's golden rule [167, 181]. In that regime, we find that the spectral function $|f_O(\omega)|^2$ at the plateau, $|f_O^p|^2$, appears to diverge as $(\Delta')^{-\beta}$ with $\beta \sim 2.55$ [see insets in Figs. 5.2(b) and 5.2(d)], consistent with the divergence of $\chi_{\rm typ}$ in Fig. 5.1 (see dotted lines in the main panels). Remarkably, it is possible to relate the scaling of $|f_O^p|^2$ with Δ' with the drift of Δ'^* with L: $\Delta'^* \sim \omega_H^\alpha$ with $\alpha = 1/\beta \sim 0.39$ [see inset in Fig. 5.1(b)].

We can understand this under the following scenario, let $|f_O(\omega)|^2 = |f_O^p(\Delta')|^2$ for $\omega < \omega_p(\Delta')$ and $|f_O(\omega)|^2 \propto (\omega/\Delta')^{-\kappa}$ for $\omega > \omega_p(\Delta')$, with $\omega_p(\Delta')$ playing the role of the so-called Thouless energy, and $\kappa > 1$. Then from the spectral sum rule: $\int |f_O(\omega)|^2 d\omega = O(1)$, we infer that $\omega_p(\Delta') \propto (\Delta')^\beta$, with $\beta = \kappa/(\kappa - 1)$, and that $|f_O^p(\Delta')|^2 \propto (\Delta')^{-\beta}$. The maximum of $\chi_{\rm typ}$ then occurs when $\omega_p = \omega_H$, i.e., when the maximum of the spectral function occurs at the Heisenberg scale. This results in $\Delta'^* \sim \omega_H^\alpha$ with $\alpha = 1/\beta$, and $\chi^*_{\rm typ} \sim \omega_H^{-2}$. Currently, we do not know the origin of the values of the exponents suggested by our numerical calculations. Given our observation of $|f_O(\omega)|^2 \sim (\Delta'/\omega)^2$ behavior for Δ' below and above Δ'^*, which appears to grow in extent with increasing system size [see top insets in Figs. 5.2(a) and 5.2(c)], two scenarios come to mind: (i) the exponents observed numerically are affected by finite-size effects and for larger systems than those accessible to us $\kappa = 2$, $\beta = 2$, and $\alpha = 1/2$, and (ii) the spectral function develops a power-law with an exponent $1 < \kappa < 2$ before saturating to a constant at low frequencies so that $\beta > 2$ and $\alpha < 1/2$.

5.4 Disordered System

In Fig. 5.3, we show results for the spectral function of disordered chains in the presence of nearest neighbor interactions. The corresponding typical fidelity susceptibilities are shown in Fig. 5.4. The results in Figs. 5.3 and 5.4 are similar to those in Figs. 5.2 and 5.1,

[3] For large L, a diffusive $1/\sqrt{\omega}$ regime is expected to develop at frequencies above those of the plateau [2]

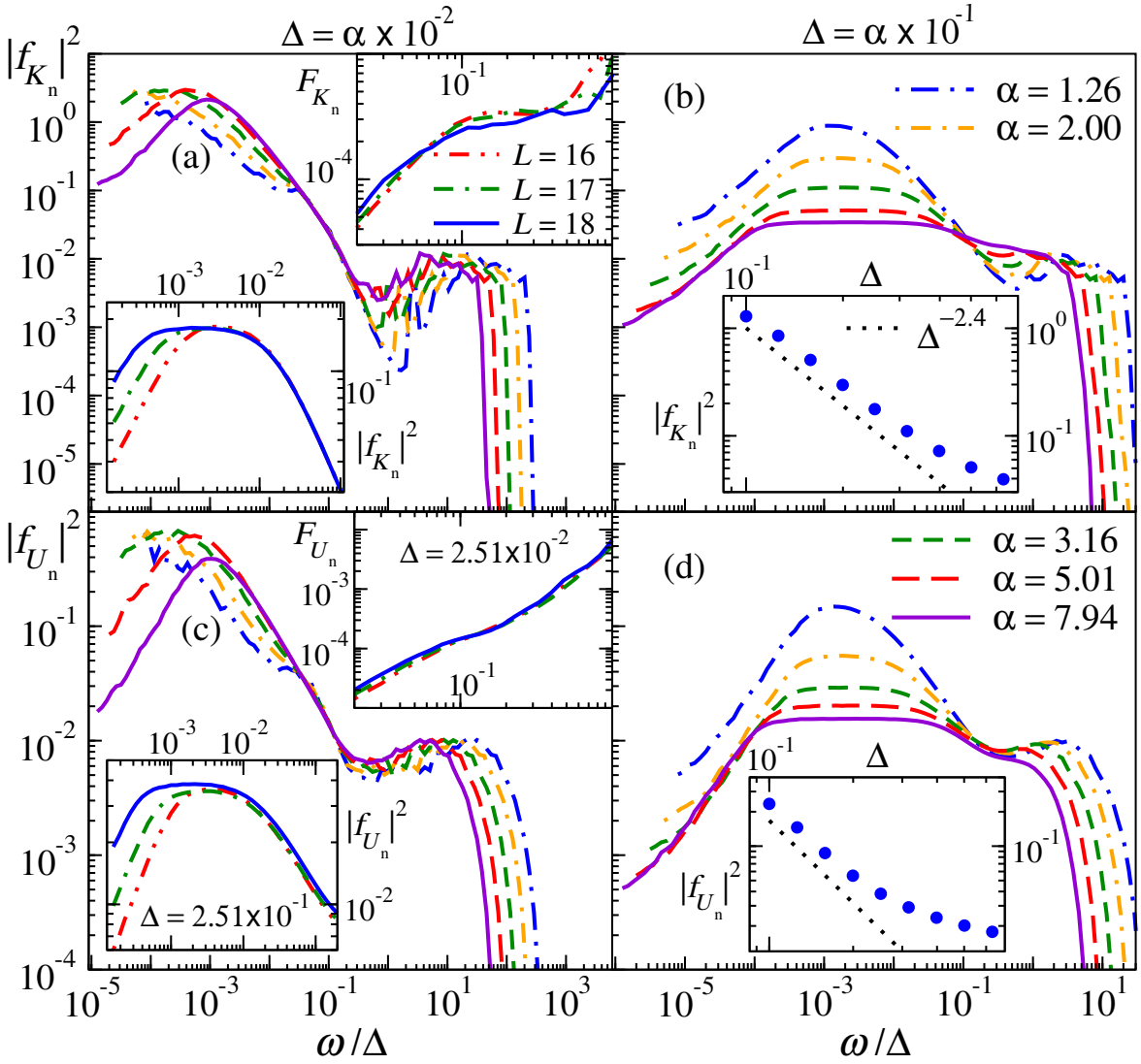

Figure 5.3 | **Spectral functions in disordered periodic chains.** Spectral functions in disordered periodic chains with $L = 18$ for observables $\hat{K}_n$ [(a) and (b)] and $\hat{U}_n$ [(c) and (d)] over two decades of the interaction strength Δ [see labels at the top, and legends in (b) and (d)]. In (a) and (c), the top insets show $F_O = (\omega/\Delta')^2|f_O(\omega)|^2$ vs ω/Δ' at $\Delta' = 2.51 \times 10^{-2}$, while the bottom insets show $|f_O(\omega)|^2$ vs ω/Δ' at $\Delta' = 2.51 \times 10^{-1}$, for the three largest chains studied. The insets in (b) and (d) show $|f_O^p(\omega)|^2$ vs Δ, where $|f_O^p(\omega)|^2$ is the value of $|f_O(\omega)|^2$ at the plateaus in the main panels (and for other values of Δ for which $|f_O(\omega)|^2$ is not shown). The dotted lines depict $\Delta'^{-2.4}$ behavior. To calculate $|f_O(\omega)|^2$, we average over the central 50% of the eigenstates in each chain, and then over disorder realizations (200 for $L \leq 16$, 100 for $L = 17$, and 30 for $L = 18$).

respectively. The similarity is remarkable considering that the unperturbed models in both cases are strikingly different, the disordered one being a noninteracting localized model and the clean one being an interacting integrable one. The slight differences

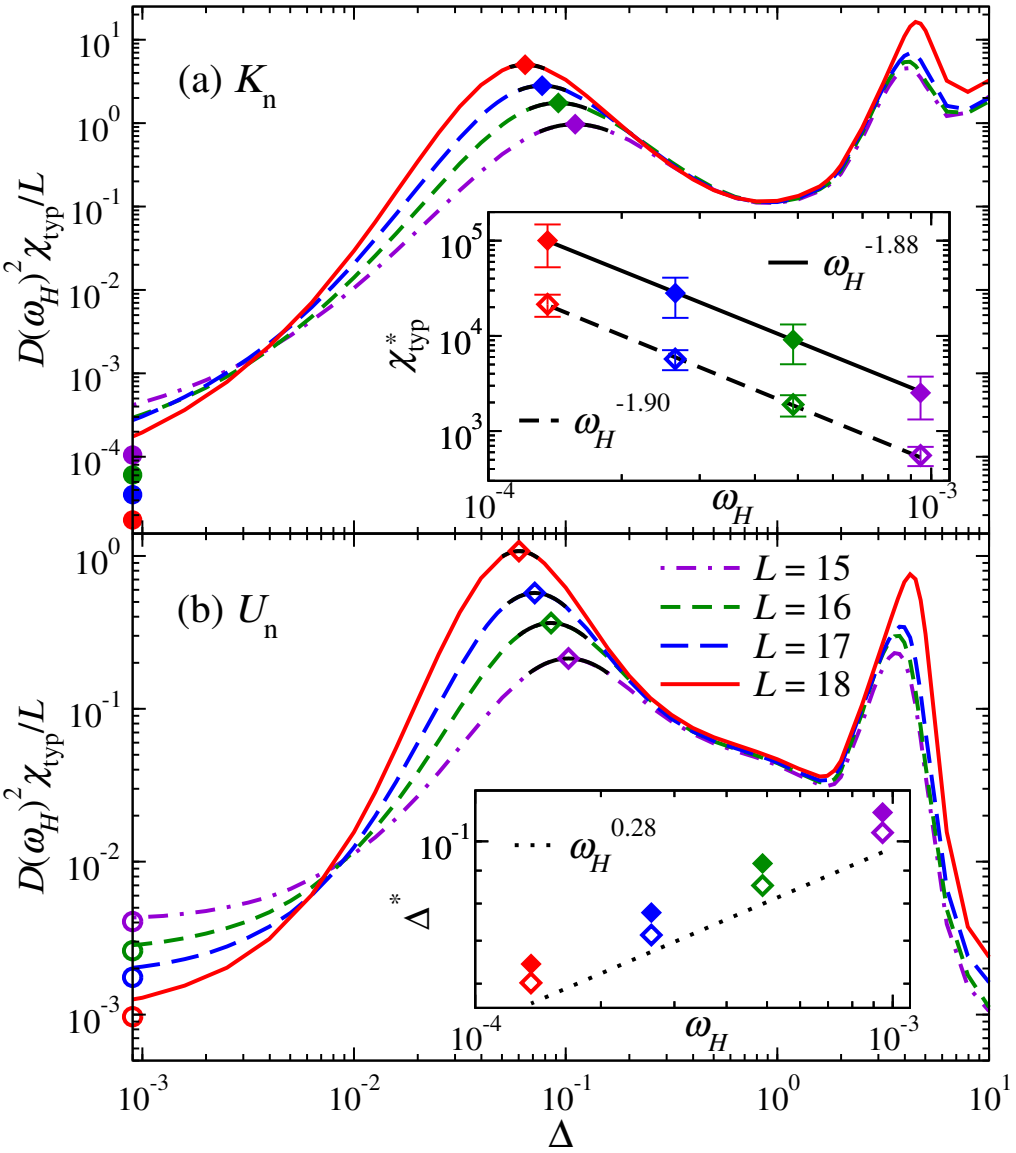

Figure 5.4 | **Typical fidelity susceptibility in disordered periodic chains.** Typical fidelity susceptibility $\chi_{\rm typ}$ (scaled to exhibit collapse in the quantum chaotic regime) vs the interaction strength Δ for observables $\hat{K}_{\rm n}$ (a) and $\hat{U}_{\rm n}$ (b) in disordered periodic chains. Circles on the y-axis show $\chi_{\rm typ}$ at the Anderson-localized point ($\Delta = 0$), and diamonds show the maximal $\chi^*_{\rm typ}$ (at $\delta^* = -b/2a$) obtained from polynomial fits $ax^2 + bx + c$ (black solid lines about the maxima). The inset in (a) shows $\chi^*_{\rm typ}$ vs ω_H for both observables, along with the results of power-law fits. The errorbars show $\pm\sigma$, where σ is the (propagated) standard deviation of the average over disorder realizations at the value of Δ (for which we carried out a calculation) that is closest to Δ^*. The inset in (b) shows Δ^* vs ω_H for both observables. The dotted line depicts $\omega_H^{0.28}$ behavior. All computations were done as for Fig. 5.3.

between the results in Figs. 5.3 and 5.2 include a narrower $|f_O(\omega)|^2 \sim (\Delta'/\omega)^2$ regime in Figs. 5.3(a) and 5.3(c) as compared to Figs. 5.2(a) and 5.2(c), and a narrower regime in which $|f_O^p|^2$ is consistent with a power law scaling with Δ in Fig. 5.3(d). Related to the latter, in the inset in Fig. 5.4(b) the dynamical range for Δ^* vs ω_H is smaller than in the inset in Fig. 5.1(b). Consequently, and also keeping in mind that in Fig. 5.4 we plot typical fidelity susceptibilities while in Fig. 5.3 we plot raw averages of the spectral functions, we cannot establish a relationship between the scaling of $|f_O^p|^2$ with Δ' and the drift of Δ'^* with L as we did for the clean case. That said, all those differences are consistent with stronger finite-size effects, and fluctuations associated to the disorder average, in the disordered systems. For the latter, the largest chains studied have $L = 18$ versus the $L = 24$ chains considered for clean systems.

5.5 Summary

In summary, our results suggest that the onset of quantum chaos at infinite temperature in the models studied, as well as its destruction when approaching classical limits for very strong interactions, is characterized by universal behavior. We focused our analysis on the onset of quantum chaos as finite-size effects (and fluctuations associated to disorder averages) are smaller. The main universal feature identified is the divergence of the typical fidelity susceptibilities as ω_H^{-2} when entering (exiting) the quantum chaotic regime and the associated divergence of the spectral functions below the Thouless energy. The latter is potentially universal, and diverges as $\epsilon^{-\beta}$ (ϵ being either the strength of the integrability or localization-breaking perturbation) in the quantum chaotic regime. Also potentially universal is the shift of the position ϵ^* of the maximum of the fidelity susceptibilities as $\epsilon^* \sim \omega_H^\alpha$, as well as the relation $\alpha = 1/\beta$ between the exponents. We note that while $\epsilon^* \sim \omega_H^\alpha$ supports the expectation that in clean systems in the thermodynamic limit quantum chaos and eigenstate thermalization break down only at the integrable point [28, 36, 37, 42, 105, 164–166], it contradicts the expectation that at infinite temperature the 1D Anderson insulator is stable against adding interactions [160]. Much still needs to be explored, such as what happens at finite temperatures and when one changes the parameters of the unperturbed Hamiltonians (which we selected to be $O(1)$ to minimize finite-size effects). In the disordered case, two parameter regimes to be explored are the strong disorder and strong interaction regimes. The contrast between the small Δ and large Δ peaks in the fidelity susceptibilities in Fig. 5.4 suggest that obtaining meaningful scalings using full exact diagonalization in those regimes will be

computationally very challenging. We note that the results reported in this work required about one million cpu hours of calculations.

5.6 Acknowledgements

My contribution to the work presented here was supported by the National Science Foundation under Grant No. PHY-2012145. I carried out the computations on the Roar supercomputer of the Institute for Computational and Data Sciences (ICDS) at Penn State.

5.7 Appendix: Additional numerical results for clean systems

In Fig. 5.5 we plot $|f_O(\omega)|^2$ vs ω/Δ', for observables $\hat{U}_{\rm n}$ [Fig. 5.5(a)] and $\hat{K}_{\rm nn}$ [Fig. 5.5(b)], at the integrable point for chains with $L = 18$ through $L = 24$. These results show that for the integrability preserving operator ($\hat{U}_{\rm n}$) the spectral function plateaus (as ω approaches ω_H) at a value that decreases exponentially with L, while for the integrability breaking operator ($\hat{K}_{\rm nn}$) the spectral function plateaus at an $O(1)$ value, as found in Ref. [42]. In the insets in Fig. 5.5, the low-frequency data collapse for different values of L show that the spectral function is a function of ωL^2 at low frequencies, as found in Ref. [46].

In Fig. 5.6 we plot $|f_O(\omega)|^2$ vs ω/Δ', for observables $\hat{U}_{\rm n}$ [Fig. 5.6(a)] and $\hat{K}_{\rm nn}$ [Fig. 5.6(b)], when $10^{-3} \leq \Delta' \leq 10^{-2}$ for chains with $L = 24$. These results are the lower Δ' precursors of the results shown in Figs. 2(a) and 2(c) in the main text. The plateaus in the insets make apparent the robust with increasing system size $(\Delta'/\omega)^2$ behavior in the spectral functions for $\Delta' < \Delta'^*$.

In Fig. 5.7, we plot the (scaled) typical fidelity susceptibility for the nearest-neighbor kinetic energy $\hat{K}_{\rm n}$ in clean systems. These results are the equivalent of the ones reported in Fig. 1 of the main text for $\hat{U}_{\rm n}$ and $\hat{K}_{\rm nn}$. The results in Fig. 5.7 are very similar to those in Fig. 1, and are most similar to the ones reported in Fig. 1(a). This is expected as $\hat{K}_{\rm n}$ is an operator that if added as a perturbation to the spin-1/2 XXZ Hamiltonian preserves integrability, like $\hat{U}_{\rm n}$. Hence, the scaling of the typical fidelity susceptibilities is the same for $\hat{K}_{\rm n}$ and $\hat{U}_{\rm n}$ at the unperturbed integrable point.

The right inset in Fig. 5.7 shows that the scaling of $\chi^*_{\rm typ}$ for $\hat{K}_{\rm n}$ is the same as for $\hat{U}_{\rm n}$ and

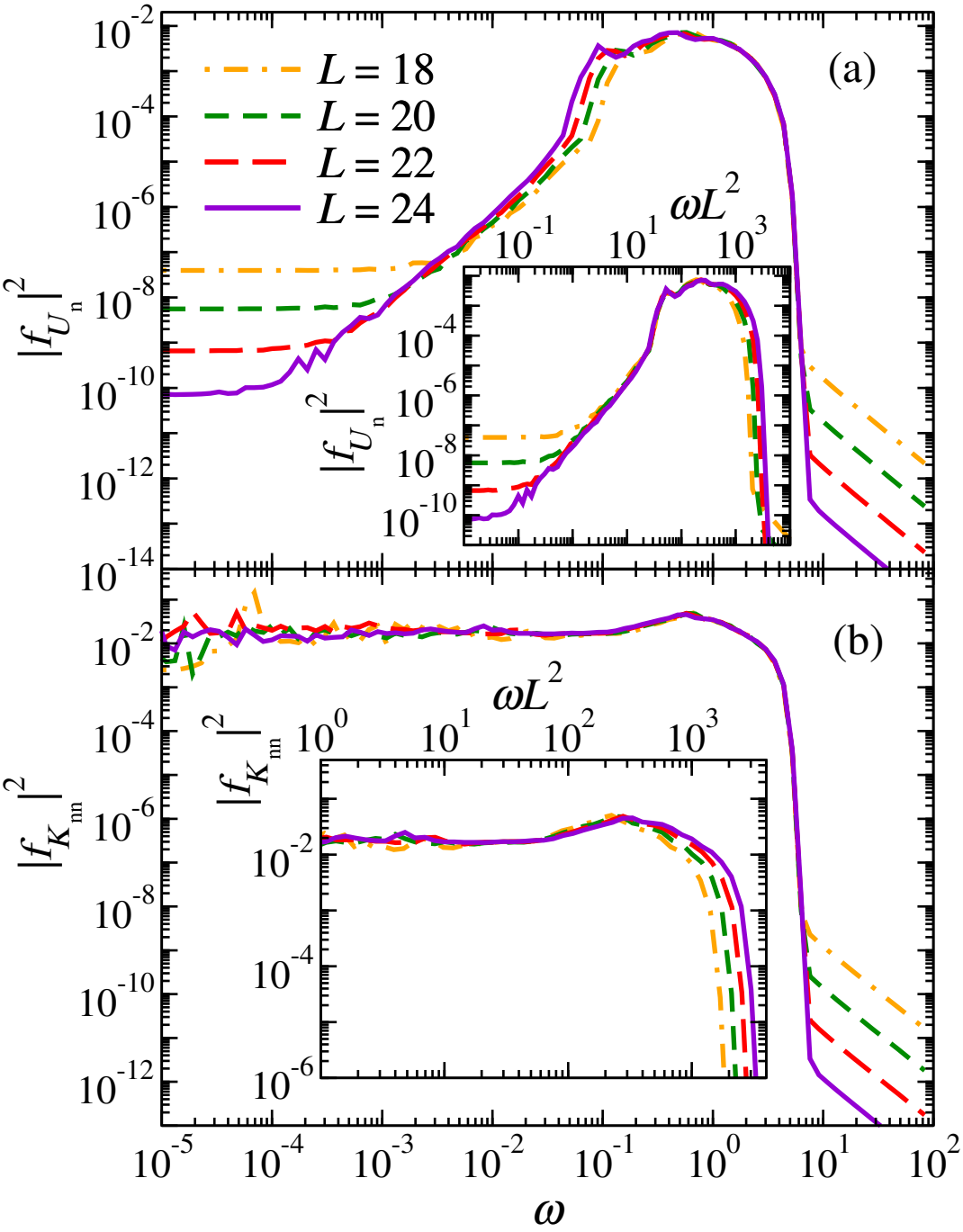

Figure 5.5 | **Spectral functions in clean periodic chains at the integrable point.** Spectral functions in clean periodic chains for observables $\hat{U}_{\rm n}$ (a) and $\hat{K}_{\rm nn}$ (b) at the integrable point $\Delta' = 0$. In our calculations we average over the central 50% of the eigenstates in each total quasimomentum sector considered. For $L < 24$, we report the weighted average over all $k \neq (0, \pi)$ sectors, while for $L = 24$ we report results for the $k = \pi/2$ sector.

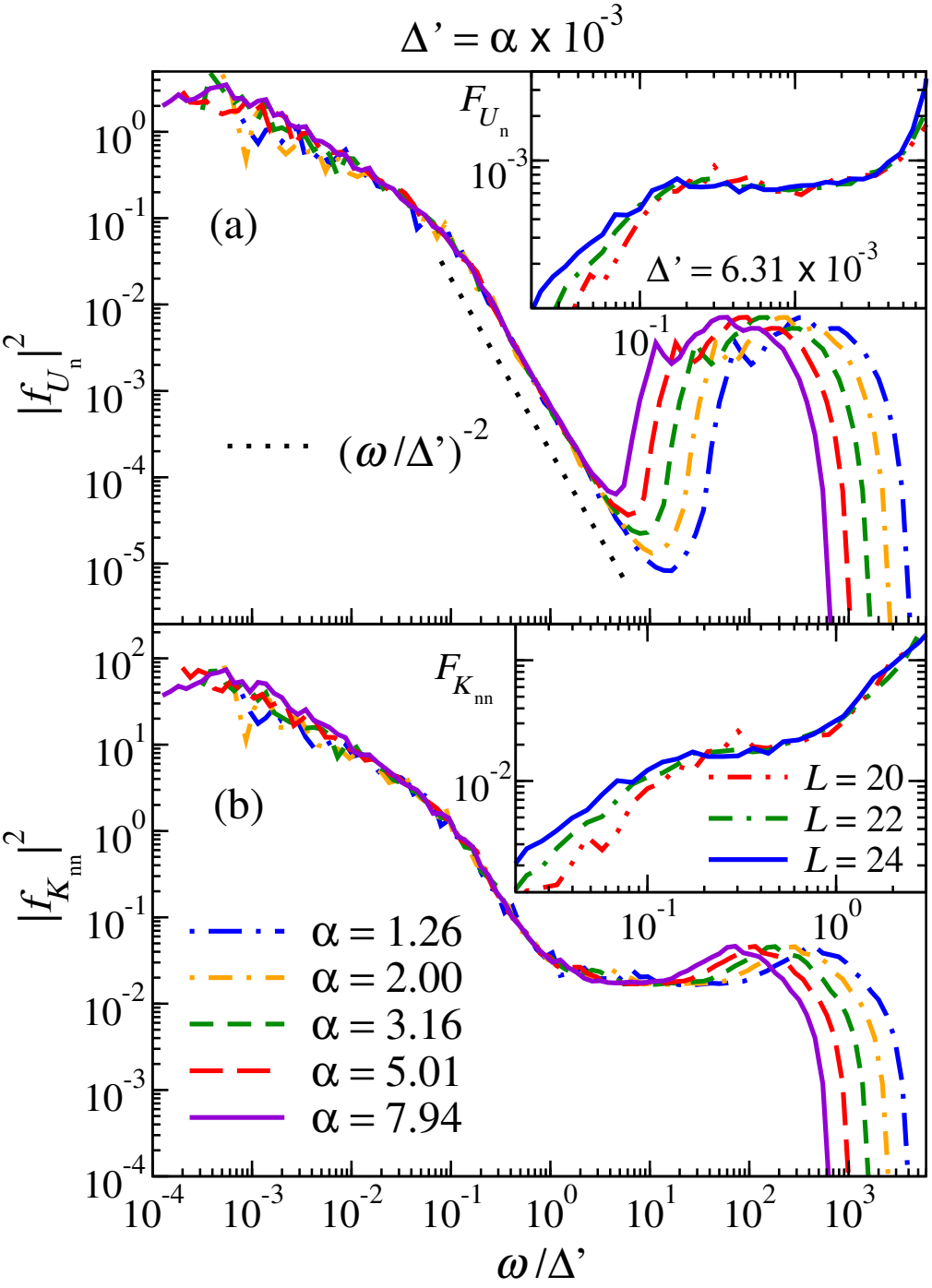

Figure 5.6 | **Spectral functions in clean periodic chains for small perturbation strength.** Spectral functions in clean periodic chains with $L = 24$ for observables $\hat{U}_{\rm n}$ (a) and $\hat{K}_{\rm nn}$ (b) over one decade of the integrability-breaking parameter Δ' [see label at the top and legends in (b)]. The insets show $F_O = (\omega/\Delta')^2|f_O(\omega)|^2$ vs ω/Δ' at $\Delta' = 6.31 \times 10^{-3}$ for the three largest chains studied. All computations were done as for Fig. 5.5.

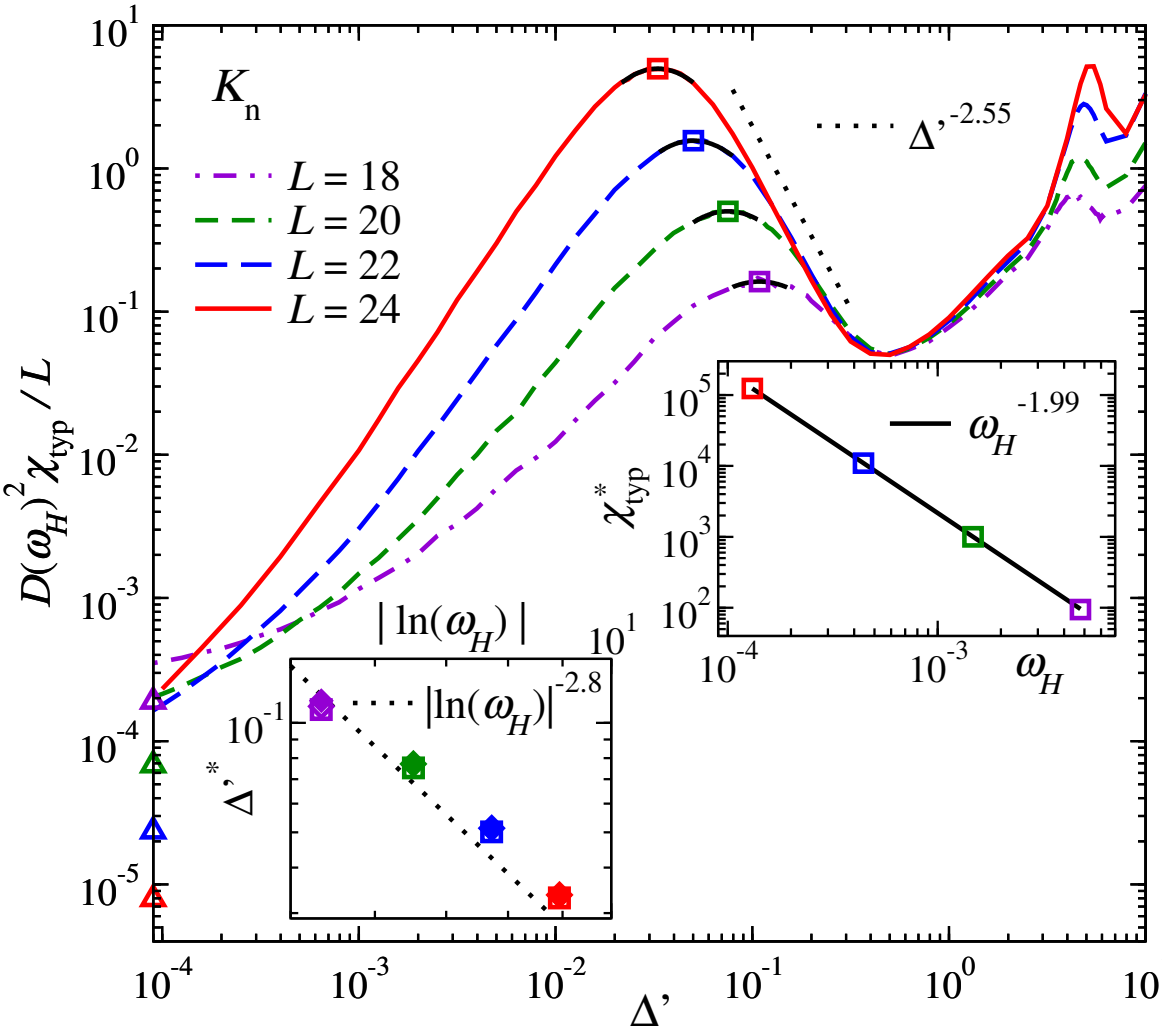

Figure 5.7 | **Typical fidelity susceptibility in clean periodic chains for $\hat{K}_{\mathrm{n}}$.** Typical fidelity susceptibility χ_{typ} (scaled to exhibit collapse in the quantum chaotic regime) vs the integrability-breaking parameter Δ' for $\hat{K}_{\mathrm{n}}$. Triangles on the y-axis show χ_{typ} at the integrable point ($\Delta' = 0$), and squares show the maximal χ^*_{typ} (at $\Delta'^* = -b/2a$) obtained from polynomial fits $ax^2 + bx + c$ (black solid lines about the maxima). The straight dotted line on the right of the first peaks depicts $\Delta'^{-2.5}$ behavior. Right inset: χ^*_{typ} vs ω_H, along with the result of a power-law fit. Left inset: Δ'^* vs $|\ln(\omega_H)|$ for $\hat{K}_{\mathrm{n}}$, $\hat{U}_{\mathrm{n}}$, and $\hat{K}_{\mathrm{nn}}$ (the values of Δ'^* for the three observables overlap). The dotted line depicts $|\ln(\omega_H)|^{-2.8}$ behavior. All computations were done as for Fig. 5.5.

$\hat{K}_{\mathrm{nn}}$ in the main text. The left inset in Fig. 5.7 shows that Δ'^* is less consistent with a polynomial scaling in $\ln(\omega_H)$ (polynomial in L) than with a polynomial scaling in ω_H (exponential in L) as shown in the main text. If it were to be a polynomial scaling in $\ln(\omega_H)$ then the power would be large ($\Delta'^* \sim |\ln(\omega_H)|^{-2.8}$).

5.8 Appendix: Additional numerical results for disordered systems

In Fig. 5.8 we plot $|f_O(\omega)|^2$ vs ω/Δ', for observables $\hat{K}_{\rm n}$ [Fig. 5.5(a)] and $\hat{U}_{\rm n}$ [Fig. 5.5(b)], at the noninteracting point for disordered chains with $L = 15$ through $L = 18$. These results show that for the localization preserving operator ($\hat{K}_{\rm n}$) the spectral function

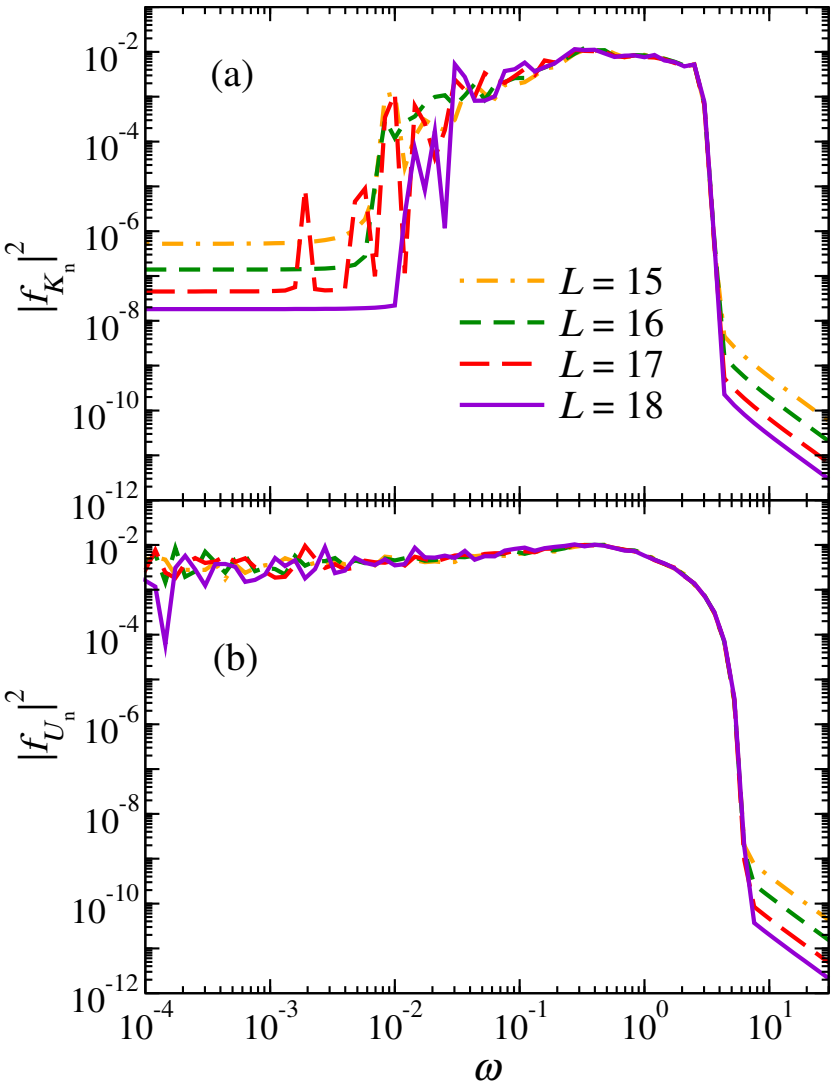

Figure 5.8 | **Spectral functions in disordered periodic chains at the noninteracting point.** Spectral functions in disordered periodic chains for observables $\hat{K}_{\rm n}$ (a), and $\hat{U}_{\rm n}$ (b) at the noninteracting point $\Delta = 0$. To calculate $|f_O(\omega)|^2$, we average over the central 50% of the eigenstates in each chain, and then over disorder realizations (200 for $L \leq 16$, 100 for $L = 17$, and 30 for $L = 18$).

plateaus (as ω approaches ω_H) at a value that decreases exponentially with L while for the localization breaking operator ($\hat{U}_{\rm n}$) the spectral function plateaus at an $O(1)$ value, as in Fig. 5.5 for integrability preserving and breaking operators, respectively.
In Fig. 5.9, we plot the (scaled) typical fidelity susceptibility for the local $\hat{S}^z_i$ operator in disordered systems. These results are the equivalent of the ones reported in Fig. 4 of the main text for $\hat{K}_{\rm n}$ and $\hat{U}_{\rm n}$. The results in Fig. 5.9 are very similar to those in Fig. 4, and are most similar to the ones reported in Fig. 4(a). This is expected as $\hat{S}^z_i$ is an operator that if added as a perturbation to the Anderson chain preserves localization, like $\hat{K}_{\rm n}$.
The right inset in Fig. 5.9 shows that the scaling of $\chi^*_{\rm typ}$ for $\hat{S}^z_i$ is the same as for $\hat{K}_{\rm n}$ and $\hat{U}_{\rm n}$ in the main text. The left inset in Fig. 5.7 shows that Δ'^* is less consistent with a polynomial scaling in $\ln(\omega_H)$ (polynomial in L) than with a polynomial scaling in ω_H (exponential in L) as shown in the main text. If it were to be a polynomial scaling in $\ln(\omega_H)$ then the power would be large ($\Delta'^* \sim |\ln(\omega_H)|^{-2.4}$).

5.9 Appendix: $(\epsilon/\omega)^2$ perturbative scaling and Fermi's golden rule

We use perturbation theory to analyze the spectral function of a weakly perturbed integrable Hamiltonian. Let us assume that the Hamiltonian can be written as

$$\hat{H} = \hat{H}_0 + \epsilon \hat{V}, \tag{5.7}$$

where $\hat{H}_0$ is an integrable Hamiltonian and $\hat{V}$ is the integrability breaking perturbation. For simplicity, we assume that the diagonal matrix elements of $\hat{V}$ in the eigenstates of $\hat{H}_0$ vanish. They produce shifts in the perturbed eigenenergies without affecting the eigenstates, and can be absorbed in the definition of $\hat{H}_0$.
Let us compute the leading perturbative correction to the magnitude of the matrix elements $|\langle n|\hat{O}|m\rangle|^2$ of an arbitrary operator $\hat{O}$ in the perturbed Hamiltonian eigenstates $\{|m\rangle\}$. Expanding

$$O_{nm} \equiv \langle n|\hat{O}|m\rangle = O^{(0)}_{nm} + \epsilon O^{(1)}_{nm} + \dots , \tag{5.8}$$

and applying standard perturbation theory, one finds

$$O^{(1)}_{nm} = -\frac{O_{nn} - O_{mm}}{E^{(0)}_n - E^{(0)}_m} V_{nm} + \sum_{k\neq n,m} \frac{O_{nk}V_{km}}{E^{(0)}_m - E^{(0)}_k} + \frac{V_{nk}O_{km}}{E^{(0)}_n - E^{(0)}_k}, \tag{5.9}$$

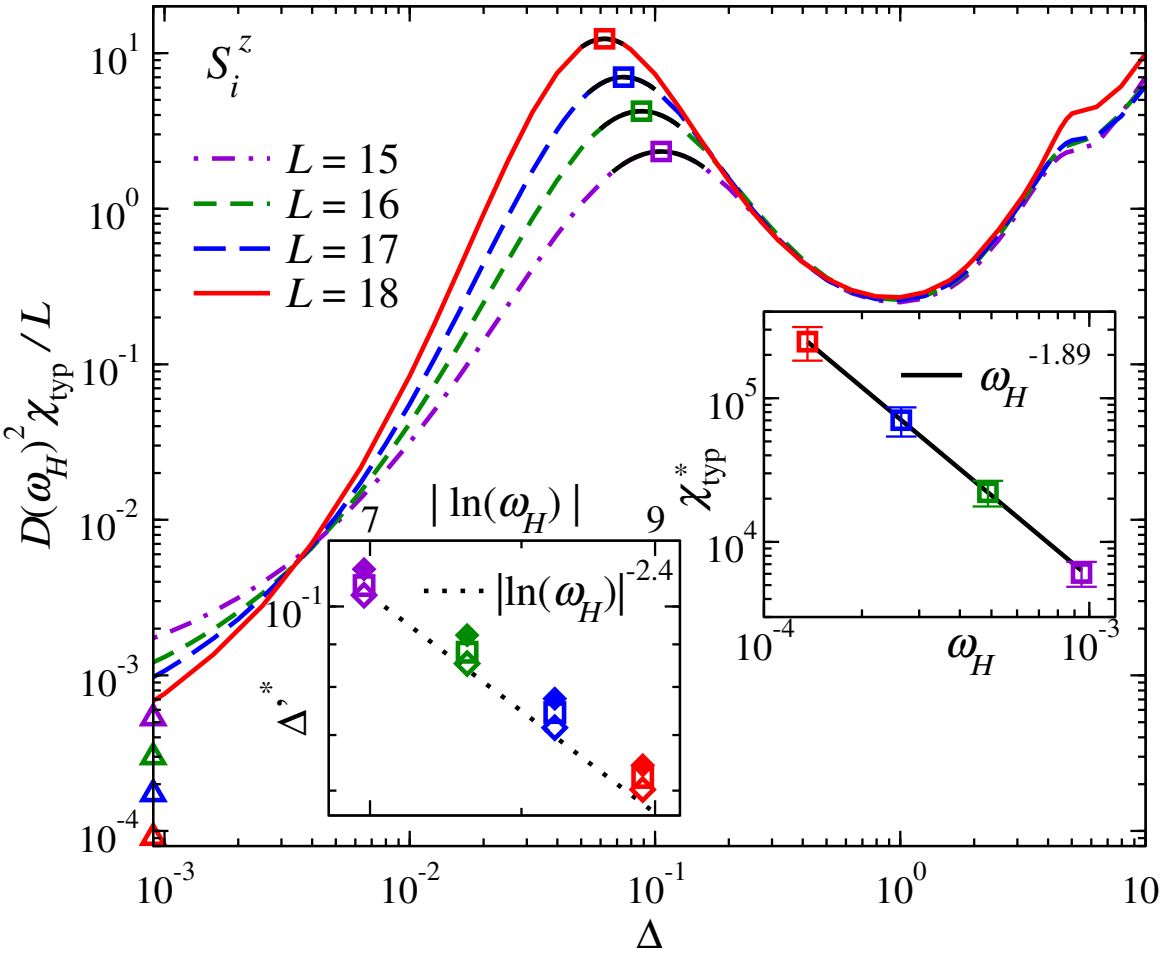

Figure 5.9 | **Typical fidelity susceptibility in disordered periodic chains for $\hat{S}_i^z$.** Typical fidelity susceptibility $\chi_{\rm typ}$ (scaled to exhibit collapse in the quantum chaotic regime) vs the interaction strength Δ for $\hat{S}_i^z$ in disordered periodic chains. Triangles on the y-axis show $\chi_{\rm typ}$ at the Anderson-localized point ($\Delta = 0$), and squares show the maximal $\chi^*_{\rm typ}$ (at $\delta^* = -b/2a$) obtained from polynomial fits $ax^2 + bx + c$ (black solid lines about the maxima). To calculate $\chi_{\rm typ}$, we average over the central 50% of the eigenstates in each chain, over sites, and over disorder realizations (all sites and 200 disorder realizations for $L \leq 16$, 8 sites and 100 disorder realizations for $L = 17$, and 3 sites and 30 disorder realizations for $L = 18$). Right inset: $\chi^*_{\rm typ}$ vs ω_H, along with the result of a power-law fit. The errorbars show $\pm\sigma$, where σ is the (propagated) standard deviation of the average over disorder realizations at the value of Δ (for which we carried out a calculation) closest to Δ^*. Left inset: Δ'^* vs $\ln(\omega_H)$ for $\hat{S}_i^z$, $\hat{K}_{\rm n}$, and $\hat{U}_{\rm n}$. The dotted line depicts $|\ln(\omega_H)|^{-2.4}$ behavior.

where all energies and matrix elements refer to those of the unperturbed integrable Hamiltonian $\hat{H}_0$. We intentionally separated diagonal and off-diagonal contributions in the expression above.

It is straightforward to check that for integrable $\hat{H}_0$ the first (diagonal) term is the most divergent one, because the diagonal matrix elements $O_n \equiv O_{nn}$ and $O_m \equiv O_{mm}$ do not have to be close to each other when the energy difference $\omega_{nm} = E_n - E_m$ becomes of the order of the level spacing, in contrast to what happens in generic systems which exhibit eigenstate thermalization. Therefore, this term is singular. The second (off-diagonal) term [in the second line in Eq. (5.9)] can be divergent as well, but generally it has weaker singularities because even in integrable systems the off-diagonal matrix elements of generic operators are exponentially small in the system size [45]. This second term may play a more prominent role when the unperturbed Hamiltonian is quadratic (as in our disorder-localized systems) because there only a vanishing fraction of off-diagonal matrix elements is nonvanishing so the nonvanishing matrix elements can be large [29]. Hence, we find the most singular perturbative correction to the spectral function $|f_O(\omega)|^2 = \overline{|f_n^O(\omega)|^2}$ (the overline stands for the average over eigenstates), with $|f_n^O(\omega)|^2$ defined in Eq. (4) in the main text, is

$$|f_O(\omega)|^2 - |f_O^{(0)}(\omega)|^2 \approx L\frac{\epsilon^2}{\omega^2}\left[\overline{\sum_m (O_n - O_m)^2 |V_{nm}|^2 \delta(\omega - \omega_{nm})}\right]. \tag{5.10}$$

We note that the linear in ϵ terms vanish because they are linear in the off-diagonal matrix elements O_{mn} and V_{nm}, whose average vanishes [45].

Interestingly Eq. (5.10) can be viewed as the Fermi golden rule (FGR) type Lorentzian broadening of the $\delta(w)$ part of the spectral function in the integrable limit by the perturbation. The FGR was recently shown to apply to weakly perturbed integrable systems under unitary dynamics in the context of quantum quenches [168] and periodic drivings [1]. Indeed for a given state n, LO_n^2 can be viewed as a $\delta(\omega)$ part of the spectral function or the Drude weight [4]. Within the FGR this δ-function broadens to a Lorentzian resulting in:

$$|f_n^O(\omega)|^2 \approx |f_{n,0}^O(\omega)|^2 + O_n^2 \frac{L}{\pi} \frac{\Gamma_n(\omega)}{\omega^2 + \Gamma_n^2(\omega)}, \tag{5.11}$$

where $|f_{n,0}^O(\omega)|^2$ is the spectral function in the integrable limit (not including the Drude weight). This shape of the spectral function was recently numerically observed on a different model [182].

Comparing Eqs. (5.11) and (5.10), we see that they are consistent if we set

$$\Gamma_n(\omega) = \pi\epsilon^2 \sum_m \left(1 - \frac{O_m}{O_n}\right)^2 |V_{nm}|^2 \delta(\omega - \omega_{nm}). \tag{5.12}$$

[4] We assume that the microcanonical average of $\hat{O}$ is zero, otherwise it should be subtracted from O_n

The rate $\Gamma_n(\omega)$ is nothing but the FGR rate of change of the normalized variance of $\hat{O}$ under perturbation $\epsilon\hat{V}\cos[\omega t]$. Indeed, within the FGR

$$\frac{d\,\delta O^2(t)}{dt} \equiv \frac{d(\langle\hat{O}^2(t)\rangle - \langle\hat{O}(t)\rangle^2}{dt} = \pi\epsilon^2\sum_m |V_{nm}|^2(O_n - O_m)^2\delta(\omega - \omega_{nm}). \quad (5.13)$$

Defining the decay rate through

$$\frac{d\,\delta O^2(t)}{dt} = \Gamma_n(\omega)\,O_n^2,$$

we get Eq. (5.12). Let us finally note that, at small frequencies ω, this rate is expected to be independent of ω and thus it can be replaced with the static rate Γ_n obtained in the limit $\omega \to 0$.

Around the maxima in the typical fidelity susceptibilities in Figs. 1 and 4 in the main text, our numerical results in Figs. 2 and 3 in the main text, and in Fig. 5.6, are consistent with the spectral function exhibiting the previously noted $(\epsilon/\omega)^2$ regime. This is a regime in which perturbation theory breaks down at low frequencies, as made apparent in our numerical results by the fact that the low-frequency parts of the spectral functions exhibit a slower than $(\epsilon/\omega)^2$ divergence.

It is important to emphasize that the $(\epsilon/\omega)^2$ regime is in general absent if $\hat{H}_0$ is quantum chaotic and $\hat{V}$ does not break any conservation law. In that case, per the eigenstate thermalization hypothesis, the diagonal matrix elements O_{nn} and O_{mm} are exponentially close (in L) to each other when ω_{nm} approaches the level spacing, and the off-diagonal matrix elements V_{nm} are exponentially suppressed, so that the perturbative correction to the spectral function does not diverge when ω approaches the level spacing. The $(\epsilon/\omega)^2$ regime is also absent if the perturbation $\hat{V}$ preserves the integrability of the unperturbed Hamiltonian $\hat{H}_0$. In that case, the matrix elements V_{nm} have an additional exponential suppression with the system size as ω_{nm} approaches the level spacing, as shown in Fig. 5.5 and in Ref. [42]. As a result, the perturbative correction to the spectral function does not diverge at ω approaches the level spacing.

Chapter 6
Summary

The research presented in this thesis has expanded our understanding of the properties of the matrix elements of observables in interacting integrable systems. Our motivation in doing this research has been to deepen our understanding of the many-body quantum dynamics of those systems. As discussed in Chapter 1, thermalization in quantum chaotic systems is understood on the basis of the eigenstate thermalization hypothesis, which is rooted on random matrix theory. The description of integrable systems after relaxation, on the other hand, is understood on the basis of generalized thermalization, in which an initial state of a system evolving under an integrable Hamiltonian selects eigenstates that have a narrow distribution in all of the conserved quantities of the system. Then, the smoothness of the diagonal matrix elements as a function of all of the conserved quantities results in a generalized Gibbs ensemble description after equilibration.

In Chapter 2, which focuses on Ref. [45], the behavior of the diagonal matrix elements in interacting integrable systems was explored in detail. There, it was demonstrated that the eigenstate-to-eigenstate fluctuations decay as a power law in system size at the center of the spectrum, while they decay exponentially in system size in nonintegrable systems. This shows that the vast majority of eigenstates are thermal in interacting integrable systems in the thermodynamic limit. We also showed that the support of the distribution does not decrease in interacting integrable systems as opposed to its exponential decrease in nonintegrable ones. Therefore, nonthermal eigenstates persist in the thermodynamic limit and they are the ones that disrupt thermalization.

The off-diagonal matrix elements in interacting integrable systems were much less well-understood in the literature preceding Ref. [45] than the diagonal matrix elements were. In Chapter 2, we showed that the off-diagonal matrix elements are dense rather than sparse, and that they obey a nearly log-normal distribution. While in Ref. [45] it was not known whether deviations from log-normality persist in the thermodynamic limit,

our later work (Ref. [46], reproduced in Chapter 4) clarified that they do. Additionally, confirming what was suggested in Ref. [1], we demonstrated in Chapter 2 that the off-diagonal matrix elements of observables in interacting integrable systems have a well-defined variance that scales as in nonintegrable ones. Interestingly, although the off-diagonal elements can be used in a similar fashion as in nonintegrable systems (a scaled variance function $|f(\bar{E},\omega)|^2$ is well-defined and can be probed using heating rates as in Ref. [1]), the distributions have a fundamentally different character than those of nonintegrable systems (which exhibit normal distributions).

In Chapter 2, the average entanglement entropy over eigenstates was also probed and shown to be a powerful tool to distinguish between integrable and quantum chaotic Hamiltonians. While the universal (maximal) volume-law coefficient was confirmed to hold in quantum chaotic systems, a smaller one (consistent with being equal to the one for noninteracting fermions) was found in interacting integrable systems. This, together with what was learned about the off-diagonal matrix elements as noted above, hints at a distinctly different underlying mathematical framework in interacting integrable systems than in quantum chaotic ones. We can understand this to be the case because integrable systems have an underlying quasiparticle description that is fundamentally different from the random matrix theory underlying nonintegrable ones. A question we leave open is how to analytically understand the emergence of a skewed log-normal-like distribution in the off-diagonal matrix elements of interacting integrable systems. On the entanglement entropy side, recent progress has been made via understanding the average entanglement entropy over eigenstates in random quadratic Hamiltonians [183].

In Chapter 4, which is based on Ref. [46], we studied the properties of matrix elements of observables that break translational symmetry in both quantum chaotic and interacting integrable Hamiltonians. These observables connect different total quasimomentum sectors of translationally invariant Hamiltonians. It was found that the underlying block-diagonal structure of the Hamiltonian does not qualitatively impact the properties of the off-diagonal matrix elements of operators in the quantum chaotic case, with the ETH ansatz being obeyed for the distributions of matrix elements that connect quasimomentum sectors and those that do not. A comparison between these two distributions showed that they are quantitatively different, and have different variances, although they share the same qualitative properties. For example, both distributions exhibit diffusive scaling for $\omega \to 0$ and an exponential decay at large ω.

In interacting integrable systems, the behavior of the matrix elements that connect different quasimomentum sectors of the Hamiltonian was shown to be the same as

what was found for translationally invariant operators in Ref. [45]. However, for low ω, differences were found between the behavior of operators that break integrability if added as perturbations to the Hamiltonian and those that do not. In the former case, the scaled variances of the off-diagonal matrix elements plateau at a constant nonzero value as $\omega \to 0$ regardless of whether or not the matrix elements mix quasimomentum sectors of the Hamiltonian. In the latter case, the variances approach zero for matrix elements that do not mix quasimomentum sectors, but plateau at a nonzero value for those that do. These observations are consistent with the findings in Ref. [130].

Additionally, in Chapter 4, we discussed the low-ω scaling properties of the variances of off-diagonal matrix elements of observables, which is especially rich in interacting integrable systems. First, we found a robust ballistic scaling regime of the variances for all observables considered. Ballistic scalings of the variances are of much interest due to their relevance to transport. For example, in Chapter 3, which is based on Ref. [131], a peak that scales ballistically in the variance of the current operator was shown to be present in a quantum-chaotic single-impurity model. This is indicative of coherent transport in that system.

Notably, we demonstrated in Chapter 4 that, irrespective of the value of Δ considered, the scaled variances of off-diagonal matrix elements exhibit diffusive scaling at low ω. We suggested that this implies that diffusion puts the ultimate limit on equilibration time in the XXZ chain. In quantum chaotic systems, a plateau that scales diffusively is expected because there must be lack of structure in the matrix elements below some ω threshold in order to make contact with random matrix theory, where there is no structure. An interesting open question is to characterize the Thouless energy, which is the energy scale that defines diffusive transport, in both classes of systems.

Lastly, in Chapter 5, we demonstrated that the onset of quantum chaos in both the perturbed XXZ model and the perturbed Anderson model is marked by universal behavior, with a peak in the fidelity susceptibility that scales as the square of the inverse level spacing developing in both cases. It was additionally observed that the value of perturbation strength at which these peaks occur decreases with increasing system size, a mark that only an infinitesimally small perturbation is needed to break induce chaos in the thermodynamic limit. Most notably, this implies that the Anderson insulator is not stable to perturbations in the thermodynamic limit.

Bibliography

[1] Mallayya, K. and M. Rigol (2019) "Heating Rates in Periodically Driven Strongly Interacting Quantum Many-Body Systems," *Phys. Rev. Lett.*, **123**, p. 240603.

[2] D'Alessio, L., Y. Kafri, A. Polkovnikov, and M. Rigol (2016) "From quantum chaos and eigenstate thermalization to statistical mechanics and thermodynamics," *Advances in Physics*, **65**(3), pp. 239–362.

[3] Langen, T., R. Geiger, and J. Schmiedmayer (2015) "Ultracold Atoms Out of Equilibrium," *Annu. Rev. Condens. Matter Phys.*, **6**(1), pp. 201–217.

[4] Bloch, I., J. Dalibard, and S. Nascimbane (2012) "Quantum simulations with ultracold quantum gases," *Nature Phys.*, **8**(4), pp. 267–276.

[5] Lewenstein, M., A. Sanpera, V. Ahufinger, B. Damski, A. Sen(De), and U. Sen (2007) "Ultracold atomic gases in optical lattices: mimicking condensed matter physics and beyond," *Adv. Phys.*, **56**(2), pp. 243–379.

[6] Kinoshita, T., T. Wenger, and D. S. Weiss (2006) "A quantum Newton's cradle," *Nature*, **440**(7086), pp. 900–903.

[7] Gring, M., M. Kuhnert, T. Langen, T. Kitagawa, B. Rauer, M. Schreitl, I. Mazets, D. A. Smith, E. Demler, and J. Schmiedmayer (2012) "Relaxation and Prethermalization in an Isolated Quantum System," *Science*, **337**, pp. 1318–1322.

[8] Langen, T., S. Erne, R. Geiger, B. Rauer, T. Schweigler, M. Kuhnert, W. Rohringer, I. E. Mazets, T. Gasenzer, and J. Schmiedmayer (2015) "Experimental observation of a generalized Gibbs ensemble," *Science*, **348**, p. 207.

[9] Tang, Y., W. Kao, K.-Y. Li, S. Seo, K. Mallayya, M. Rigol, S. Gopalakrishnan, and B. L. Lev (2018) "Thermalization near Integrability in a Dipolar Quantum Newton's Cradle," *Phys. Rev. X*, **8**, p. 021030.

[10] Trotzky, S., Y.-A. Chen, A. Flesch, I. P. McCulloch, U. Schollwöck, J. Eisert, and I. Bloch (2012) "Probing the relaxation towards equilibrium in an isolated strongly correlated one-dimensional Bose gas," *Nature Physics*, **8**, p. 325.

[11] Kaufman, A. M., M. E. Tai, A. Lukin, M. Rispoli, R. Schittko, P. M. Preiss, and M. Greiner (2016) "Quantum thermalization through entanglement in an isolated many-body system," *Science*, **353**, p. 794.

[12] Clos, G., D. Porras, U. Warring, and T. Schaetz (2016) "Time-Resolved Observation of Thermalization in an Isolated Quantum System," *Phys. Rev. Lett.*, **117**, p. 170401.

[13] Rigol, M., V. Dunjko, and M. Olshanii (2008) "Thermalization and its mechanism for generic isolated quantum systems," *Nature*, **452**, p. 854.

[14] "Lyapunov exponent," wikipedia.org.

[15] Shenker, S. H. and D. Stanford (2014) "Black holes and the butterfly effect," *Journal of High Energy Physics*, **2014**(3), p. 67.

[16] Rozenbaum, E. B., S. Ganeshan, and V. Galitski (2019) "Universal level statistics of the out-of-time-ordered operator," *Phys. Rev. B*, **100**, p. 035112.

[17] Bohigas, O., M. J. Giannoni, and C. Schmit (1984) "Characterization of Chaotic Quantum Spectra and Universality of Level Fluctuation Laws," *Phys. Rev. Lett.*, **52**, pp. 1–4.

[18] Berry, M. V., M. Tabor, and J. M. Ziman (1977) "Level clustering in the regular spectrum," *Proc. R. Soc. London A*, **356**(1686), pp. 375–394.

[19] Oganesyan, V. and D. A. Huse (2007) "Localization of interacting fermions at high temperature," *Phys. Rev. B*, **75**, p. 155111.

[20] Atas, Y. Y., E. Bogomolny, O. Giraud, and G. Roux (2013) "Distribution of the Ratio of Consecutive Level Spacings in Random Matrix Ensembles," *Phys. Rev. Lett.*, **110**, p. 084101.

[21] Alhassid, Y. (2000) "The statistical theory of quantum dots," *Rev. Mod. Phys.*, **72**, pp. 895–968.

[22] Vidmar, L. and M. Rigol (2017) "Entanglement Entropy of Eigenstates of Quantum Chaotic Hamiltonians," *Phys. Rev. Lett.*, **119**, p. 220603.

[23] Page, D. N. (1993) "Average entropy of a subsystem," *Phys. Rev. Lett.*, **71**, pp. 1291–1294.

[24] Srednicki, M. (1999) "The approach to thermal equilibrium in quantized chaotic systems," *Journal of Physics A: Mathematical and General*, **32**(7), pp. 1163–1175.

[25] Richter, J., A. Dymarsky, R. Steinigeweg, and J. Gemmer (2020) "Eigenstate thermalization hypothesis beyond standard indicators: Emergence of random-matrix behavior at small frequencies," *Phys. Rev. E*, **102**, p. 042127.

[26] Rigol, M. (2009) "Breakdown of Thermalization in Finite One-Dimensional Systems," *Phys. Rev. Lett.*, **103**, p. 100403.

[27] ——— (2009) "Quantum quenches and thermalization in one-dimensional fermionic systems," *Phys. Rev. A*, **80**, p. 053607.

[28] Santos, L. F. and M. Rigol (2010) "Localization and the effects of symmetries in the thermalization properties of one-dimensional quantum systems," *Phys. Rev. E*, **82**, p. 031130.

[29] Khatami, E., G. Pupillo, M. Srednicki, and M. Rigol (2013) "Fluctuation-Dissipation Theorem in an Isolated System of Quantum Dipolar Bosons after a Quench," *Phys. Rev. Lett.*, **111**, p. 050403.

[30] Steinigeweg, R., J. Herbrych, and P. Prelovšek (2013) "Eigenstate thermalization within isolated spin-chain systems," *Phys. Rev. E*, **87**, p. 012118.

[31] Beugeling, W., R. Moessner, and M. Haque (2014) "Finite-size scaling of eigenstate thermalization," *Phys. Rev. E*, **89**, p. 042112.

[32] Steinigeweg, R., A. Khodja, H. Niemeyer, C. Gogolin, and J. Gemmer (2014) "Pushing the Limits of the Eigenstate Thermalization Hypothesis towards Mesoscopic Quantum Systems," *Phys. Rev. Lett.*, **112**, p. 130403.

[33] Sorg, S., L. Vidmar, L. Pollet, and F. Heidrich-Meisner (2014) "Relaxation and thermalization in the one-dimensional Bose-Hubbard model: A case study for the interaction quantum quench from the atomic limit," *Phys. Rev. A*, **90**, p. 033606.

[34] Kim, H., T. N. Ikeda, and D. A. Huse (2014) "Testing whether all eigenstates obey the eigenstate thermalization hypothesis," *Phys. Rev. E*, **90**, p. 052105.

[35] Beugeling, W., R. Moessner, and M. Haque (2015) "Off-diagonal matrix elements of local operators in many-body quantum systems," *Phys. Rev. E*, **91**, p. 012144.

[36] Mondaini, R., K. R. Fratus, M. Srednicki, and M. Rigol (2016) "Eigenstate thermalization in the two-dimensional transverse field Ising model," *Phys. Rev. E*, **93**, p. 032104.

[37] Mondaini, R. and M. Rigol (2017) "Eigenstate thermalization in the two-dimensional transverse field Ising model. II. Off-diagonal matrix elements of observables," *Phys. Rev. E*, **96**, p. 012157.

[38] Yoshizawa, T., E. Iyoda, and T. Sagawa (2018) "Numerical Large Deviation Analysis of the Eigenstate Thermalization Hypothesis," *Phys. Rev. Lett.*, **120**, p. 200604.

[39] Khaymovich, I. M., M. Haque, and P. A. McClarty (2019) "Eigenstate Thermalization, Random Matrix Theory, and Behemoths," *Phys. Rev. Lett.*, **122**, p. 070601.

[40] Jansen, D., J. Stolpp, L. Vidmar, and F. Heidrich-Meisner (2019) "Eigenstate thermalization and quantum chaos in the Holstein polaron model," *Phys. Rev. B*, **99**, p. 155130.

[41] Mierzejewski, M. and L. Vidmar (2020) "Quantitative Impact of Integrals of Motion on the Eigenstate Thermalization Hypothesis," *Phys. Rev. Lett.*, **124**, p. 040603.

[42] Pandey, M., P. W. Claeys, D. K. Campbell, A. Polkovnikov, and D. Sels (2020) "Adiabatic Eigenstate Deformations as a Sensitive Probe for Quantum Chaos," *Phys. Rev. X*, **10**, p. 041017.

[43] Rigol, M., V. Dunjko, V. Yurovsky, and M. Olshanii (2007) "Relaxation in a Completely Integrable Many-Body Quantum System: An Ab Initio Study of the Dynamics of the Highly Excited States of 1D Lattice Hard-Core Bosons," *Phys. Rev. Lett.*, **98**, p. 050405.

[44] Cassidy, A. C., C. W. Clark, and M. Rigol (2011) "Generalized Thermalization in an Integrable Lattice System," *Phys. Rev. Lett.*, **106**, p. 140405.

[45] LeBlond, T., K. Mallayya, L. Vidmar, and M. Rigol (2019) "Entanglement and matrix elements of observables in interacting integrable systems," *Phys. Rev. E*, **100**, p. 062134.

[46] LeBlond, T. and M. Rigol (2020) "Eigenstate thermalization for observables that break Hamiltonian symmetries and its counterpart in interacting integrable systems," *Phys. Rev. E*, **102**, p. 062113.

[47] Brenes, M., E. Mascarenhas, M. Rigol, and J. Goold (2018) "High-temperature coherent transport in the XXZ chain in the presence of an impurity," *Phys. Rev. B*, **98**, p. 235128.

[48] LeBlond, T., D. Sels, A. Polkovnikov, and M. Rigol (2020), "Universality in the Onset of Quantum Chaos in Many-Body Systems," arXiv:2012.07849.

[49] Eisert, J., M. Friesdorf, and C. Gogolin (2015) "Quantum many-body systems out of equilibrium," *Nature Phys.*, **11**, p. 124.

[50] Polkovnikov, A., K. Sengupta, A. Silva, and M. Vengalattore (2011) "*Colloquium*: Nonequilibrium dynamics of closed interacting quantum systems," *Rev. Mod. Phys.*, **83**, pp. 863–883.

[51] Essler, F. H. L. and M. Fagotti "Quench dynamics and relaxation in isolated integrable quantum spin chains," *J. Stat. Mech.*, (2016)(6), p. 064002.

[52] Calabrese, P. and J. Cardy "Quantum quenches in 1+1 dimensional conformal field theories," *J. Stat. Mech.*, (2016)(6), p. 064003.

[53] Cazalilla, M. A. and M.-C. Chung "Quantum quenches in the Luttinger model and its close relatives," *J. Stat. Mech.*, (2016)(6), p. 064004.

[54] Bernard, D. and B. Doyon "Conformal field theory out of equilibrium: a review," *J. Stat. Mech.*, (2016)(6), p. 064005.

[55] Caux, J.-S. "The Quench Action," *J. Stat. Mech.*, (2016)(6), p. 064006.

[56] Vidmar, L. and M. Rigol "Generalized Gibbs ensemble in integrable lattice models," *J. Stat. Mech.*, (2016)(6), p. 064007.

[57] Ilievski, E., M. Medenjak, T. Prosen, and L. Zadnik "Quasilocal charges in integrable lattice systems," *J. Stat. Mech.*, (2016)(6), p. 064008.

[58] Langen, T., T. Gasenzer, and J. Schmiedmayer "Prethermalization and universal dynamics in near-integrable quantum systems," *J. Stat. Mech.*, (2016)(6), p. 064009.

[59] Vasseur, R. and J. E. Moore (2016) "Nonequilibrium quantum dynamics and transport: from integrability to many-body localization," *J. Stat. Mech.*, (2016)(6), p. 064010.

[60] De Luca, A. and G. Mussardo "Equilibration properties of classical integrable field theories," *J. Stat. Mech.*, (2016)(6), p. 064011.

[61] Wouters, B., J. De Nardis, M. Brockmann, D. Fioretto, M. Rigol, and J.-S. Caux (2014) "Quenching the Anisotropic Heisenberg Chain: Exact Solution and Generalized Gibbs Ensemble Predictions," *Phys. Rev. Lett.*, **113**, p. 117202.

[62] Pozsgay, B., M. Mestyán, M. A. Werner, M. Kormos, G. Zaránd, and G. Takács (2014) "Correlations after Quantum Quenches in the XXZ Spin Chain: Failure of the Generalized Gibbs Ensemble," *Phys. Rev. Lett.*, **113**, p. 117203.

[63] Ilievski, E., J. De Nardis, B. Wouters, J.-S. Caux, F. H. L. Essler, and T. Prosen (2015) "Complete Generalized Gibbs Ensembles in an Interacting Theory," *Phys. Rev. Lett.*, **115**, p. 157201.

[64] Deutsch, J. M. (1991) "Quantum statistical mechanics in a closed system," *Phys. Rev. A*, **43**, pp. 2046–2049.

[65] Srednicki, M. (1994) "Chaos and quantum thermalization," *Phys. Rev. E*, **50**, pp. 888–901.

[66] Biroli, G., C. Kollath, and A. M. Läuchli (2010) "Effect of Rare Fluctuations on the Thermalization of Isolated Quantum Systems," *Phys. Rev. Lett.*, **105**, p. 250401.

[67] Ikeda, T. N., Y. Watanabe, and M. Ueda (2013) "Finite-size scaling analysis of the eigenstate thermalization hypothesis in a one-dimensional interacting Bose gas," *Phys. Rev. E*, **87**, p. 012125.

[68] Alba, V. (2015) "Eigenstate thermalization hypothesis and integrability in quantum spin chains," *Phys. Rev. B*, **91**, p. 155123.

[69] Alba, V., M. Fagotti, and P. Calabrese "Entanglement entropy of excited states," *J. Stat. Mech.*, (2009)(10), p. P10020.

[70] Deutsch, J. M. (2010) "Thermodynamic entropy of a many-body energy eigenstate," *New J. Phys.*, **12**(7), p. 075021.

[71] Santos, L. F., A. Polkovnikov, and M. Rigol (2012) "Weak and strong typicality in quantum systems," *Phys. Rev. E*, **86**, p. 010102(R).

[72] Hamma, A., S. Santra, and P. Zanardi (2012) "Quantum Entanglement in Random Physical States," *Phys. Rev. Lett.*, **109**, p. 040502.

[73] Deutsch, J. M., H. Li, and A. Sharma (2013) "Microscopic origin of thermodynamic entropy in isolated systems," *Phys. Rev. E*, **87**, p. 042135.

[74] Mölter, J., T. Barthel, U. Schollwöck, and V. Alba "Bound states and entanglement in the excited states of quantum spin chains," *J. Stat. Mech.*, (2014)(10), p. P10029.

[75] Storms, M. and R. R. P. Singh (2014) "Entanglement in ground and excited states of gapped free-fermion systems and their relationship with Fermi surface and thermodynamic equilibrium properties," *Phys. Rev. E*, **89**, p. 012125.

[76] Beugeling, W., A. Andreanov, and M. Haque "Global characteristics of all eigenstates of local many-body Hamiltonians: participation ratio and entanglement entropy," *J. Stat. Mech.*, (2015)(2), p. P02002.

[77] Yang, Z.-C., C. Chamon, A. Hamma, and E. R. Mucciolo (2015) "Two-Component Structure in the Entanglement Spectrum of Highly Excited States," *Phys. Rev. Lett.*, **115**, p. 267206.

[78] Lai, H.-H. and K. Yang (2015) "Entanglement entropy scaling laws and eigenstate typicality in free fermion systems," *Phys. Rev. B*, **91**, p. 081110(R).

[79] Nandy, S., A. Sen, A. Das, and A. Dhar (2016) "Eigenstate Gibbs ensemble in integrable quantum systems," *Phys. Rev. B*, **94**, p. 245131.

[80] Vidmar, L., L. Hackl, E. Bianchi, and M. Rigol (2017) "Entanglement Entropy of Eigenstates of Quadratic Fermionic Hamiltonians," *Phys. Rev. Lett.*, **119**, p. 020601.

[81] Dymarsky, A., N. Lashkari, and H. Liu (2018) "Subsystem eigenstate thermalization hypothesis," *Phys. Rev. E*, **97**, p. 012140.

[82] Riddell, J. and M. P. Müller (2018) "Generalized eigenstate typicality in translation-invariant quasifree fermionic models," *Phys. Rev. B*, **97**, p. 035129.

[83] Zhang, Y., L. Vidmar, and M. Rigol (2018) "Information measures for a local quantum phase transition: Lattice fermions in a one-dimensional harmonic trap," *Phys. Rev. A*, **97**, p. 023605.

[84] Liu, C., X. Chen, and L. Balents (2018) "Quantum entanglement of the Sachdev-Ye-Kitaev models," *Phys. Rev. B*, **97**, p. 245126.

[85] Garrison, J. R. and T. Grover (2018) "Does a Single Eigenstate Encode the Full Hamiltonian?" *Phys. Rev. X*, **8**, p. 021026.

[86] Nakagawa, Y. O., M. Watanabe, H. Fujita, and S. Sugiura (2018) "Universality in volume-law entanglement of scrambled pure quantum states," *Nat. Comm.*, **9**, p. 1635.

[87] Vidmar, L., L. Hackl, E. Bianchi, and M. Rigol (2018) "Volume Law and Quantum Criticality in the Entanglement Entropy of Excited Eigenstates of the Quantum Ising Model," *Phys. Rev. Lett.*, **121**, p. 220602.

[88] Huang, Y. (2019) "Universal eigenstate entanglement of chaotic local Hamiltonians," *Nuc. Phys. B*, **938**, pp. 594 – 604.

[89] Hackl, L., L. Vidmar, M. Rigol, and E. Bianchi (2019) "Average eigenstate entanglement entropy of the XY chain in a transverse field and its universality for translationally invariant quadratic fermionic models," *Phys. Rev. B*, **99**, p. 075123.

[90] Murciano, S., P. Ruggiero, and P. Calabrese "Entanglement and relative entropies for low-lying excited states in inhomogeneous one-dimensional quantum systems," *J. Stat. Mech.*, (2019)(3), p. 034001.

[91] Lu, T.-C. and T. Grover (2019) "Renyi entropy of chaotic eigenstates," *Phys. Rev. E*, **99**, p. 032111.

[92] Sun, L.-Z., Q. Nie, and H. Li (2019) "Randomness of Eigenstates of Many-Body Quantum Systems," *Entropy*, **21**(3).

[93] Giovenale, N., F. M. Pont, P. Serra, and O. Osenda (2019) "Convexity properties of superpositions of degenerate bipartite eigenstates," *Phys. Rev. A*, **99**, p. 052340.

[94] Bertini, B., P. Kos, and T. Prosen (2019) "Entanglement Spreading in a Minimal Model of Maximal Many-Body Quantum Chaos," *Phys. Rev. X*, **9**, p. 021033.

[95] Huang, Y. and Y. Gu (2019) "Eigenstate entanglement in the Sachdev-Ye-Kitaev model," *Phys. Rev. D*, **100**, p. 041901(R).

[96] Murthy, C. and M. Srednicki (2019) "Structure of chaotic eigenstates and their entanglement entropy," *Phys. Rev. E*, **100**, p. 022131.

[97] Morampudi, S. C., A. Chandran, and C. R. Laumann (2020) "Universal Entanglement of Typical States in Constrained Systems," *Phys. Rev. Lett.*, **124**, p. 050602.

[98] Modak, R. and T. Nag (2020) "Many-body dynamics in long-range hopping models in the presence of correlated and uncorrelated disorder," *Phys. Rev. Research*, **2**, p. 012074.

[99] Miao, Q. and T. Barthel, "Eigenstate entanglement: Crossover from the ground state to volume laws," arXiv:1905.07760.

[100] Bianchi, E. and P. Donà (2019) "Typical entanglement entropy in the presence of a center: Page curve and its variance," *Phys. Rev. D*, **100**, p. 105010.

[101] Faiez, D. and D. Šafránek (2020) "How much entanglement can be created in a closed system," *Phys. Rev. B*, **101**, p. 060401.

[102] Faiez, D., D. Šafránek, J. M. Deutsch, and A. Aguirre (2020) "Typical and extreme entropies of long-lived isolated quantum systems," *Phys. Rev. A*, **101**, p. 052101.

[103] Jafarizadeh, A. and M. A. Rajabpour (2019) "Bipartite entanglement entropy of the excited states of free fermions and harmonic oscillators," *Phys. Rev. B*, **100**, p. 165135.

[104] Cazalilla, M. A., R. Citro, T. Giamarchi, E. Orignac, and M. Rigol (2011) "One dimensional bosons: From condensed matter systems to ultracold gases," *Rev. Mod. Phys.*, **83**, pp. 1405–1466.

[105] Santos, L. F. and M. Rigol (2010) "Onset of quantum chaos in one-dimensional bosonic and fermionic systems and its relation to thermalization," *Phys. Rev. E*, **81**, p. 036206.

[106] Hartmann, M., G. Mahler, and O. Hess (2004) "Gaussian Quantum Fluctuations in Interacting Many Particle Systems," *Lett. Math. Phys.*, **68**, p. 103.

[107] ——— (2005) "Spectral Densities and Partition Functions of Modular Quantum ystems as Derived from a Central Limit Theorem," *J. Stat. Phys.*, **119**, p. 1139.

[108] Luitz, D. J. and Y. Bar Lev (2016) "Anomalous Thermalization in Ergodic Systems," *Phys. Rev. Lett.*, **117**, p. 170404.

[109] Schrödinger, E. (1927) "Energieaustausch nach der Wellenmechanik," *Ann. Phys. (N.Y.)*, **388**(15), pp. 956–968.

[110] Neumann, J. v. (1929) "Beweis des Ergodensatzes und desH-Theorems in der neuen Mechanik," *Z. Phys.*, **57**(1), pp. 30–70.

[111] Goldstein, S., J. L. Lebowitz, C. Mastrodonato, R. Tumulka, and N. Zanghì (2010) "Normal typicality and von Neumann's quantum ergodic theorem," *Proc. R. Soc. A*, **466**(2123), pp. 3203–3224.

[112] Rigol, M. (2016) "Fundamental Asymmetry in Quenches Between Integrable and Nonintegrable Systems," *Phys. Rev. Lett.*, **116**, p. 100601.

[113] Santos, L. (2004) "Integrability of a disordered Heisenberg spin-1/2 chain," *J. Phys. A*, **37**(17), p. 4723.

[114] Santos, L. F. and A. Mitra (2011) "Domain wall dynamics in integrable and chaotic spin-1/2 chains," *Phys. Rev. E*, **84**(1), p. 016206.

[115] Torres-Herrera, E. J. and L. F. Santos (2014) "Local quenches with global effects in interacting quantum systems," *Phys. Rev. E*, **89**(6), p. 062110.

[116] Torres-Herrera, E. J., D. Kollmar, and L. F. Santos (2015) "Relaxation and thermalization of isolated many-body quantum systems," *Phys. Scr.*, **T165**, p. 014018.

[117] Barišić, O. S., P. Prelovšek, A. Metavitsiadis, and X. Zotos (2009) "Incoherent transport induced by a single static impurity in a Heisenberg chain," *Phys. Rev. B*, **80**, p. 125118.

[118] Metavitsiadis, A., X. Zotos, O. S. Barišić, and P. Prelovšek (2010) "Thermal transport in a spin-$\frac{1}{2}$ Heisenberg chain coupled to a magnetic or nonmagnetic impurity," *Phys. Rev. B*, **81**, p. 205101.

[119] Bertini, B., F. Heidrich-Meisner, C. Karrasch, T. Prosen, R. Steinigeweg, and M. Znidaric, "Finite-temperature transport in one-dimensional quantum lattice models," arXiv:2003.03334.

[120] Shastry, B. S. and B. Sutherland (1990) "Twisted boundary conditions and effective mass in Heisenberg-Ising and Hubbard rings," *Phys. Rev. Lett.*, **65**, pp. 243–246.

[121] Rigol, M. and M. Srednicki (2012) "Alternatives to Eigenstate Thermalization," *Phys. Rev. Lett.*, **108**, p. 110601.

[122] Kubo, R. (1957) "Statistical-mechanical theory of irreversible processes. I. General theory and simple applications to magnetic and conduction problems," *J. Phys. Soc. Jpn.*, **12**(6), pp. 570–586.

[123] Kubo, R., M. Yokota, and S. Nakajima (1957) "Statistical-mechanical theory of irreversible processes. II. Response to thermal disturbance," *J. Phys. Soc. Jpn.*, **12**(11), pp. 1203–1211.

[124] Mukerjee, S. and B. S. Shastry (2008) "Signatures of diffusion and ballistic transport in the stiffness, dynamical correlation functions, and statistics of one-dimensional systems," *Phys. Rev. B*, **77**, p. 245131.

[125] Rigol, M. and B. S. Shastry (2008) "Drude weight in systems with open boundary conditions," *Phys. Rev. B*, **77**, p. 161101(R).

[126] Žnidarič, M. (2011) "Spin Transport in a One-Dimensional Anisotropic Heisenberg Model," *Phys. Rev. Lett.*, **106**, p. 220601.

[127] Jepsen, N., J. Amato-Grill, I. Dimitrova, W. W. Ho, E. Demler, and W. Ketterle, arXiv:2005.09549.

[128] Mori, T., T. N. Ikeda, E. Kaminishi, and M. Ueda (2018) "Thermalization and prethermalization in isolated quantum systems: a theoretical overview," *J. Phys. B*, **51**(11), p. 112001.

[129] Yoshizawa, T., E. Iyoda, and T. Sagawa (2018) "Numerical Large Deviation Analysis of the Eigenstate Thermalization Hypothesis," *Phys. Rev. Lett.*, **120**, p. 200604.

[130] Brenes, M., T. LeBlond, J. Goold, and M. Rigol (2020) "Eigenstate Thermalization in a Locally Perturbed Integrable System," *Phys. Rev. Lett.*, **125**, p. 070605.

[131] Brenes, M., J. Goold, and M. Rigol (2020) "Low-frequency behavior of off-diagonal matrix elements in the integrable XXZ chain and in a locally perturbed quantum-chaotic XXZ chain," *Phys. Rev. B*, **102**, p. 075127.

[132] Villazon, T., P. W. Claeys, M. Pandey, A. Polkovnikov, and A. Chandran (2020) "Persistent dark states in anisotropic central spin models," *Sci. Rep.*, **10**, p. 16080.

[133] Dymarsky, A. and H. Liu (2019) "New characteristic of quantum many-body chaotic systems," *Phys. Rev. E*, **99**, p. 010102(R).

[134] Dymarsky, A. (2019) "Mechanism of macroscopic equilibration of isolated quantum systems," *Phys. Rev. B*, **99**, p. 224302.

[135] Santos, L. F., F. Pérez-Bernal, and E. J. Torres-Herrera (2020) "Speck of chaos," *Phys. Rev. Research*, **2**, p. 043034.

[136] Richter, J., A. Dymarsky, R. Steinigeweg, and J. Gemmer (2020) "Eigenstate thermalization hypothesis beyond standard indicators: Emergence of random-matrix behavior at small frequencies," *Phys. Rev. E*, **102**, p. 042127.

[137] Serbyn, M., Z. Papić, and D. A. Abanin (2017) "Thouless energy and multifractality across the many-body localization transition," *Phys. Rev. B*, **96**, p. 104201.

[138] Brenes, M., S. Pappalardi, J. Goold, and A. Silva (2020) "Multipartite Entanglement Structure in the Eigenstate Thermalization Hypothesis," *Phys. Rev. Lett.*, **124**, p. 040605.

[139] Rigol, M. and B. S. Shastry (2008) "Drude weight in systems with open boundary conditions," *Phys. Rev. B*, **77**, p. 161101(R).

[140] De Nardis, J., D. Bernard, and B. Doyon (2018) "Hydrodynamic Diffusion in Integrable Systems," *Phys. Rev. Lett.*, **121**, p. 160603.

[141] Gopalakrishnan, S., D. A. Huse, V. Khemani, and R. Vasseur (2018) "Hydrodynamics of operator spreading and quasiparticle diffusion in interacting integrable systems," *Phys. Rev. B*, **98**, p. 220303(R).

[142] Ilievski, E., J. De Nardis, M. Medenjak, and T. Prosen (2018) "Superdiffusion in One-Dimensional Quantum Lattice Models," *Phys. Rev. Lett.*, **121**, p. 230602.

[143] Gopalakrishnan, S. and R. Vasseur (2019) "Kinetic Theory of Spin Diffusion and Superdiffusion in XXZ Spin Chains," *Phys. Rev. Lett.*, **122**, p. 127202.

[144] Gopalakrishnan, S., R. Vasseur, and B. Ware (2019) "Anomalous relaxation and the high-temperature structure factor of XXZ spin chains," *Proc. Natl. Acad. Sci.*, **116**(33), pp. 16250–16255.

[145] Bulchandani, V. B. (2020) "Kardar-Parisi-Zhang universality from soft gauge modes," *Phys. Rev. B*, **101**, p. 041411(R).

[146] Agrawal, U., S. Gopalakrishnan, R. Vasseur, and B. Ware (2020) "Anomalous low-frequency conductivity in easy-plane XXZ spin chains," *Phys. Rev. B*, **101**, p. 224415.

[147] Fava, M., B. Ware, S. Gopalakrishnan, R. Vasseur, and S. A. Parameswaran (2020) "Spin crossovers and superdiffusion in the one-dimensional Hubbard model," *Phys. Rev. B*, **102**, p. 115121.

[148] We thank an anonymous referee for suggesting this analysis.

[149] Deutsch, J. M. (2018) "Eigenstate thermalization hypothesis," *Rep. Prog. Phys.*, **81**(8), p. 082001.

[150] Wigner, E. (1955) "Characteristic vectors of bordered matrices with infinite dimensions," *Ann. of Math.*, **62**, pp. 548–564.

[151] ——— (1957) "Characteristic vectors of bordered matrices of infinite dimensions II," *Ann. of Math.*, **65**, pp. 203–207.

[152] ——— (1958) "On the distribution of the roots of certain symmetric matrices," *Ann. of Math.*, **67**, pp. 325–326.

[153] Dyson, F. J. (1962) "Statistical Theory of the Energy Levels of Complex Systems. I," *J. Math. Phys.*, **3**(1), pp. 140–156.

[154] ——— (1962) "Statistical Theory of the Energy Levels of Complex Systems. II," *J. Math. Phys.*, **3**(1), pp. 157–165.

[155] ——— (1962) "Statistical Theory of the Energy Levels of Complex Systems. III," *J. Math. Phys.*, **3**(1), pp. 166–175.

[156] von Neumann, J. (1929) "Proof of the ergodic theorem and the H-theorem in quantum mechanics," *Z. Physik*, **57**, pp. 30–70.

[157] Goldstein, S., J. L. Lebowitz, R. Tumulka, and N. Zanghì (2010) "Long-time behavior of macroscopic quantum systems," *European Phys. J. H*, **35**, pp. 173–200.

[158] Nandkishore, R. and D. A. Huse (2015) "Many-Body Localization and Thermalization in Quantum Statistical Mechanics," *Annu. Rev. Condens. Matter Phys,*, **6**, pp. 15–38.

[159] Altman, E. and R. Vosk (2015) "Universal Dynamics and Renormalization in Many-Body-Localized Systems," *Annu. Rev. Condens. Matter Phys.*, **6**, pp. 383–409.

[160] Abanin, D. A., E. Altman, I. Bloch, and M. Serbyn (2019) "Colloquium: Many-body localization, thermalization, and entanglement," *Rev. Mod. Phys.*, **91**, p. 021001.

[161] Schreiber, M., S. S. Hodgman, P. Bordia, H. P. Lüschen, M. H. Fischer, R. Vosk, E. Altman, U. Schneider, and I. Bloch (2015) "Observation of many-body localization of interacting fermions in a quasi-random optical lattice," *Science*, **349**, p. 842.

[162] Choi, J.-Y., S. Hild, J. Zeiher, P. Schauss, A. Rubio-Abadal, T. Yefsah, V. Khemani, D. A. Huse, I. Bloch, and C. Gross (2016) "Exploring the many-body localization transition in two dimensions," *Science*, **352**, p. 1547.

[163] Malvania, N., Y. Zhang, Y. Le, J. Dubail, M. Rigol, and D. S. Weiss, "Generalized hydrodynamics in strongly interacting 1D Bose gases," arXiv:2009.06651.

[164] Rabson, D. A., B. N. Narozhny, and A. J. Millis (2004) "Crossover from Poisson to Wigner-Dyson level statistics in spin chains with integrability breaking," *Phys. Rev. B*, **69**, p. 054403.

[165] Modak, R., S. Mukerjee, and S. Ramaswamy (2014) "Universal power law in crossover from integrability to quantum chaos," *Phys. Rev. B*, **90**, p. 075152.

[166] Modak, R. and S. Mukerjee (2014) "Finite size scaling in crossover among different random matrix ensembles in microscopic lattice models," *New J. Phys.*, **16**, p. 093016.

[167] Mallayya, K. and M. Rigol (2018) "Quantum Quenches and Relaxation Dynamics in the Thermodynamic Limit," *Phys. Rev. Lett.*, **120**, p. 070603.

[168] Mallayya, K., M. Rigol, and W. De Roeck (2019) "Prethermalization and Thermalization in Isolated Quantum Systems," *Phys. Rev. X*, **9**, p. 021027.

[169] Gornyi, I. V., A. D. Mirlin, and D. G. Polyakov (2005) "Interacting Electrons in Disordered Wires: Anderson Localization and Low-T Transport," *Phys. Rev. Lett.*, **95**, p. 206603.

[170] (2006) "Metal–insulator transition in a weakly interacting many-electron system with localized single-particle states," *Ann. Phys. (N. Y.)*, **321**(5), pp. 1126 – 1205.

[171] Šuntajs, J., J. Bonča, T. Prosen, and L. Vidmar, "Quantum chaos challenges many-body localization," arXiv:1905.06345.

[172] Abanin, D. A., J. H. Bardarson, G. D. Tomasi, S. Gopalakrishnan, V. Khemani, S. A. Parameswaran, F. Pollmann, A. C. Potter, M. Serbyn, and R. Vasseur, "Distinguishing localization from chaos: challenges in finite-size systems," arXiv:1911.04501.

[173] Šuntajs, J., J. Bonča, T. Prosen, and L. Vidmar (2020) "Ergodicity breaking transition in finite disordered spin chains," *Phys. Rev. B*, **102**, p. 064207.

[174] Sels, D. and A. Polkovnikov, "Dynamical obstruction to localization in a disordered spin chain," arXiv:2009.04501.

[175] Kiefer-Emmanouilidis, M., R. Unanyan, M. Fleischhauer, and J. Sirker, "Absence of true localization in many-body localized phases," arXiv:2010.00565.

[176] Campos Venuti, L. and P. Zanardi (2007) "Quantum Critical Scaling of the Geometric Tensors," *Phys. Rev. Lett.*, **99**, p. 095701.

[177] Kolodrubetz, M., V. Gritsev, and A. Polkovnikov (2013) "Classifying and measuring geometry of a quantum ground state manifold," *Phys. Rev. B*, **88**, p. 064304.

[178] Zanardi, P. and N. Paunković (2006) "Ground state overlap and quantum phase transitions," *Phys. Rev. E*, **74**, p. 031123.

[179] Rigol, M., B. S. Shastry, and S. Haas (2009) "Fidelity and superconductivity in two-dimensional $t-J$ models," *Phys. Rev. B*, **80**, p. 094529.

[180] Kolodrubetz, M., D. Sels, P. Mehta, and A. Polkovnikov (2017) "Geometry and non-adiabatic response in quantum and classical systems," *Phys. Rep.*, **697**, pp. 1 – 87.

[181] See appendices for additional numerical results, which include the spectral functions of the unperturbed models and for additional parameters to the ones reported in the main text, as well as typical fidelity susceptibilities for other observables. We also provide a perturbation theory derivation of the $(\epsilon/\omega)^2$ behavior of the spectral function and discuss its relation to Fermi's golden rule.

[182] Schönle, C., D. Jansen, F. Heidrich-Meisner, and L. Vidmar, "Eigenstate thermalization hypothesis through the lens of autocorrelation functions," arXiv:2011.13958.

[183] Łydżba, P., M. Rigol, and L. Vidmar (2020) "Eigenstate Entanglement Entropy in Random Quadratic Hamiltonians," *Phys. Rev. Lett.*, **125**, p. 180604.

Vita

Tyler LeBlond

Tyler LeBlond mostly grew up in the northeast part of the United States, and lived in places such as New Hampshire and Connecticut. He began attending Rensselaer Polytechnic Institute in Troy, NY in August 2012, where he received Bachelor's degrees in chemistry and physics and remained for a Master's degree in physics. There, his research in computational chemistry was advised by Prof. Peter Dinolfo. In August 2017, he began his Ph. D studies at the Pennsylvania State University in the department of physics and started research with Prof. Marcos Rigol in the summer of 2018.

Full list of publications (as of Jan. 5, 2021)

1. **T. LeBlond**, D. Sels, A. Polkovnikov, and M. Rigol. Universality in the Onset of Quantum Chaos in Many-Body Systems, arXiv:2012.07849 (2020)

2. **T. LeBlond**, and M. Rigol. Eigenstate thermalization for observables that break Hamiltonian symmetries and its counterpart in interacting integrable systems, Phys. Rev. E **102**, 062113 (2020).

3. M. Brenes, **T. LeBlond**, J. Goold, and M. Rigol. Eigenstate thermalization in a locally perturbed integrable system, Phys. Rev. Lett. **125**, 070605 (2020).

4. **T. LeBlond**, K. Mallayya, L. Vidmar, and M. Rigol. Entanglement and matrix elements of observables in interacting integrable systems, Phys. Rev. E **100**, 062134 (2019).

5. **T. LeBlond**, and P. H. Dinolfo. Density Functional Theory Prediction of the Electrocatalytic Mechanism of Proton Reduction by a Dicobalt Tetrakis(Schiff base) Macrocycle, *Inorg. Chem.* 2020, 59, 6, 3764